

2003

The analysis and modeling of pressure fluctuations in a fluidized bed

David Thomas Falkowski
Iowa State University

Follow this and additional works at: <https://lib.dr.iastate.edu/rtd>

 Part of the [Mechanical Engineering Commons](#)

Recommended Citation

Falkowski, David Thomas, "The analysis and modeling of pressure fluctuations in a fluidized bed " (2003). *Retrospective Theses and Dissertations*. 578.

<https://lib.dr.iastate.edu/rtd/578>

This Dissertation is brought to you for free and open access by the Iowa State University Capstones, Theses and Dissertations at Iowa State University Digital Repository. It has been accepted for inclusion in Retrospective Theses and Dissertations by an authorized administrator of Iowa State University Digital Repository. For more information, please contact digirep@iastate.edu.

The analysis and modeling of pressure fluctuations in a fluidized bed

by

David Thomas Falkowski

A dissertation submitted to the graduate faculty
in partial fulfillment of the requirements for the degree of

DOCTOR OF PHILOSOPHY

Major: Mechanical Engineering

Program of Study Committee:
Robert C. Brown, Major Professor
Gerald Colver
Theodore Heindel
Steven Hoff
Vijay Vittal

Iowa State University

Ames, Iowa

2003

UMI Number: 3085903

UMI[®]

UMI Microform 3085903

Copyright 2003 by ProQuest Information and Learning Company.
All rights reserved. This microform edition is protected against
unauthorized copying under Title 17, United States Code.

ProQuest Information and Learning Company
300 North Zeeb Road
P.O. Box 1346
Ann Arbor, MI 48106-1346

Graduate College
Iowa State University

This is to certify that the doctoral dissertation of
David Thomas Falkowski
has met the dissertation requirements of Iowa State University

Signature was redacted for privacy.

Major Professor

Signature was redacted for privacy.

For the Major Program

TABLE OF CONTENTS

ACKNOWLEDGEMENTS	iv
ABSTRACT	v
CHAPTER 1. INTRODUCTION	1
CHAPTER 2. LITERATURE REVIEW	4
CHAPTER 3. DATA ANALYSIS AND MODELING PARAMETERS	32
CHAPTER 4. EXPERIMENTAL APPARATUS AND PROCEDURE	52
CHAPTER 5. RESULTS AND DISCUSSION	65
CHAPTER 6. CONCLUSIONS AND RECOMMENDATIONS	131
REFERENCES	137
APPENDIX A. BADGER SAND SIEVE ANALYSIS	145
APPENDIX B. MATHCAD ANALYSIS PROGRAM	147
APPENDIX C. POWER SPECTRUMS AT SIX BED HEIGHTS WITH DIFFERENT PROBE ARM POSITIONS	151
APPENDIX D. EXPERIMENTAL AND MODELED POWER SPECTRUMS AT DIFFERENT BED HEIGHTS	158

ACKNOWLEDGEMENTS

I would first like to thank my major professor Dr. Robert Brown for providing countless recommendations and allowing me to pursue this research. The insight that he provided was essential to this research. I would also like to thank Dr. Gerald Colver, Dr. Theodore Heindel, Dr. Steven Hoff, and Dr. Vijay Vittal for serving on my committee and providing valuable insight and recommendations on my research. A large part of the experimental apparatus was constructed with the help of Daren Daugaard and background work was provided by Ethan Brue, both of whom I would like to thank. I would also like to thank all of the members of CSET for their direct involvement in this project, especially Diane Love, Tonia McCarley, Jim Pollard, Jerod Smeenk, and Andy Suby. Most of my research has been funded through various grants from the Iowa Energy Center, and I am grateful for this contribution.

Throughout my life, my family and friends have always supported me in my endeavors, especially my parents, Larry and Janet. This dissertation is dedicated to all of them (although I'm sure that not one of them will read it).

ABSTRACT

The objective of this research was to evaluate several different pressure probe techniques used to measure the pressure fluctuations in a fluidized bed, to determine the effect of bed parameters on the power spectrums from the corresponding pressure fluctuations, and to develop a second-order model that describes the power spectrums of these pressure fluctuations. The motivation for this work is to increase the knowledge of fluidized bed pressure phenomena and consequently further the understanding of such fluidized bed research areas as similitude, chemical processes, and the use of pressure fluctuations as a diagnostic tool.

Pressure fluctuations in a fluidized bed were measured with four pressure probe techniques to determine if differences existed amongst them. These techniques included static-absolute, dynamic-absolute, static-differential, and dynamic-differential pressure probe techniques. The pressure fluctuation data were analyzed using spectral analysis techniques and graphed on Bode plots. This testing showed that the absolute and differential pressure probe technique produced drastically different results under certain conditions. Comparison of the dynamic and static techniques showed that the results were very similar in most situations, but that the amplitude of the pressure fluctuations measured with the static technique was lower than that of the dynamic technique in a few situations. The position of the probe arm in the bed was also determined to be an important testing parameter for all techniques as several frequency peaks in the power spectrum were a function of position in the bed.

Pressure fluctuation data for a range of bed heights, fluidization velocities, particle sizes, particle densities, and bed temperatures were taken to determine each parameter's effect on the power spectrum. The relationship between the bed height and location of the dominant frequency was shown to agree with the literature, but secondary peaks were shown to be a function of position in the bed (e.g., distance above the distributor) and not affected by increasing the bed height above this position (e.g., by adding sand to the bed). Through the use of the Bode plot, the shifting of frequency peaks with an increase in fluidization velocity was documented to be a continuous growth. Large-diameter, high-density particles

(Group D) exhibited harmonic behavior, while small-diameter, low-density particles (Group A) yielded power spectrums with first-order characteristics. When pressure fluctuations were measured over a temperature range from ambient to above 500° C, power spectrums varied little when velocity ratios were kept within a tight range (1.3 – 1.5). These tests showed that temperature had only a small influence on the spectrums for the test conditions. Multiple-peak phenomena were examined and related to bubble effects, and peaks in the power spectrums were associated with bubble coalescence, bubble surface effects, and jetting effects at the distributor.

Using the information from these tests, a second-order system model that describes the location and magnitude of the dominant peak was developed. An equation for the natural frequency as a function of bed height was developed from experimental data and shown to agree with theories in the literature. An equation for the damping ratio as a function of bed height was developed from experimental data and shown to yield the same trend as a new theoretical damping ratio presented in this research. Using these two equations for the natural frequency and damping ratio, the model was developed such that its output was a function of bed height. This output was compared to the experimental data and shown to qualitatively describe the experimental spectrums adequately.

CHAPTER 1. INTRODUCTION

Fluidized beds have been utilized in industry for over 60 years for such processes as coal gasification and synthetic fuel catalytic cracking. From their initial use, researchers have recognized the link between a fluidized bed's performance and the pressure fluctuations within the bed. Even though a large amount of research involving these pressure fluctuations has been conducted, the phenomenon is still not well-understood.

The goal of this dissertation is to increase the understanding of the pressure fluctuations in a fluidized bed. Three main areas exist that will be benefited by this work. The first area is hydrodynamic and heat transfer similitude. As in other industries, small-scale testing is done to evaluate an initial design. When specific goals are met at the small-scale testing, the process moves to large-scale prototype (or production) testing. In the case of fluidized beds, researchers have experienced problems with reactor performance when making this jump to a larger scale. Currently, the power spectrums of the fluidized bed as measured through the pressure fluctuations are compared to determine if similitude is attained [1-4]. By understanding how the characteristics of this spectrum relate to the fluidized bed operation, the correct pressure fluctuation criteria can be chosen for similitude validation.

The second area involves chemical processes associated with a fluidized bed. Past research has shown that the pressure fluctuations in fluidized beds are linked to the chemical processes occurring in the reactor such as the adsorption and desorption of gases on the surface of catalyst particles [5] and the combustion of bubbles in a bed fluidized with methane and air [6]. By understanding how the pressure fluctuations are affected by changes in bed parameters, these chemical processes can be better controlled through the fluidized bed parameters.

The third area that will be benefited is the use of pressure fluctuations as a diagnostic tool for fluidized bed performance and fluidization regime identification [7-10]. Researchers have shown that a change in bed performance as measured through the pressure fluctuations can be used to determine if a bed is experiencing problems such as agglomeration [7]. The power spectrum may also be used to identify in which fluidization regime the bed is

operating [8-10]. A more thorough understanding of the pressure fluctuations will then lead to improved diagnostic and regime identification techniques.

Because testing methods have varied widely among researchers, any conclusions drawn between these studies are questionable. Brue and Brown have investigated the sampling and analysis techniques used to measure the pressure fluctuations and to determine the corresponding power spectrums [1,11, 12]. Unfortunately, a large variation still exists in several other areas of pressure fluctuation testing. For example, testing has been done with several variations of pressure probe techniques including absolute, differential, static, and dynamic variations, but no study has adequately described the differences between each of these techniques. To address this issue, the first objective of this dissertation is to examine the differences between these probe techniques employed in the literature. The pressure measured with each of these techniques is studied with spectral analysis techniques. Differences between these techniques are described qualitatively by plotting the power spectrums on a Bode plot and examining the results. The use of the Bode plot to describe pressure fluctuations is a relatively new method and offers important information about the power spectrums, as opposed to a single data point (e.g., the dominant frequency) used to describe an entire spectrum. The increase in understanding of the different probe techniques through this testing offers insight into which type of probe technique should be used for the modeling of the power spectrums.

The research areas involving similitude, chemical reaction, and diagnostic effects are all benefited through an increase in the understanding of pressure fluctuations. To achieve this understanding, the second objective of this dissertation is to acquire pressure data over a range of bed heights, fluidization velocities, particle diameters, particle densities, and bed temperatures, and then to examine the corresponding power spectrums in the frequency domain. As the Bode plot has only been used to interpret pressure fluctuation data over the past few years, it will be used to provide a fresh view of the differences between power spectrums under the given test conditions. Multiple-peak phenomena will also be examined to determine the relationship between the peaks in the spectrums and the bed parameters. The physical significance of several peaks will be determined.

To date, no researcher has developed a model that adequately describes fluidized bed pressure fluctuations in the frequency domain. Brue's work represents an initial attempt to model peaks in the power spectrums using second-order systems [1,2,11,12], but much work is needed to extend this idea. The last goal of this dissertation will be to develop a second-order model that describes the dominant frequency of the pressure fluctuations in the frequency domain. As opposed to an equation that relates a bed parameter (e.g., bed height) to the location of the dominant frequency, this model will also determine the magnitude of the dominant frequency in the power spectrum. (This will provide the initial step towards an expanded model that includes secondary peaks. Such an expanded model could predict when one peak becomes dominant over another and other multiple-peak phenomena.) The output from this model's equation will be a function of bed height and describe the location and magnitude of the dominant frequency for a given bed height range. The model's output will be plotted with the experimental data on a Bode plot to assure that the model qualitatively describes the experimental data adequately.

CHAPTER 2. LITERATURE REVIEW

Chapter 2 is divided into two main sections. The first section provides a brief background on fluidized bed fundamentals. Unless otherwise stated, this review will only deal with two-phase systems in which a gas is used as the fluidizing medium and the bed material is comprised of solid particles. A more thorough review can be found in [13]. The second section of this chapter discusses research that has been done involving pressure fluctuations in fluidized beds. The five main parts of this section include examples of pressure probe techniques, the pressure analysis techniques, the effect of bed parameters on the pressure fluctuations, the presence of multiple-peak phenomena and associated bubble effects, and the relation of pressure fluctuations to second-order systems.

Fluidization Fundamentals

A fluidized bed is a type of reactor that uses gas to 'fluidize' or levitate particles by using the force of the gas to balance the weight of the particles. Fluidized beds have a large assortment of configurations, but the type relative to this study contain three essential parts: a plenum, a distributor plate, and a bed section. The gas is provided to the plenum at the bottom of the fluidized bed and is distributed evenly to the bed through a distributor plate. The gas then fluidizes the bed particles, passes through the freeboard, and out of the bed. The bed sections can be cylindrical, square, or rectangular in cross-section. An example of a fluidized bed is illustrated in Figure 2.1.

Fluidized beds offer high mixing rates, high heat transfer rates, and isothermal operation in some regimes. Because of their wide range of capabilities, fluidized beds are used for several different processes. Among these are pyrolysis reactors, coal gasification, heat exchangers, metal coating operations, and combustion reactors.

If a relatively small amount of gas is passed through the bed, the bed material remains fixed (packed) and no pressure fluctuations are present in the bed. If the amount of gas is increased, a point is reached where the force provided by the gas balances the weight of the particles. This point is known as minimum fluidization, and the velocity of the gas at this point is referred to as the minimum fluidization velocity. Small pressure fluctuations appear

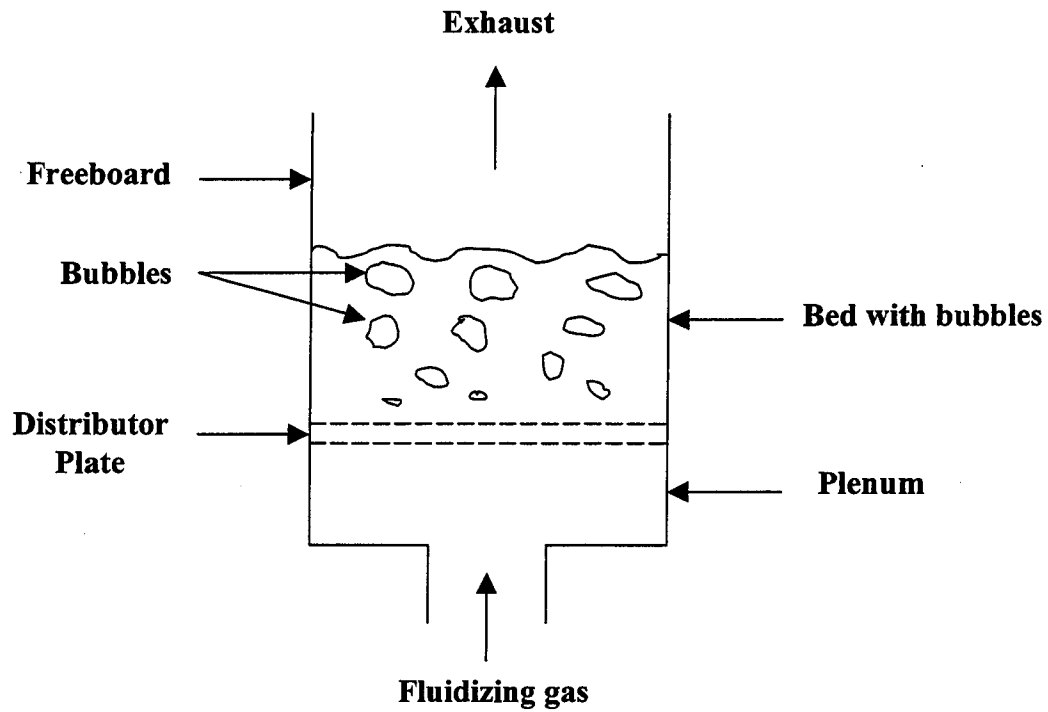


Figure 2.1: Illustration of a fluidized bed

in the bed at the onset of fluidization. Figure 2.2 shows how the pressure drop in the bed increases linearly with fluidization velocity in the fixed bed, and then remains nearly constant with an increase in fluidization velocity after the minimum fluidization velocity (labeled as “ u_{mf} ” in the figure) is reached.

Once minimum fluidization is reached, the bed attains characteristics similar to those of a liquid. Under certain conditions, the top surface of the bed may ‘slosh’ around the bed column. When the fluidized bed is tipped, the top surface remains horizontal, similar to how water in a cup would react when the cup is tipped. Many of the bed properties are best described by the mixture of gas and particles (known as the emulsion) instead of the individual properties of the gas and particles. For example, bubbling fluidized bed (BFB) heat transfer correlations may be defined in terms of the emulsion density rather than the density of each phase.

Depending on the type of particle in the bed and fluidization velocity, several different fluidization regimes can be achieved beyond the fixed bed. After minimum

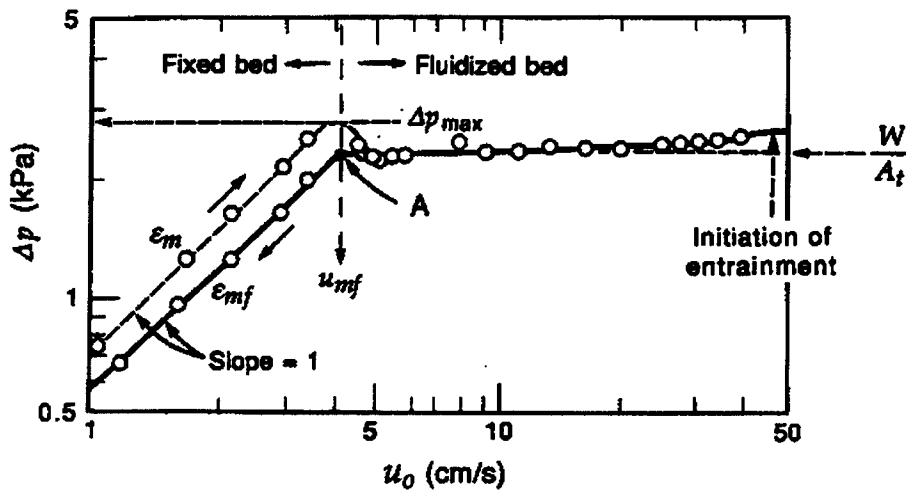


Figure 2.2: Pressure differential in a fixed and fluidized bed [13]

fluidization is reached, the bed may experience a smooth fluidization or bubbles may appear in the bed depending on the type of bed material. A further increase in velocity will place the bed in a slugging regime in which the bubble growth may reach a permanent size, and the slug is spherical or flat in appearance. In this regime, the slug may occupy nearly the entire cross-section of the bed. At fluidization velocities beyond this, the solid particles are elutriated from the bed, and turbulent fluidization or lean phase fluidization is reached. Two characteristics of the turbulent fluidization regime include the top of the bed being elutriated with the gas and a lower-density phase as compared to the smooth or bubbling fluidization. The lean phase regime characteristics include very high elutriation rates and low particle content in the bed. The different fluidization regimes described above are illustrated in Figure 2.3.

The fluidized bed characteristics depend on the type of material used. Geldart [14] created a particle classification system based on the particle diameter and the density difference between the particle and fluidizing medium (gas or liquid). This system has four different classifications, defined as Groups A, B, C, and D. Figure 2.4 shows the relationship between the four groups.

Starting with the lowest diameter, Group C particles are usually difficult to fluidize because of interparticle forces causing cohesive effects. Group A particles are easily

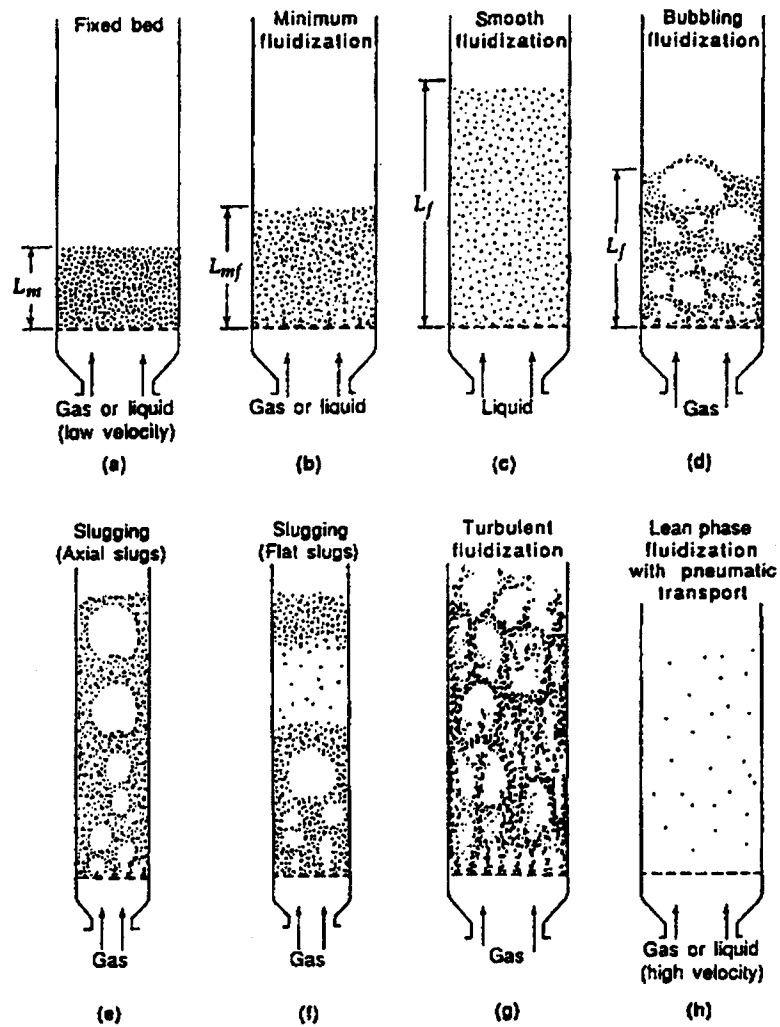


Figure 2.3: Different fluidization regimes [13]

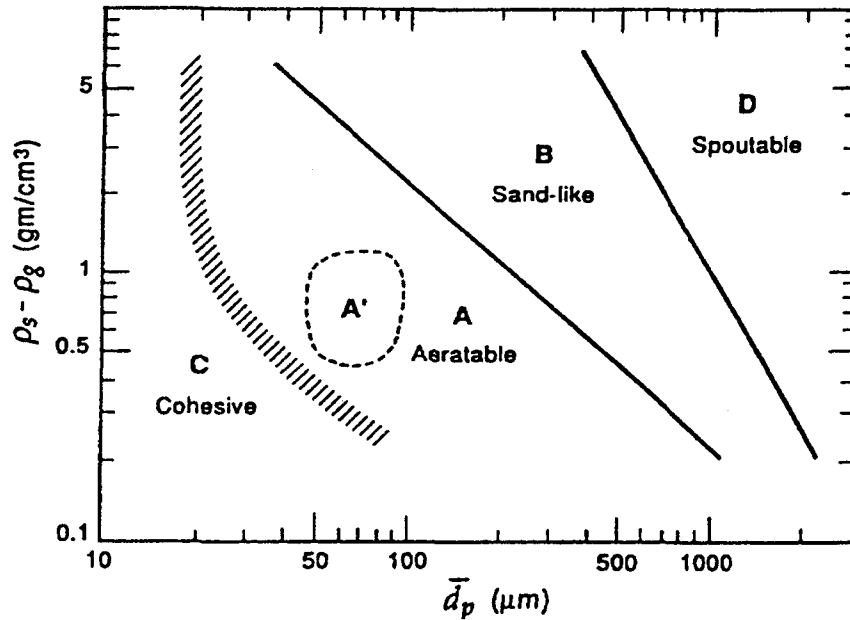


Figure 2.4: Geldart classification system [14]

fluidized and able to operate in the smooth fluidization regime without bubbling. The velocity must be increased above the minimum fluidization velocity to induce bubbling in fluidized beds with Group A particles, and the bubbles generated are predominantly small. In contrast, bubbling in the bed occurs at the onset of fluidization with Group B particles. The extensive bubbling found in beds with Group B particles leads to high mixing rates desired in many industrial processes. Group D is designated for the largest particles of the four classifications. The larger particles need a relatively larger flow of gas to achieve fluidization, and the flow regime is usually characterized by slugging instead of the smooth or bubbling fluidization seen with Groups A and B particles, respectively. Figure 2.4 also provides a heuristic for bubble development: the size of the bubble in fluidized beds increases as the particle density and diameter is increase from low-density/small-diameter particles (which produce small bubbles or no bubbles at all) to high-density/large-diameter particles (which produce large bubbles or slugs). Figure 2.5 shows the fluidization regimes achieved with increases in fluidization velocity for each of the Geldart classification groups.

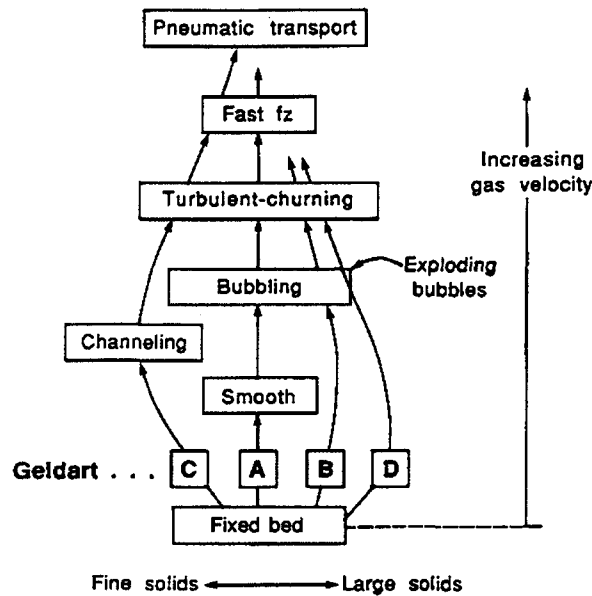


Figure 2.5: Particle classifications and fluidization regimes [13]

Pressure Fluctuations in Fluidized Beds

The following section describes several issues involving pressure fluctuations in fluidized beds. These issues include the different probe techniques used to acquire the pressure fluctuations, the analysis techniques used to study the fluctuations, characteristics of these fluctuations, and the relationship between these fluctuations and second-order systems.

Pressure probe technique and probe arm position

Pressure fluctuations in fluidized beds have been studied using several different techniques, including pressure transducers, thermocouples, capacitive probes, video cameras, and conductivity cells [15]. Of all these techniques, the use of pressure transducers is the most prevalent. Several different types of pressure transducers are available (e.g., diaphragm or piezoelectric) that may be used to measure the absolute and differential pressures in the bed with the openings of the probe arms at different alignments. These alignments may orientate the opening of the probe arm so that it is aligned perpendicular, parallel, or at other angles to the flow through the bed. Regarding the effect of the probe arm on the bed phenomena, Rowe and Masson [16] have shown interesting effects that occur with different

probe arms as they encounter bubbles. These probe effects include elongating and accelerating the bubbles, along with changing their path so that the bubbles travel up the probe arm. They described the effect of the probe arm on the position, shape, and velocity of the bubbles with photographic methods, but they did not examine the effects in the frequency domain.

The four techniques discussed in this research for acquiring pressure fluctuation data are listed below along with an example of each technique in the literature. In each of these techniques, the probe arm (or stem) was placed directly into the fluidized bed. The literature also provides examples where the pressure fluctuations were measured at the bed wall [12,17] or in the plenum [18,19].

The static-absolute pressure probe technique

Figure 2.6 provides an example of the static-absolute technique. Fan et al. [20] used this technique to investigate the characteristics of pressure fluctuations in a bed operating at high temperatures (up to 700° C).

A rectangular slot was cut into the side of the probe arm (as shown in Figure 2.6 (A) and (B)), and the arm is labeled as “8” in Figure 2.6 (C). In this figure, the probe arm is positioned vertically in the bed and fastened to the top cover of the bed. This probe technique is labeled as “static-absolute” because the opening of the probe arm was parallel to the flow (static) and the pressure was being measured at only one position in the bed (absolute).

The static-differential pressure probe technique

An example of the static-differential technique used by Clark and Atkinson [21] is shown in Figure 2.7. This technique was used to study the effect of probe geometry and transducer type on the measured pressure fluctuations.

In this figure, both probe arms are positioned horizontally in the bed and held in place by a fitting at the bed wall. This probe technique is labeled as “static-differential” because the opening of the probe arm was parallel to the flow (static) and the pressure was being measured at two positions in the bed (differential).

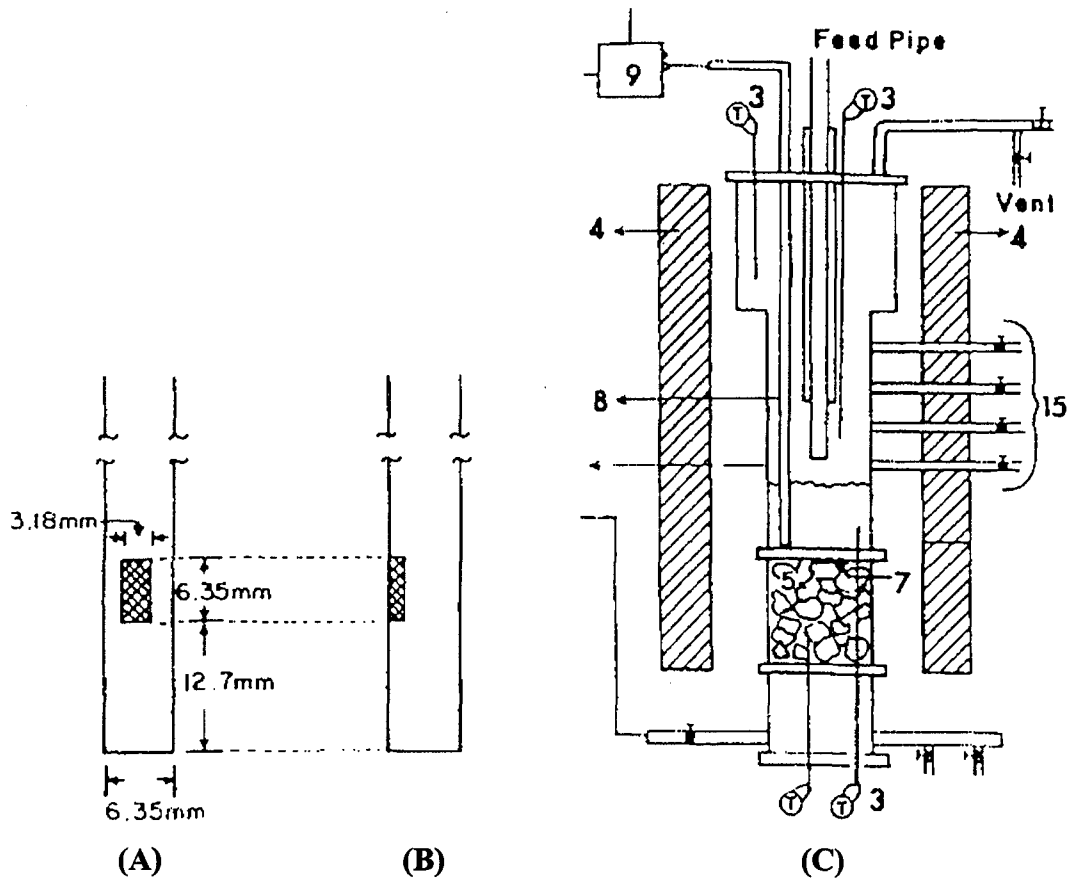


Figure 2.6: The static-absolute pressure probe technique used by Fan et al. [20] with a front view of the probe arm (A), a side view of the probe arm (B), and the probe arm (8) positioned vertically in the bed (C)

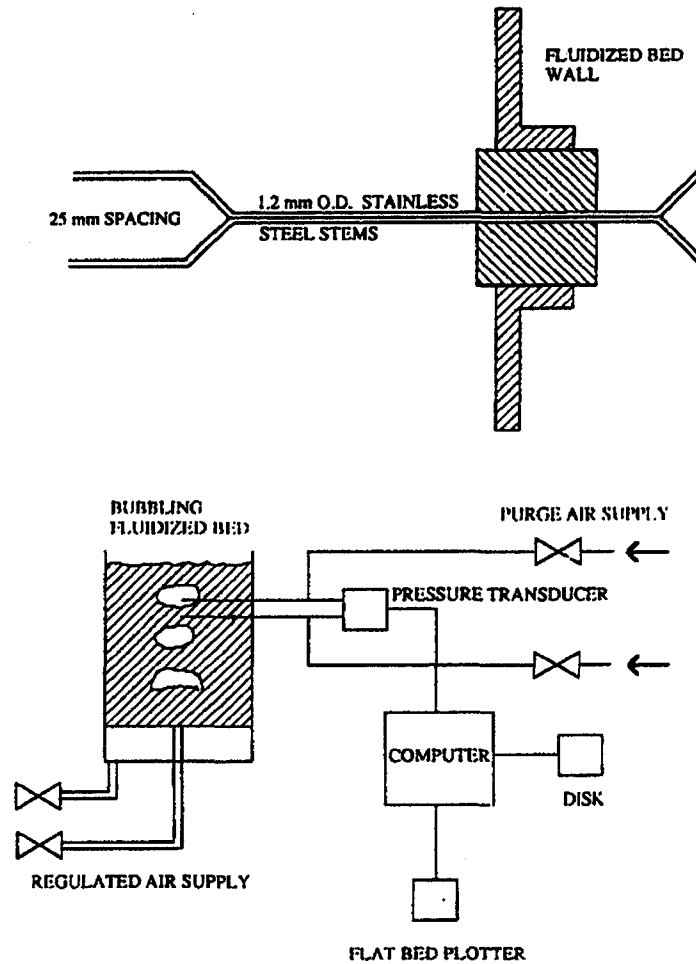


Figure 2.7: The static-differential pressure probe technique used by Clark et al. [21]

The dynamic-absolute pressure probe technique

Figure 2.8 provides an example of the dynamic-absolute technique. Svoboda et al. [22] used this technique to investigate the characteristics of pressure fluctuations in a bed operating at high temperatures (up to 800° C).

The probe in this figure was aligned vertically in the bed and held in place by a special construction above the reactor. This probe technique is labeled as “dynamic-absolute” because the opening of the probe arm was perpendicular to the flow (dynamic) and the pressure was being measured at only one position in the bed (absolute).

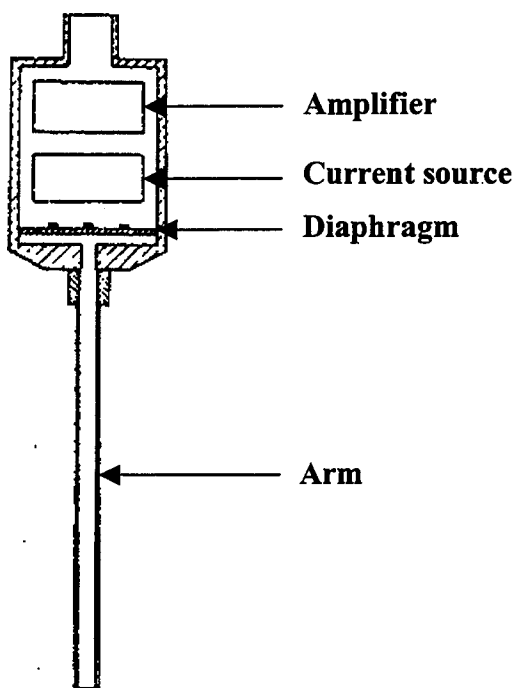


Figure 2.8: The dynamic-absolute pressure probe technique used by Svoboda et al. [22]

Botterill and Hawkes [23] used a hybrid of the dynamic-absolute and static-absolute techniques discussed above. This hybrid used a single probe arm that was inclined downward into the bed at sixty degrees.

The dynamic-differential pressure probe technique

An example of the dynamic-differential technique is shown in Figure 2.9. This technique was used by Dent et al. [24] to study bed characteristics such as bubble rise velocity.

This figure shows two sets of the dynamic differential technique. The probe arms were inserted horizontally and bent ninety degrees so that the opening was perpendicular to the flow. This probe technique is labeled as “dynamic-differential” because the opening of the probe arm was perpendicular to the flow (dynamic) and the pressure was being measured at two positions in the bed (differential).

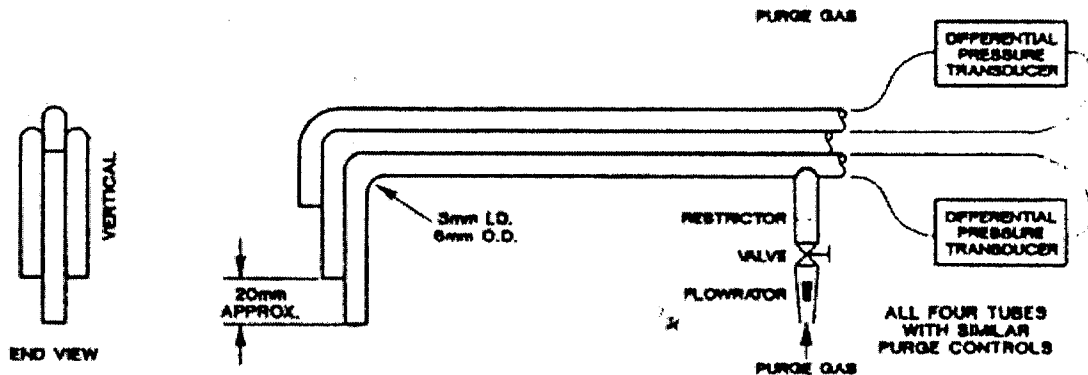


Figure 2.9: The dynamic-differential pressure probe technique used by Dent et al. [24]

Comments on probe technique differences

Regarding the absolute and differential pressure probe techniques, the general understanding is that absolute pressure probes measure global bed phenomena, while differential pressure probes measure local phenomena [25,26]. Roy and Davidson [25] have shown that differences do exist between the two techniques. Figure 2.10 shows two power spectrums from Roy and Davidson that used absolute and differential pressure probes. As observed in this figure, the dominant frequency varies significantly between the two techniques, as it is about 3 Hz with the single probe measurement and over 5 Hz with the double probe measurement.

Agreeing with Roy and Davidson [25], Bi et al. [26] also make reference to absolute probe techniques measuring global phenomena and differential techniques measuring local phenomena through filtering common signals measured at each probe opening. Furthermore, Bi et al. discuss the importance of the vertical spacing between the differential probe openings for testing involved with characterizing bubble phenomena. They comment that “if the spacing between the two ports is too large, poor signal correlation and strong interference from extraneous pressure waves prevents accurate measurement of local bubble properties.”

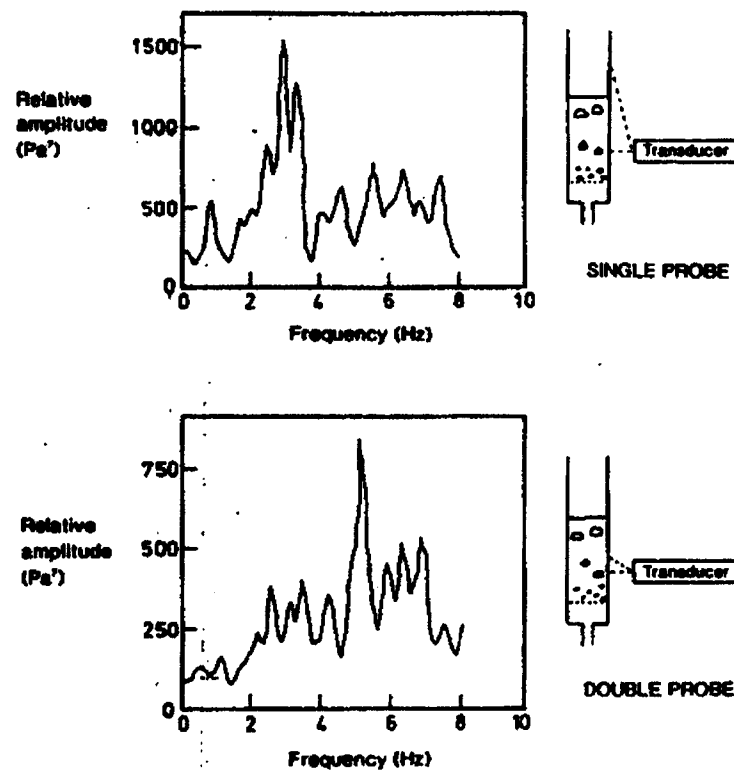


Figure 2.10: Absolute (single, above) and differential (double, below) pressure probe techniques [25]

These comments on the importance of probe spacing agree with those presented by Sitnai et al. [27].

Few researchers [22,24] have commented on the differences between static and dynamic techniques, but the general understanding is that the two techniques provide similar results. Svoboda et al. [22] commented that static and dynamic probe techniques produced the same results when determining the type of probe to use for high-temperature testing. Dent et al. [24] also used both static and dynamic probes to measure bubble characteristics with a differential probe and did not comment on any differences observed between the two techniques.

Probe arm position in the bed

Several researchers [22,28,29] have commented that pressure fluctuations have characteristics that vary along the vertical axis of the bed. Dhodapkar and Klinzing [28]

attributed these differences to bubble effects, as small-diameter bubbles dominate the lower positions in the bed and large-diameter bubbles dominate the upper portion of the bed.

An example of different frequency peaks being present in the power spectrums measured at different axial positions in the bed is provided by Van der Schaaf et al. [30] in Figure 2.11. This figure shows two different axial positions (0.14 m and 0.44 m) that have a dominant peak at 0.43 Hz. When the axial position from the distributor plate was increased to 0.74 m above the distributor plate, a second peak at 0.82 Hz appeared and was dominant. A further increase of the arm position to the surface showed a lower-magnitude dominant peak at 0.75 Hz. The change in peaks were attributed to different “modes” of oscillation being excited. Brue and Brown [2] have observed similar changes in peak dominance between two frequencies with changes in the arm position in the bed. Because the frequency phenomena has been shown to be a function of position in the bed, the position of the probe arm is an important testing parameter.

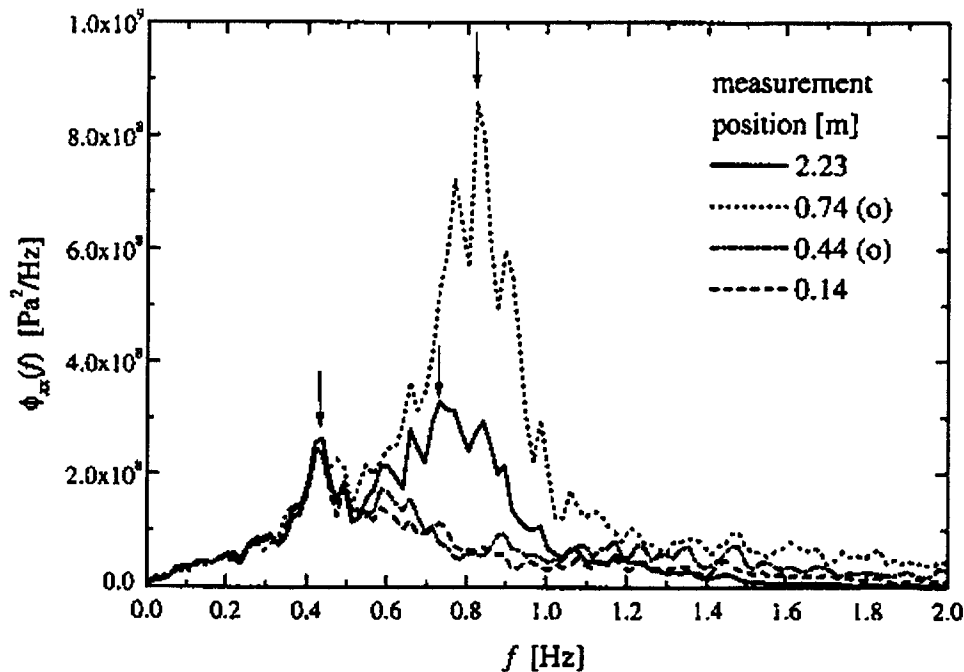


Figure 2.11: Example of the dominant frequency changing with axial position in a bubbling fluidized bed [30]

The relationship between pressure phenomena and radial position within the bed is not well-documented. Van der Schaaf et al. [30] document one case where a secondary peak was located in the power spectrum at one radial position, but not another. No explanation for this occurrence was given. Musmarra et al. [31] showed that there was some attenuation of the pressure signal in the time domain when the pressure measurement was at the wall as opposed to the center of the bed, although no description of the differences were given in the frequency domain.

Pressure fluctuation analysis techniques

Statistical, time-domain, and frequency-domain analysis techniques have all been used to describe pressure fluctuations in a fluidized bed. In this section, examples of researchers that used these techniques are given. An explanation of each of the techniques mentioned below is provided in Chapter 3.

In the earliest studies of pressure fluctuations in fluidized beds, Tamarin [32] and Hiby [33] used visual observation of the pressure signals with time to determine the frequency of the pressure fluctuations. Kang et al. [34] were among the first to use signal analysis techniques to describe the time and frequency characteristics of the pressure fluctuations. These techniques included the probability density function (PDF), the root mean square of the pressure fluctuations (RMS), and the power spectral density (PSD) technique. Figure 2.12 shows an example PSD from their research. The PSD technique is the most widely used method for studying pressure fluctuation phenomena in fluidized beds.

Lirag and Littman [17] extended the analysis techniques used by Kang et al. to include the autocorrelation function and crosscorrelation function. The autocorrelation function (ACF) was used to determine if a periodic phenomenon existed in the bed pressure fluctuations, while the crosscorrelation function (CCF) was used to determine if the pressure fluctuations in the bed occurred slightly before the pressure fluctuations in the plenum. They used the time lag from the crosscorrelation function and the distance between probes to calculate the propagation velocity of the pressure wave. Fan et al. [29] used these two

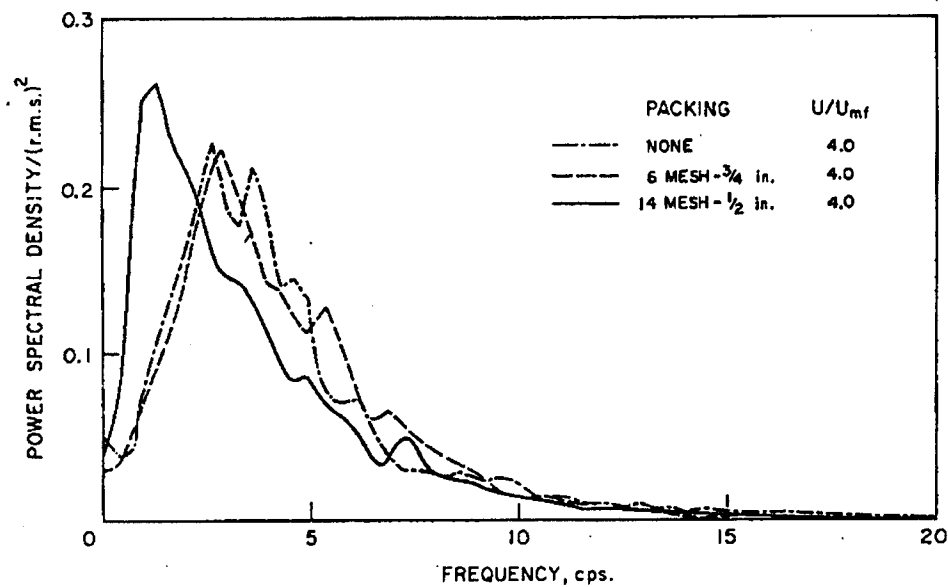


Figure 2.12: The use of the PSD technique to describe pressure fluctuation data [34]

functions in a similar manner. Clark et al. [35] also discussed the ACF, PSD, and Fast Fourier Transform (FFT) techniques and provided examples of each with a slugging fluidized bed.

Brue [11] was the first researcher to use a Bode plot to study the power spectrums of fluidized beds. The Bode plot technique encompasses taking the logarithm of the power spectrum (or PSD) and plotting it against the logarithm of the corresponding frequencies. By performing this transformation, Brue discovered several important characteristics of the pressure fluctuations in the power spectrum that were not previously observed. First, low-magnitude, secondary peaks that were not apparent with the PSD technique were easily observed in the Bode plot. Second, bubbling fluidized beds were shown to have characteristics (e.g., -40 dB/decade decay slopes) similar to second-order dynamic systems.

Pressure fluctuation characteristics

Studies on the pressure characteristics in packed beds provided the basis for fluidized bed research. Darcy [36] determined that the pressure gradient in a packed bed is proportional to the velocity and viscosity of the gas. Ergun [37] expanded on this relation for flow through a packed bed in the laminar and turbulent regions by including particle diameter

and voidage effects. With this foundation in place, the first relevant studies on fluidized beds were carried out (e.g., [32]). The following section describes the relationship between the pressure fluctuations observed in fluidized beds and bed height, fluidization velocity, particle density/diameter, and bed temperature.

Bed height effects

Hiby [33] was the first researcher to relate the periodic nature of the pressure fluctuations in a fluidized bed to a “natural frequency” occurring in the bed, and he developed an equation for this periodic nature shown in Equation 2.1.

$$\omega_n = \frac{2}{\pi} \sqrt{\frac{g \cdot (1 - \varepsilon)}{3 \cdot H_{mf} \cdot \varepsilon}} \quad (2.1)$$

In this equation, “ ω_n ” is the natural frequency of the bed, “ g ” is gravity, “ ε ” is the bed voidage, and “ H_{mf} ” is the bed height at minimum fluidization.

This equation was derived through a force balance on an individual particle. Hiby combined this force balance with the Ergun equation to describe the pressure force throughout the entire bed. Hiby estimated that Equation 2.1 was valid for shallow beds with heights of about ten particle diameters. As bed height was increased, the fluctuations became more random. Even at the higher bed heights, the relationship of frequency being inversely proportional to the square root of bed height held fairly well up to bed heights of five hundred particle diameters.

Equations showing the same relationship between the natural frequency and bed height have been developed by Baskakov [38] and Sun et al. [39,40] (with the comments of Bi and Grace [41]). Other researchers have also confirmed this relationship with experimental data [29,42], and have commented that the bed height range that this relationship is valid extends to bed heights over one thousand particle diameters.

Verloop and Heertjes [43] studied the pressure fluctuations and determined that the phenomena was due to bubble inception at low bed heights (agreeing with Hiby) but that a slugging phenomena becomes dominant once a critical bed height is reached. This bed

height is on the order of a few hundred particle diameters. Using an energy balance on the entire bed, they derived the following equation for the natural frequency of the bed.

$$\omega_n = \frac{1}{2 \cdot \pi} \sqrt{\frac{g \cdot (2 \cdot \varepsilon)}{H_{mf} \cdot \varepsilon}} \quad (2.2)$$

This equation is valid up to a critical bed height, above which slugging occurs. The frequency relationship for slugging (ω_s) is given below in Equation 2.3, where “ D_b ” is the bed diameter.

$$\omega_s = 0.35 \cdot \frac{\sqrt{g \cdot D_b}}{H_{mf}} \quad (2.3)$$

For the moderate gas velocities and geometric (height-to-diameter) ratios in this study, other researchers have shown similar dependence of frequency with height and diameter at slugging [44,45]. Baeyens and Geldart [44] developed a similar equation for the slugging frequency of the bed, and this frequency was shown to occur at high bed depths or at high velocities. Figure 2.13 illustrates how the slugging frequency decreases with an increase in height until a certain height is reached. Above this certain height, the slugging frequency is independent of height.

Fluidization velocity effects

The effect of fluidization velocity on the frequencies in the power spectrum is not well-understood, but several researchers have shown that increasing the velocity will generally increase the dominant frequency [1,17,30]. In Figure 2.14, Van der Schaaf et al. [30] show two different frequency phenomena (designated by the two lines) increasing with an increase in fluidization velocity and then leveling off. The minimum fluidization velocity for this test was 0.14 m/s, and the trend levels off at a velocity ratio (u/u_{mf}) of about 4.

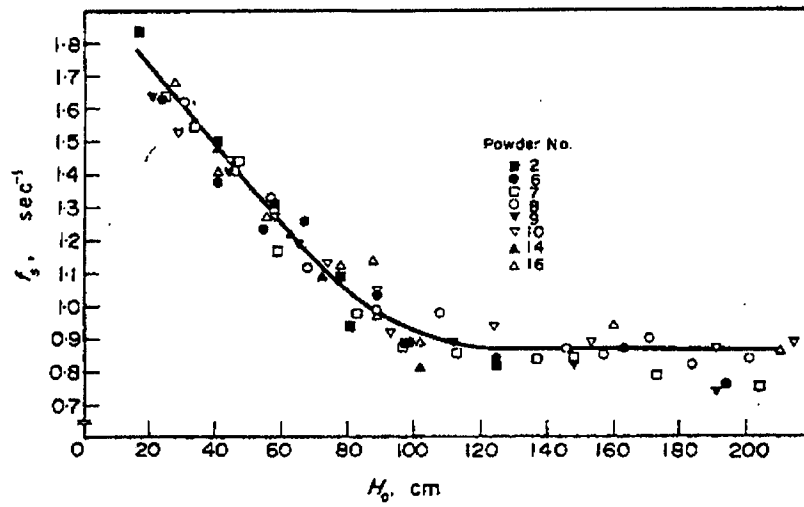


Figure 2.13: Relationship of slugging frequencies with bed height [44]

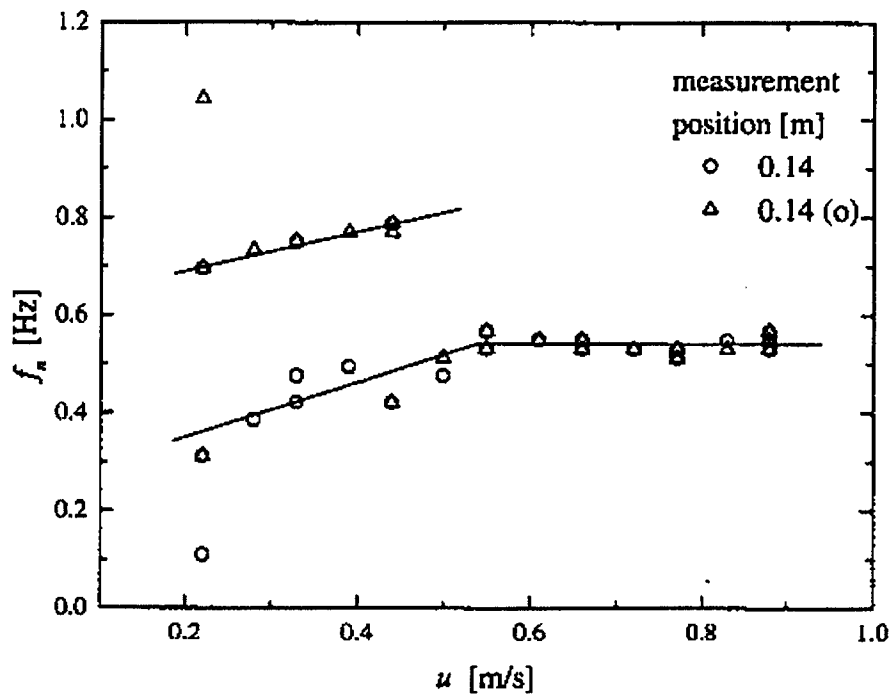


Figure 2.14: The effect of velocity on dominant and secondary frequencies [30]

For the trend observed in Figure 2.14, the authors did not provide a reason for the dominant frequency increasing with an increase in fluidization velocity, but the reason is generally attributed to bubble phenomena. For example, Fan et al. [46] measured the bubble rise velocities in the bubbling, slugging, and turbulent fluidization regimes, as shown in Figure 2.15. They showed that the dominant frequency and the bubble rise velocity both increased as the fluidization velocity increased in the bubbling regime. At the transition from the bubbling regime to the slugging regime, a “jump-like” drop in the bubble rise velocity occurred. This transition coincides with the transition from bubbling to slugging observed at the critical height presented by Verloop and Heertjes [43].

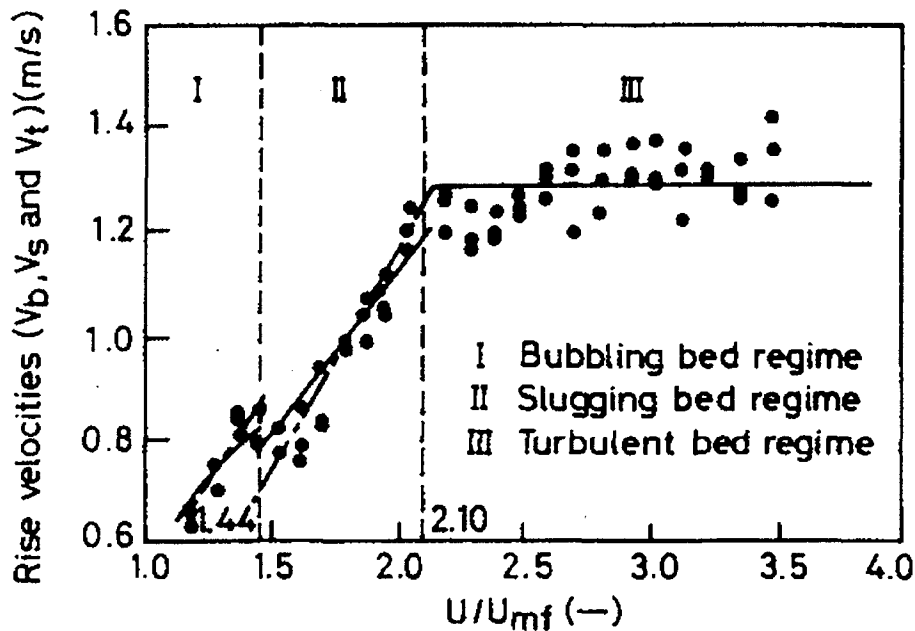


Figure 2.15: The effect of fluidization velocity ratio on bubble (V_b), slug (V_s), and turbulent (V_t) rise velocities in the bubbling (I), slugging (II), and turbulent (III) regimes [46]

Particle diameter/density effects

The relationship between particle diameter/density effects and fluidization regimes has been illustrated previously in Figures 2.4 and 2.5. As shown in Figure 2.5, slugging (or turbulent churning) often occurs in beds fluidized with Group D particles. The criteria for

determining if a bed is slugging is generally concluded through visual observation [44], but other methods involving the amplitude of the pressure fluctuations [47], the presence of pressure fluctuation minima [44], or the ratio of the bubble size to the bed diameter [13] have been used. Power spectrums from fluidized beds generally have only a single peak or a peak that is considerably more dominant than any secondary peak. An example of a power spectrum from a slugging bed fluidized with Group D particles is provided by Clark et al. [35] in Figure 2.16. In this spectrum, a peak at 1.75 Hz is considerably more dominant than a secondary peak at 3.5 Hz. The authors do not comment on the fact that the secondary peak is twice that of the first.

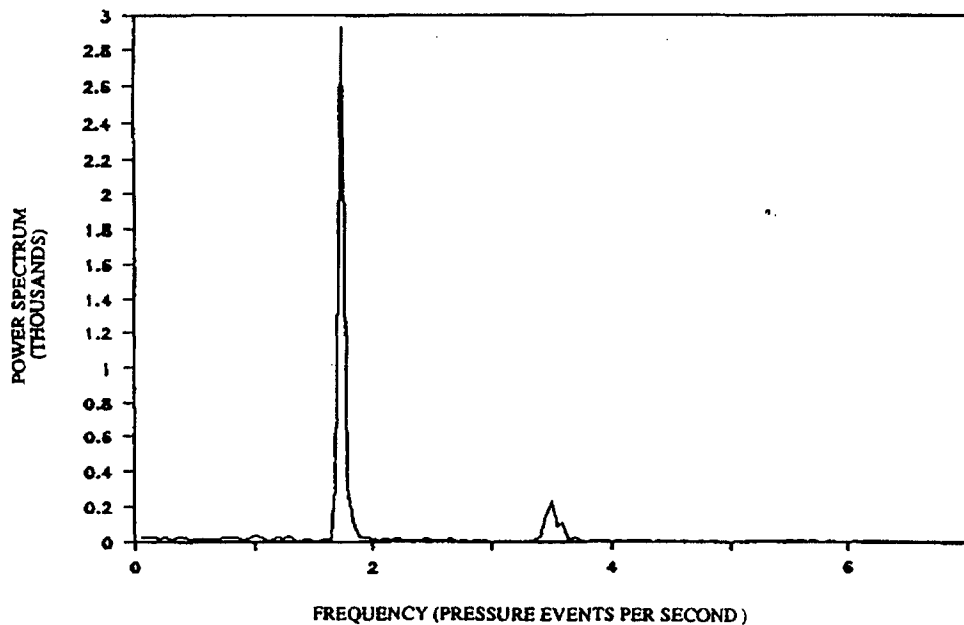


Figure 2.16: Example of a power spectrum from a slugging fluidized bed [35]

Group A particles are generally tested with Group B without any distinction made between these particles [28,45]. For example, Roy et al. [45] use frequency data from both Group A and B particles to determine a correlation for the natural frequency of a slugging bed, while Dhodapkar and Klinzing [28] provide examples of power spectrums from Group A and B particles that have similar characteristics.

Bed temperature effects

Very few studies exist that describe the effect of bed temperature on bed pressure fluctuations, mainly due to the difficulties associated with measuring the fluctuations at the high temperatures. Svoboda et al. [22] measured pressure fluctuations in a fluidized bed across a temperature range of 20° C to 700° C. Figure 2.17 shows how the dominant frequency plotted against the fluidization velocity ratio for the bed operating at 20° C (1), 450° C (2), and 700° C (3). Their testing showed that the dominant frequency increased significantly when the bed temperature was increased in the freely bubbling regime (between a velocity ratio of about 1 to 1.3). This coincides with several other researchers who saw an increase in bubble frequency over the same temperature range using optical and capacitive probes [48-50]. At higher gas velocities, a lower frequency became dominant. They described this change in regimes as a “jump-like change” in the dominant frequency and tried to correlate this lower dominant frequency to the slugging frequency of the bed. In the free-bubbling regime, they were not able to explain the large jump in frequency with temperature.

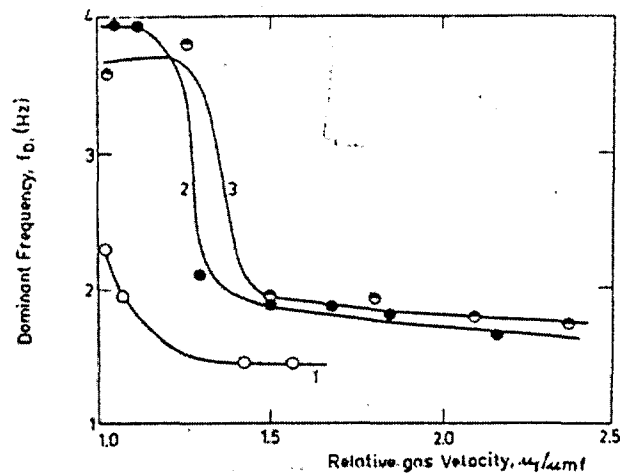


Figure 2.17: The influence of velocity ratio on the dominant frequency with the bed operating at bed temperatures of 20° C (1), 450° C (2), and 700° C (3) [22]

As shown in Figure 2.18, Fan et al. [20] provided information on the dominant frequency's dependence on temperature that was considerably more complicated than the

data provided by Svoboda et al. [22]. In this figure, lines are drawn through points of common fluidization velocity ratio. The lack of a smooth trend between dominant frequency and bed temperature is highly apparent, but some general comments can be stated. First, the frequency increased and then decreased over the temperature range at a velocity ratio of 1.0, which agreed with Svoboda et al. At velocity ratios above 1 and temperatures above 200° C, the dominant frequencies tended to stay within a frequency range of 4 to 5 Hz.

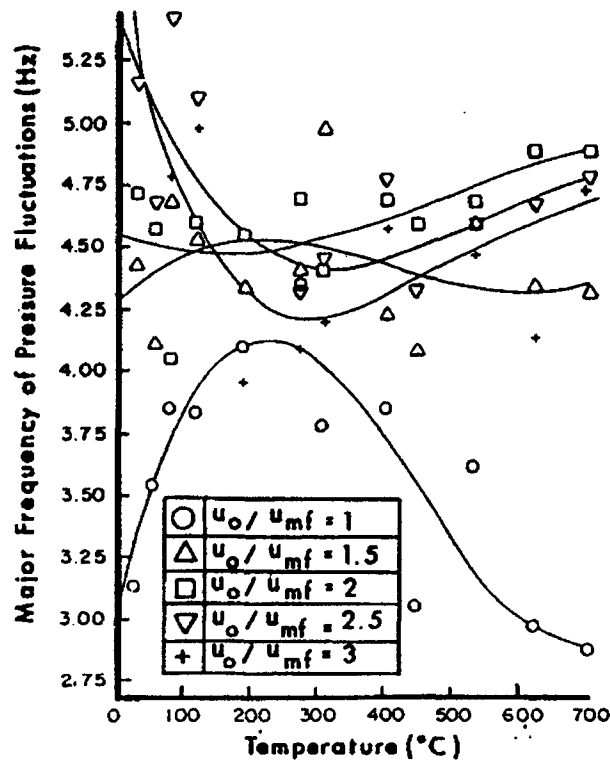


Figure 2.18: The effect of temperature on dominant frequency [20]

Multiple-peak phenomena and physical mechanisms

The following section is divided into two parts. The first part provides several examples of multiple-peak frequency phenomena present in the power spectrums of fluidized beds, and the second part describes the bubble-related physical mechanisms that are associated with the peak phenomena.

Examples of multiple-peak phenomena

In most of the studies discussed above, only the dominant frequency in the power spectrum is discussed, and any secondary peaks in the spectrum are not mentioned. Svoboda et al. [22] were one of the first research teams to discuss the presence of multiple-peak phenomena in the power spectrum. Figure 2.19 shows an example of a power spectrum from Svoboda et al. with three peaks present at 2.0, 2.6, and 3.8 Hz. They also provided tabular data that showed the changing of dominance between two peaks as the velocity was increased (the “jump-like” changes in Figure 2.17). As explained previously, they attributed this to a slugging effect becoming dominant over a bubbling effect as fluidization velocity was increased.

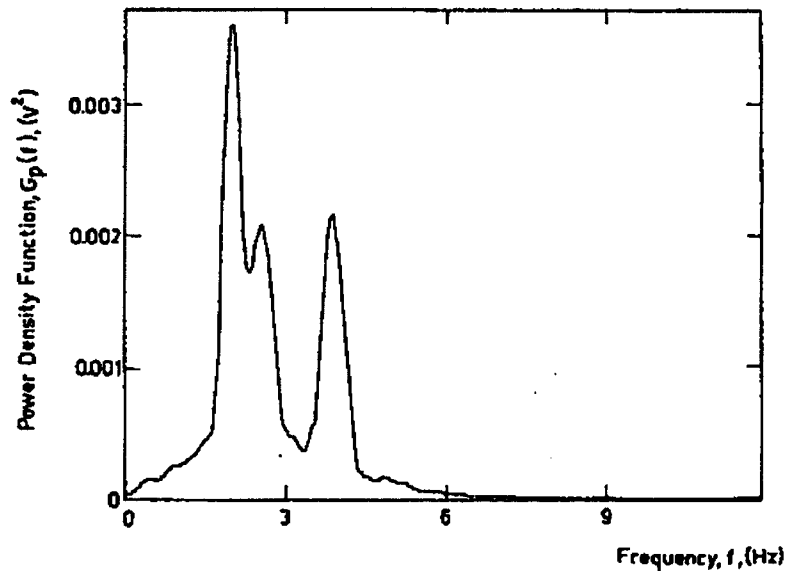


Figure 2.19: An example of multiple-peak phenomena in the power spectrum of a fluidized bed [22]

Kage et al. [19] studied pressure phenomena in a BFB by measuring the pressure fluctuations in the plenum. In several cases, they observed three peaks in the power spectrum and identified these peaks as the eruption frequency, bubble generation frequency, and the natural frequency of the bed. Figure 2.10 gives an example of one of these power

spectrums showing the bubble generation frequency (F_g), the bubble eruption frequency (F_e), and the natural frequency of the bed (F_b) labeled on the figure.

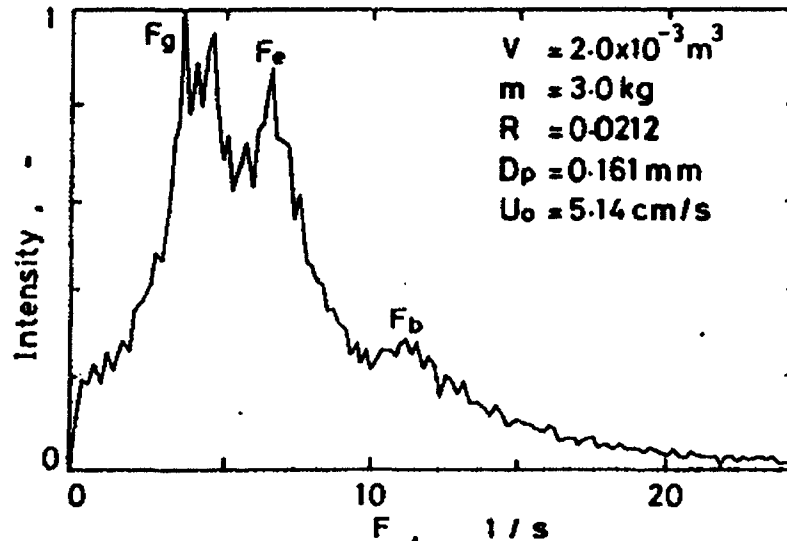


Figure 2.20: An example of multiple-peak phenomena in a power spectrum from a fluidized bed showing frequencies associated with bubble generation (F_g), bubble eruption (F_e), and the natural frequency of the bed (F_b) [19]

Svensson et al. [51] provide evidence of another multiple frequency phenomena: the disappearance of one frequency peak and the emergence of another peak with an increase in fluidization velocity (Figure 2.21). Although this testing was done in a circulating fluidized bed and the increase in fluidization velocity needed to bring about this change was very large compared to fluidization velocities in bubbling fluidized beds, it does show that such an emergence and disappearance of dominant frequency peaks is possible. Figure 2.21 shows that the dominance of peaks is likely to occur gradually, not with “jump-like” shifting as described by Svoboda et al [22].

Association of multiple-peak phenomena to bubble effects

As the cause of pressure fluctuations in fluidized beds have been attributed to many phenomena, Roy et al. [45] have attempted to categorize the types of pressure fluctuations

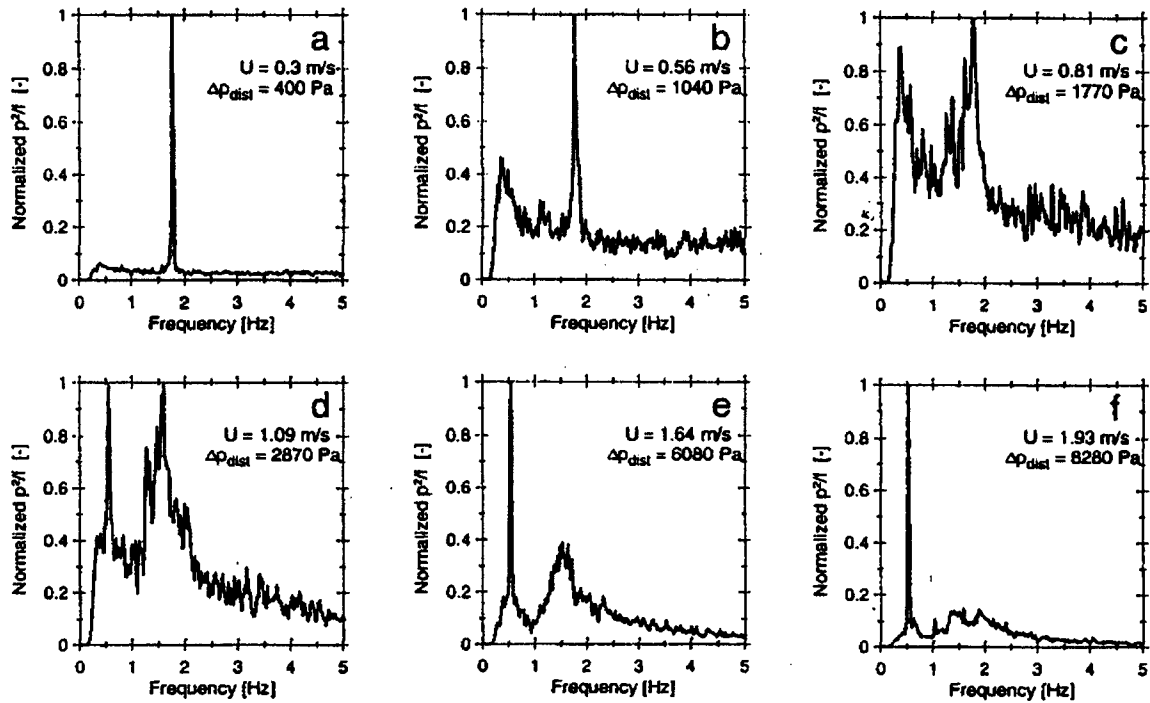


Figure 2.21: An example of multiple-peak phenomena in the power spectrum of a circulating fluidized bed showing the dominance between two peaks (1.75 Hz and 0.5 Hz) changing with an increase in fluidization velocity [51]

and their corresponding bed parameters. Among these categories, bubble effects have been linked to the pressure fluctuations in a bubbling fluidized bed (e.g., [46]). In a review paper on the various techniques used to study fluidization phenomena, Yates and Simons [15] state that the pressure fluctuations “are generally acknowledged to be due to the flow of bubbles, but the exact cause and effect have been the source of much discussion.” They offer that pressure fluctuation phenomena may be the result of bubble eruption at the surface, bubble coalescence, bubble formation, and distributor plate effects.

As bubble effects are related to pressure fluctuation phenomena, the understanding of bubble dynamics is important to understand the corresponding frequencies. Davidson was the first researcher to adequately describe the movement of bubbles in a fluidized bed, and his work is detailed in [52]. This model includes such postulates as the gas bubble being solids-free and spherical, and the medium surrounding the bubble being incompressible.

Davidson also worked with Darton et al. [53] to develop a model that employs bubble coalescence to explain the reason for bubble growth. Figure 2.22 illustrates the bubble path that results from the coalescence and upward movement of the bubbles. The authors state that “bubbles tend to rise in preferred paths” and note that this behavior has been observed by many researchers, with [54] given as an example. The two bubbles on the upper right of this figure also provide an example of how bubbles may coalesce, with the bottom bubble brought up into the top bubble’s wake.

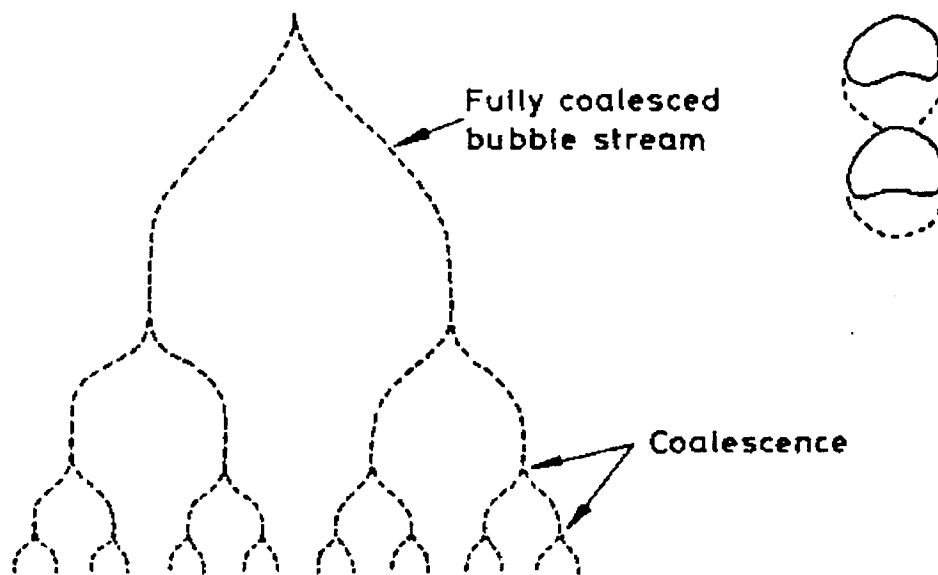


Figure 2.22: Bubble coalescence model from Darton et al. [53] showing the path of coalescence of a bubble stream (left) and an example of two bubbles coalescing vertically (upper right)

Believing that bubble effects are associated with the pressure fluctuations in fluidized beds and the frequency peaks in their power spectrums, Van der Schaaf et al. [55,56] have studied the influence of a single bubble on the pressure in the bed. A single gas pulse was introduced into the plenum of a bed at minimum fluidization. Figure 2.23 shows the pressure characteristics and associated bubble effects (e.g., bubble eruption) of the single bubble divided into three phases: homogenous oscillation of the bed, bubble movement in the bed, and bed surface effects with bubble eruption.

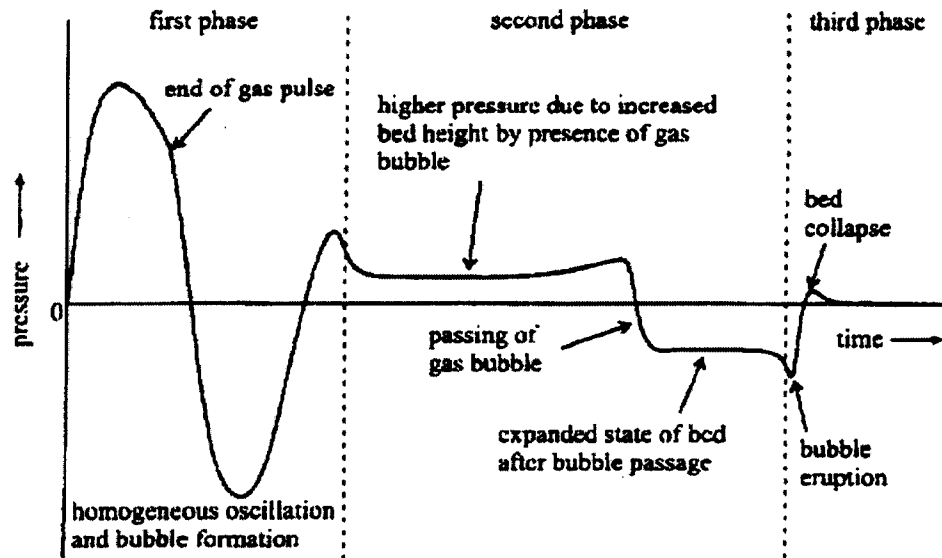


Figure 2.23: Pressure response in the bed from a gas pulse introduced in the plenum [55]

This figure shows that an effect such as bubble eruption causes pressure fluctuations. Bubble coalescence was not discussed in this figure as only a single bubble was formed in the bed when a gas pulse was introduced into the plenum.

Pressure fluctuations and second-order systems

Brue and Brown [1,2,11,12] linked the power spectrums from a fluidized bed to the dynamic behavior of a second-order system. They believed that the bed acted as a second-order system and that phenomena such as bubble eruptions at the surface acted as a forcing function. These researchers adjusted the natural frequency and damping ratio of a second-order frequency-response function (FRF) so that its output aligned with the experimental power spectrum when laid on top in a Bode plot. When more than one peak was present in the experimental spectrum, FRF's were added in parallel to account for each peak. They used the natural frequencies and damping ratios from the FRF as validation parameters for a similitude study. For example, the dimensionless natural frequencies from two scaled

fluidized beds (e.g., a model bed and prototype bed) were compared to determine if similitude was achieved.

CHAPTER 3. DATA ANALYSIS AND MODELING PARAMETERS

The following chapter is divided into four sections. The first section provides a background on a second-order mechanical system and its governing equations of motion, as the pressure fluctuation phenomena are later compared to second-order systems. The second section discusses data analysis techniques used to examine signals with periodic phenomena. In the third section, a method to determine the order of a system is presented along with an example of a second-order frequency-response function with a random input. In the last section, relationships for the natural frequency and damping ratio are derived for a fluidized bed acting as a second-order system and expressed in terms of bed height.

Second-Order Systems

Earlier work has shown that bubbling fluidized beds may be characterized as a second-order system or several second-order systems acting in parallel [1]. A mechanical second-order system consists of a mass connected to the ground through a spring and damper acting in parallel [57]. An example of this system is shown below in Figure 3.1.

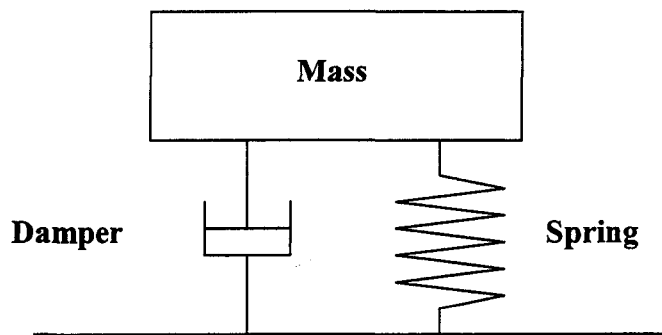


Figure 3.1: A mechanical second-order system

A force balance on the system yields the following equation.

$$m \cdot \frac{d^2 y(t)}{dt^2} + c \cdot \frac{dy(t)}{dt} + k \cdot y(t) = u(t) \quad (3.1)$$

The first term on the left hand side of the equation describes the force due to acceleration of the mass, the second term describes the force associated with the damper, and the third term describes the force associated with the spring. The $u(t)$ term on the right-hand side of the equation is a forcing function that may act on the system but is not present in the diagram. The solution for this equation with no forcing function can be determined by assuming a solution of the form

$$y(t) = C \cdot e^{st} \quad (3.2)$$

This leads to the following characteristic equation

$$m \cdot s^2 + c \cdot s + k = 0 \quad (3.3)$$

which has the solution

$$y(t) = C_1 \cdot e^{s_1 t} + C_2 \cdot e^{s_2 t} \quad (3.4)$$

where

$$s_{1,2} = -\frac{c}{2 \cdot m} \pm \sqrt{\left(\frac{c}{2 \cdot m}\right)^2 - \frac{k}{m}} \quad (3.5)$$

By using the following definitions for the natural frequency and damping ratio, respectively,

$$\omega_n = \sqrt{\frac{k}{m}} \quad (3.6)$$

$$\xi = \frac{c}{2 \cdot \sqrt{k \cdot m}} \quad (3.7)$$

the roots become

$$s_{1,2} = \left(-\xi \pm i \cdot \sqrt{1 - \xi^2} \right) \cdot \omega_n \quad (3.8)$$

The natural frequency and damping ratio definitions can also be substituted into Equation 3.1 to yield

$$\frac{d^2 y(t)}{dt^2} + 2 \cdot \xi \cdot \omega_n \cdot \frac{dy(t)}{dt} + \omega_n^2 \cdot y(t) = u(t) \quad (3.9)$$

For an under-damped system ($\xi < 1$), the solution to the force balance equation can be manipulated to yield

$$y(t) = A \cdot e^{-\xi \omega_n t} \cdot \cos(\omega_d t + B) \quad (3.10)$$

where A and B are arbitrary constants determined from initial conditions and ω_d is the damped natural frequency defined as

$$\omega_d = \omega_n \cdot \sqrt{1 - \xi^2} \quad (3.11)$$

When an under-damped system with a natural frequency of 1 Hz and a damping ratio of 0.1 is excited by an impulse force, the resulting displacement for the system is shown in Figure 3.2.

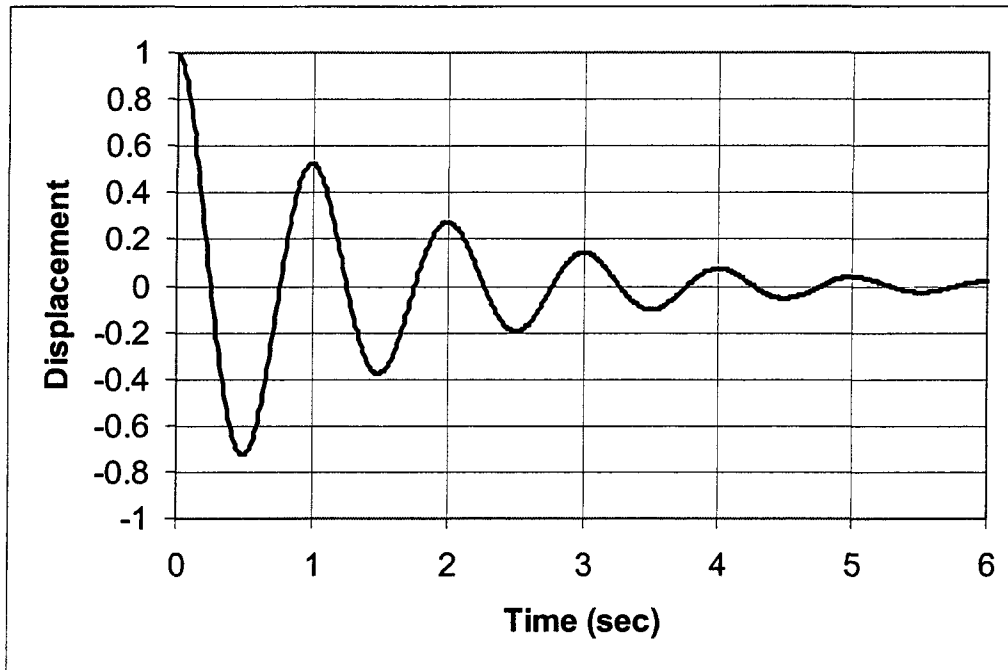


Figure 3.2: Displacement of a second-order system from an impulse

The system oscillates at the damped natural frequency. It is easily shown that for the case of no damping, the results give an infinite sinusoidal wave with the natural frequency as the frequency of oscillation.

Signal Analysis

The following section describes the signal analysis techniques used in this dissertation. This explanation follows Brown and Hwang [58], and similar explanations (e.g., discrete formulations) can be found in [59-61]. This section is separated into statistical, time-domain, and frequency-domain analysis techniques.

Statistical analysis

In the early studies on BFB pressure fluctuations, statistical analysis techniques were used to describe the fluctuations [34]. These techniques include the mean, variance, and

probability density function (PDF) of the pressure fluctuations. The mean may be calculated by integrating the product of the variable and its PDF as shown in the equation below.

$$\mu_y = E[y(t)] = \int_{-\infty}^{\infty} y(t) \cdot p_y(t) \cdot dt \quad (3.12)$$

In this equation, μ_y is the mean, $y(t)$ is the variable as a function of time t , and $p_y(t)$ is the PDF, which describes the relative distribution of the variable. The mean may also be expressed as the expected value of $y(t)$, i.e., $E[y(t)]$. The expected value can be viewed as a type of averaging process for a variable or set of variables. Its use will become significant in explaining processes in the time-domain and frequency-domain sections.

The statistical techniques mentioned above have limited capability in describing pressure fluctuations. Because of this, researchers use the time-domain and frequency-domain techniques discussed below.

Time-domain analysis

It is difficult to determine if a set of data contains a periodic component by observing its time history when a large amount of noise or several frequencies are present in the data. To determine whether the data set has a periodic nature, the set may be processed through a correlation function. The autocorrelation function (ACF) is the integration of the product of the variable and its value at a time ' τ ' later. It can be intuitively understood that this function will be largest (show high correlation) when the two variables being multiplied are similar, while the function will be lowest when the two variables are dissimilar (show low correlation). The ACF ($R_{yy}(\tau)$) for a data set is given below.

$$R_{yy}(\tau) = \lim_{T \rightarrow \infty} \frac{1}{T} \cdot \int_0^T y(t) \cdot y(t + \tau) \cdot dt \quad (3.13)$$

In terms of the expected value notation, the ACF is given as

$$R_{yy}(\tau) = E[y(t) \cdot y(t + \tau)] \quad (3.14)$$

The ACF of a random process will produce a maximum value at zero and decrease rapidly to zero for all other values of ' τ '. In contrast, the ACF of a periodic signal will yield another periodic signal with the same frequency.

The ACF has been used during the early research on fluidized bed pressure fluctuations to show that the pressure fluctuations contain a periodic component [17]. The frequency of the periodic component in the data set can be determined indirectly by using the ACF. This is done by measuring the amount of time between peaks on the ACF to get the period of the data set. The frequency is the inverse of this period.

Similar to the autocorrelation function, the crosscorrelation function (CCF) may be performed on two sets of data to determine the correlation between the two signals. This has been done in the literature to show the correlation between two different sampling sites or to filter out any signals that are common between the two sampling points [17]. For example, measuring the pressure signal between two points relatively close to one another in a fluidized bed will show the local pressure phenomena by canceling out any global phenomena that affect both sampling points at the same time.

Frequency-domain analysis

As stated above, the ACF can be used to indirectly determine the frequency component of a periodic data set. One method to directly determine the frequency or frequencies associated with the system is to process the data set through the power spectral density (PSD) technique. The PSD represents the amount of power in a given frequency interval contained in the data set. This can be done using the Weiner-Khinchin relation [58]. This relation is given in Equation 3.15 and states that the PSD can be calculated by taking the Fourier transform of the ACF, where $\mathfrak{F}[x]$ is the Fourier transform of x .

$$S_{yy}(i\omega) = \mathfrak{F}[R_{yy}(\tau)] = \int_{-\infty}^{\infty} R_{yy}(\tau) \cdot e^{-i\omega\tau} \cdot d\tau \quad (3.15)$$

This definition for the Fourier transform is across an infinite range. This range can be separated into finite sections by splitting the interval into a periodogram

$$\int_{-\infty}^{\infty} R_{yy}(\tau) \cdot e^{-i\omega\tau} \cdot d\tau = \lim_{T \rightarrow \infty} E \left[\frac{1}{T} \cdot |\mathfrak{F}\{y_{\tau}(t)\}|^2 \right] \quad (3.16)$$

where the quantity in brackets on the right hand side of Equation 3.16 above is known as the periodogram.

The Fourier transform of the periodogram for the given interval can be calculated using the Fast Fourier Transform (FFT) algorithm. This yields the following equation for the PSD, where the square of the value of the FFT can be found by multiplying the FFT by its complex conjugate (denoted by a super-scripted asterisk).

$$S_{yy} = E \left[\frac{1}{T} \cdot [FFT \cdot FFT^*] \right] \quad (3.17)$$

In the above relation, the expectation operation indicates that the FFT periodogram is taken over several averages.

System Identification

A system may be characterized by how it reacts (output or response) to a given action (input or excitation) [62]. A linear system can be described by a transfer function using the Laplace transform (or by a frequency-response function in the frequency domain). Figure 3.3 shows the interaction between the input and output response of the system in the time domain and the transfer function in the Laplace domain.

The transfer function, $H(s)$, for this system is defined as the ratio of the output response $Y(s)$ to the input stimulus $X(s)$ as shown in Equation 3.18. This transfer function

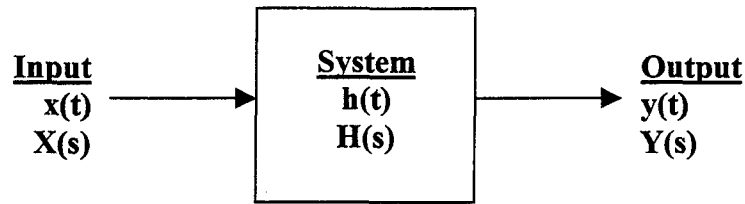


Figure 3.3: Input, output, and system configuration

may be described as a gain performed on the input to produce the given output.

$$H(s) = \frac{Y(s)}{X(s)} \quad (3.18)$$

By looking at the power of the above system, Equation 3.18 can be described in terms of the input PSD, output PSD, and the power of the gain so that the relation can be manipulated to yield

$$S_{yy}(s) = |H(s)|^2 \cdot S_{xx}(s) \quad (3.19)$$

where $|H(s)|$ is the gain. For white noise input, the PSD of the input is the variance of the white noise (a constant). This information can be substituted into the above equation to yield

$$S_{yy}(s) = |H(s)|^2 \cdot \sigma^2 \quad (3.20)$$

One method of representing the transfer function involves the use of a Bode plot. A Bode plot can be created by plotting the logarithm of the transfer function gain against the logarithm of the frequencies tested. To create a Bode plot for the system discussed above,

the logarithm of each side of Equation 3.20 is taken and solved for the transfer function to yield

$$20 \cdot \log|H(s)| = 10 \cdot \log(S_{yy}(s)) - 20 \cdot \log(\sigma) \quad (3.21)$$

The Bode plot offers a method for describing the gain of the second-order system discussed above in terms of the system output. As an example, a Bode plot can be used to see the effect of different damping ratios on the second-order system gains. An example of a second-order system with a natural frequency of 1 Hz and different damping ratios is shown in Figure 3.4. The value on the vertical axis is ten times the log of the power of the signal (or twenty times the log of the amplitude of the signal) and is listed in decibels (dB).

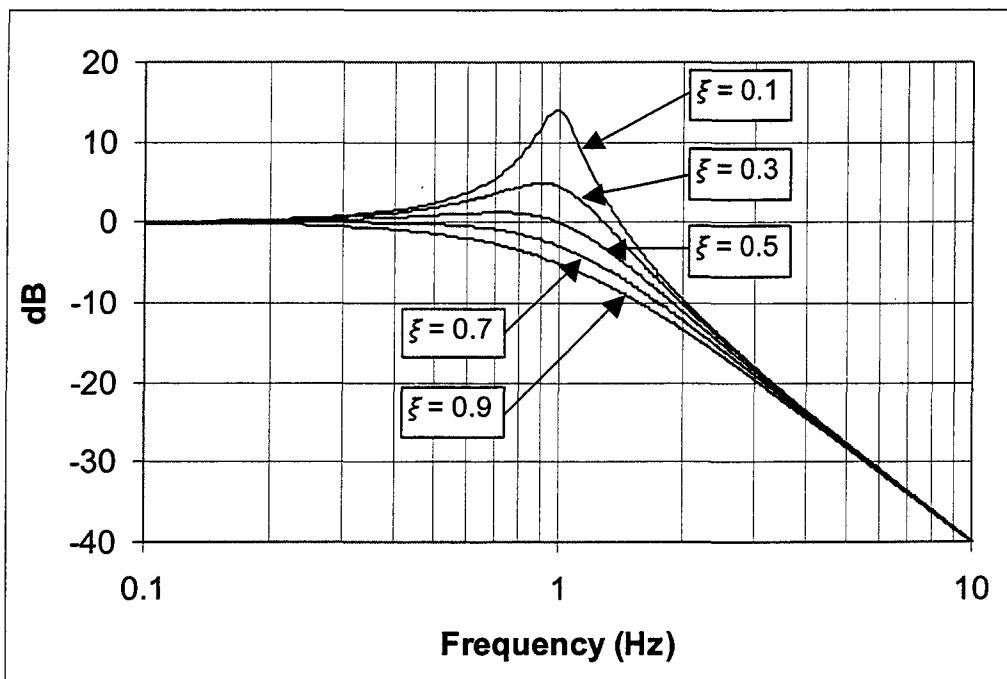


Figure 3.4: Second-order systems with different damping ratios on a Bode plot

As shown in this figure, the response of second-order systems exhibits -40dB/decade slope drop-off, which is indicative of second-order systems [63]. First-order systems exhibit a -20 dB/decade response, while third-order systems exhibit -60 dB/decade response. It is

interesting to note that the peak of the power spectrum shown in the Bode plot is located at the resonance frequency, given below, not the damped natural frequency.

$$\omega_r = \omega_n \cdot \sqrt{1 - 2 \cdot \xi^2} \quad (3.22)$$

To show how the Bode plot may be used for system identification, the second-order transfer function of Equation 3.23 is first examined.

$$H(s) = \left(\frac{1}{1 + \frac{2 \cdot \xi}{\omega_n} \cdot s + \frac{s^2}{\omega_n^2}} \right) \cdot C \quad (3.23)$$

This transfer function can be used with white noise as an input to yield a given output. This is similar to the transfer function acting as a second-order filter for the random data input. Figure 3.5 shows the random input data and the output data after it has been passed through the transfer function. The filtered time data may be examined by discretizing the second-order equation.

By setting $s = i\omega$, the system characteristics can be shown in the frequency domain. A Bode plot of the random data from Figure 3.5 passed through an under-damped, second-order frequency response function is shown in Figure 3.6. As shown in this figure, the frequency-response function is under-damped and shows a peak at 5 Hz. Overlaid on this data is the plot of a second-order, frequency-response function. Both of the plots show the -40dB/decade slope drop-off. A Bode plot of strictly white noise would show a straight line with zero slope.

To examine the filtered times-series data in the frequency domain using the Bode plot, the data from Figure 3.5 were processed with a Mathcad program (discussed in Chapter 4) using the spectral analysis techniques described above. It is important to point out that the obvious correlation on the Bode plot between the random filtered data and the overlaid frequency-response function is due to several issues addressed in the program. First, the

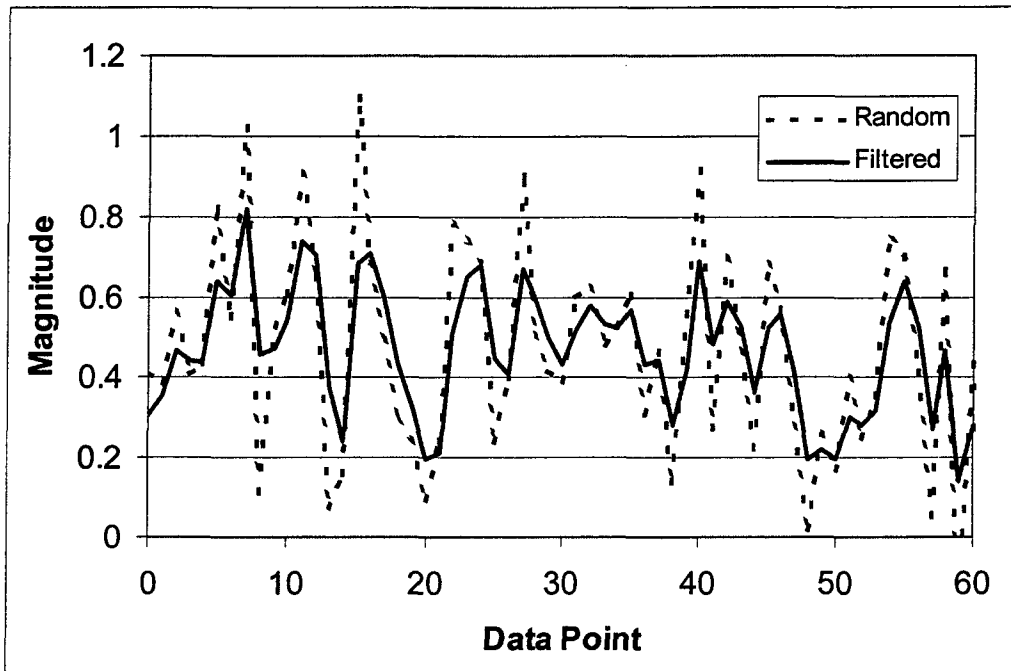


Figure 3.5: Random and filtered data

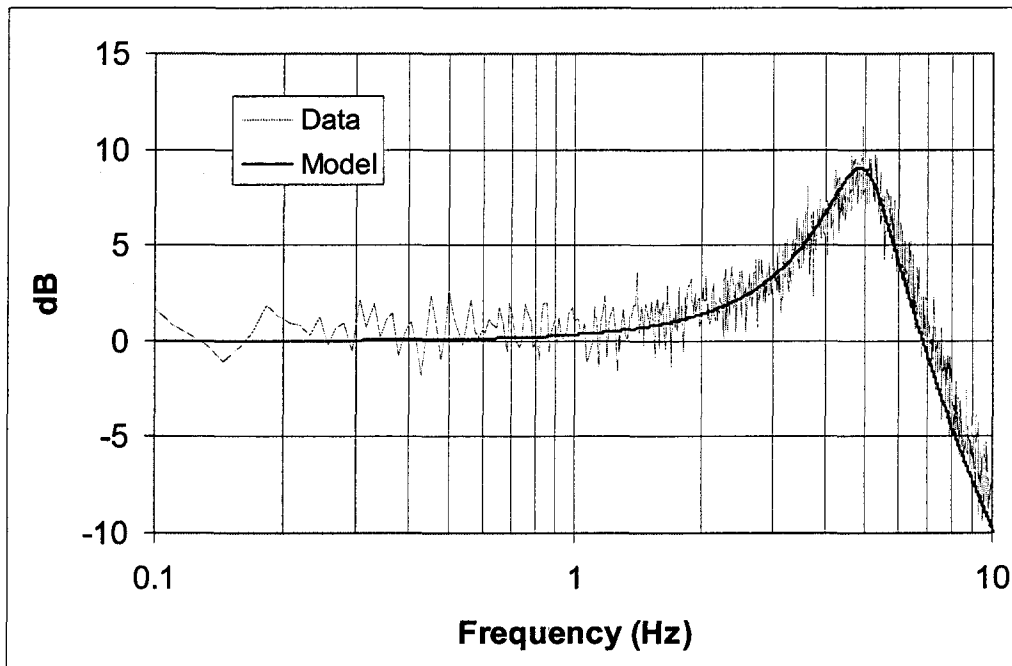


Figure 3.6: Bode plot of second-order filtered data and model

analysis model averaged several sets of data to decrease the influence of the random nature of the data. Second, an appropriate sampling frequency was used to provide a suitable range of the relevant frequencies. Third, a large periodogram (i.e., large sampling times) was used to allow for small intervals between frequency points so that point-to-point resolution was favorable.

The power spectrums of pressure fluctuations from some fluidized bed regimes have the Bode plot characteristics of two or more second-order systems acting in parallel [1,2]. Two systems acting in parallel in the Laplace domain are added together as shown in Equation 3.24.

$$H(s) = \left(\frac{C_1}{1 + \frac{2 \cdot \xi_1}{\omega_{n1}} \cdot s + \frac{s^2}{\omega_{n1}^2}} + \frac{C_2}{1 + \frac{2 \cdot \xi_1}{\omega_{n1}} \cdot s + \frac{s^2}{\omega_{n1}^2}} \right) \quad (3.24)$$

Two modeled second-order systems acting in parallel are shown in Figure 3.7. The systems are overlaid on experimental data that Brue and Brown [2] acquired from a fluidized bed.

Determination of Modeling Parameters

The following chapter is divided into two sections. In the first section, the natural frequency is derived for a fluidized bed. This derivation follows directly from Brue [1] and Hiby [33]. In the second section, the damping ratio that accompanies this natural frequency is derived. The natural frequency and damping ratio for a fluidized bed are derived here to determine how these two quantities are theoretically related to bed height. This relationship will then be compared to the experimental relationship determined in the second-order modeling section presented in Chapter 5.

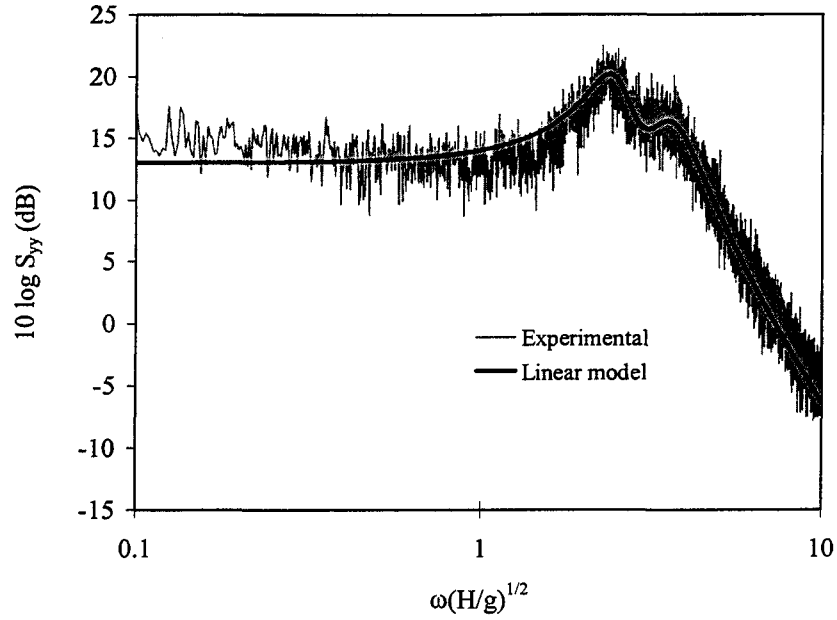


Figure 3.7: Experimental data with output from a multiple-order system [2]

Natural frequency

A force balance similar to Equation 3.1 is written below for a single particle without a forcing function. In this equation, “ h_i ” is the vertical height of an individual particle, and “ C_R ” and “ K_R ” are the damping constant and stiffness constant, respectively.

$$m_i \cdot \frac{d^2 h_i}{dt^2} + C_R \cdot \frac{dh_i}{dt} + K_R \cdot h_i = 0 \quad (3.25)$$

The stiffness constant is defined as the change in force per change in distance.

$$K_R = \frac{dF_i}{dh_i} \quad (3.26)$$

The damping constant is defined as the change in force per change in velocity.

$$C_R = \frac{dF_i}{dv_{\text{int}}} \quad (3.27)$$

$$v_{\text{int}} = \frac{dh_i}{dt} \quad (3.28)$$

The velocity in Equations 3.27 and 3.28 is the interstitial velocity (v_{int}), as this is the velocity acting upon the particle. To determine the stiffness and damping constants, a force balance was performed on a single particle. This balance on the particle shows that the force is equal to the weight of the particle and the pressure force acting on it.

$$F_i = -m_i g + \frac{\Delta p A}{N} \quad (3.29)$$

The number of particles in a fluidized bed can be defined as

$$N = \frac{V_s}{V_p} = \frac{V \cdot (1 - \varepsilon)}{\left(\frac{\pi}{6}\right) \cdot d_p^3} \quad (3.30)$$

Combining Equations 3.29 and 3.30 yields

$$F = -mg + \frac{\pi \cdot \Delta p \cdot A \cdot d_p^3}{6 \cdot V \cdot (1 - \varepsilon)} \quad (3.31)$$

Substituting $A/V = 1/H$, the force balance equation becomes

$$F = -mg + \left(\frac{\pi \cdot d_p^3}{6 \cdot (1 - \varepsilon)}\right) \cdot \left(\frac{\Delta p}{H}\right) \quad (3.32)$$

Under fluidization conditions, the pressure drop can be estimated using the Ergun equation at minimum fluidization velocity (U_{mf}). The Ergun equation at minimum fluidization is

$$\frac{\Delta p}{H} = 150 \cdot \frac{U_{mf} \cdot \mu}{d_p^2} \cdot \frac{(1-\varepsilon)^2}{\varepsilon^3} + 1.75 \cdot \frac{\rho_g \cdot U_{mf}^2}{d_p} \cdot \frac{(1-\varepsilon)}{\varepsilon^3} \quad (3.33)$$

Combining Equations 3.32 and 3.33 yields

$$F = -mg + \left(\frac{\pi \cdot d_p^3}{6} \right) \cdot \left(150 \cdot \frac{U_{mf} \cdot \mu}{d_p^2} \cdot \frac{(1-\varepsilon)}{\varepsilon^3} + 1.75 \cdot \frac{\rho_g \cdot U_{mf}^2}{d_p} \cdot \frac{1}{\varepsilon^3} \right) \quad (3.34)$$

It is assumed that individual particles oscillate such that at every moment all particles show the same relative vertical displacement from their equilibrium position. The amplitude of an individual particle ' i ' is then proportional to its height h_i and,

$$\frac{dh_i}{h_i} = \frac{dH}{H} \quad (3.35)$$

The voidage (ε) is related to the bed height through its definition (the ratio of the volume of gas to the total volume of the bed), and the following relationship is determined

$$\varepsilon = \frac{V - V_s}{V} = 1 - \frac{V_s}{A \cdot H} \quad (3.36)$$

Solving for H,

$$H = \frac{V_s}{A \cdot (1-\varepsilon)} \quad (3.37)$$

Equation 3.35 can be re-arranged to yield

$$\frac{dH}{dh_i} = \frac{H}{h_i} \quad (3.38)$$

Differentiating Equation 3.36 yields

$$\frac{d\varepsilon}{dH} = \frac{V_s}{A \cdot H^2} \quad (3.39)$$

Combining Equations 3.37, 3.38, and 3.39 yields

$$\frac{d\varepsilon}{dh_i} = \frac{d\varepsilon}{dH} \cdot \frac{dH}{dh_i} = \frac{V_s}{A \cdot H \cdot h_i} = \frac{1 - \varepsilon}{h_i} \quad (3.40)$$

Differentiating Equation 3.34

$$\frac{dF_i}{d\varepsilon} = - \left(\frac{\pi \cdot d_p^3}{6} \right) \cdot \left(150 \cdot \frac{U_{mf} \cdot \mu}{d_p^2} \cdot \frac{3 - 2 \cdot \varepsilon}{\varepsilon^4} + 1.75 \cdot \frac{\rho_g \cdot U_{mf}^2}{d_p} \cdot \frac{3}{\varepsilon^4} \right) \quad (3.41)$$

Combining Equations 3.40 and 3.41

$$\frac{dF_i}{dh_i} = K_R = \left(\frac{\pi \cdot d_p^3}{6 \cdot h_i} \right) \cdot \left(150 \cdot \frac{U_{mf} \cdot \mu}{d_p^2} \cdot \frac{(1 - \varepsilon) \cdot (3 - 2 \cdot \varepsilon)}{\varepsilon^4} + 1.75 \cdot \frac{\rho_g \cdot U_{mf}^2}{d_p} \cdot \frac{1 - \varepsilon}{\varepsilon^4} \cdot 3 \right) \quad (3.42)$$

As in a mass-spring system the frequency of oscillation can be predicted by

$$\omega_i = \sqrt{\frac{K_R}{m_i}} = \sqrt{\left(\frac{3}{\rho_s \cdot h_i} \right) \left(150 \cdot \frac{U_{mf} \cdot \mu}{d_p^2} \cdot \frac{(1 - \varepsilon) \cdot (3 - 2 \cdot \varepsilon)}{3 \cdot \varepsilon^4} + 1.75 \cdot \frac{\rho_g \cdot U_{mf}^2}{d_p} \cdot \frac{1 - \varepsilon}{\varepsilon^4} \right)} \quad (3.43)$$

Therefore

$$\omega_i = C_1 \cdot h_i^{-0.5} \quad (3.44)$$

For small changes in the equilibrium voidage ($\varepsilon \approx \varepsilon_{mf}$), C_1 is a constant equal to

$$C_1 = \sqrt{\frac{3}{\rho_s} \left(150 \cdot \frac{U_{mf} \cdot \mu}{d_p^2} \cdot \frac{(1 - \varepsilon_{mf}) \cdot (3 - 2 \cdot \varepsilon_{mf})}{3 \cdot \varepsilon_{mf}^4} + 1.75 \cdot \frac{\rho_g \cdot U_{mf}^2}{d_p} \cdot \frac{1 - \varepsilon_{mf}}{\varepsilon_{mf}^4} \right)} \quad (3.45)$$

This shows that the natural frequency of a particle depends on its height in the bed. The entire bed will tend to oscillate at an overall mean frequency of the particles, as the bed is “pulled into tune” [33]. Hiby estimates this mean frequency by summing up a weighted average based on the amplitude of oscillation of each level of particles.

$$\omega_n = \frac{\int_0^H (C_1 \cdot h^{-0.5}) \cdot h \, dh}{\int_0^H h \, dh} = \frac{4}{3} \cdot C_1 \cdot H^{-0.5} \quad (3.46)$$

therefore,

$$\omega_n \propto H^{-0.5} \quad (3.47)$$

The relationship between the natural frequency and the bed height has been determined and is shown in Equation 3.47. The trend from this equation is that the natural frequency decreases as the bed height increases.

Damping ratio

To determine the damping ratio, the interstitial velocity is related to the superficial velocity through the voidage

$$v_{\text{int}} = \frac{u_{\text{super}}}{\varepsilon} \quad \varepsilon = \frac{u_{\text{super}}}{v_{\text{int}}} \quad (3.48)$$

The damping coefficient must be split up into two partial derivatives, as the force equation is not defined in terms of interstitial velocity

$$C_R = \frac{dF_i}{dv_{\text{int}}} = \frac{dF_i}{d\varepsilon} \cdot \frac{d\varepsilon}{dv_{\text{int}}} \quad (3.49)$$

Taking the derivative of the voidage with respect to the interstitial velocity yields

$$\frac{d\varepsilon}{dv_{\text{int}}} = -\frac{u_{\text{super}}}{v_{\text{int}}^2} = -\frac{\varepsilon^2}{u_{\text{super}}} \quad (3.50)$$

Multiplying the two partial derivatives together

$$\frac{dF_i}{dv_{\text{int}}} = \frac{\varepsilon^2}{u_{\text{super}}} \left(\frac{\pi \cdot d_p^3}{6} \right) \cdot \left(150 \cdot \frac{U_{mf} \cdot \mu}{d_p^2} \cdot \frac{3-2 \cdot \varepsilon}{\varepsilon^4} + 1.75 \cdot \frac{\rho_g \cdot U_{mf}^2}{d_p} \cdot \frac{3}{\varepsilon^4} \right) \quad (3.51)$$

For the bed conditions considered in this research, the bed was operated at or slightly above minimum fluidization. We can then assume the superficial velocity is essentially the minimum fluidization velocity

$$u_{\text{super}} \approx U_{mf} \quad (3.52)$$

Using the definition of damping ratio and canceling out the volume term

$$\xi_i = \frac{C_R}{2 \cdot m \cdot \omega_i} = \frac{\left(\frac{\varepsilon^2}{U_{mf}} \right) \cdot \left(150 \cdot \frac{U_{mf} \cdot \mu}{d_p^2} \cdot \frac{(3-2 \cdot \varepsilon)}{\varepsilon^4} + 1.75 \cdot \frac{\rho_g \cdot U_{mf}^2}{d_p} \cdot \frac{3}{\varepsilon^4} \right)}{2 \cdot \rho_s \cdot \sqrt{\left(\frac{(1-\varepsilon)}{\rho_s \cdot h_i} \right) \left(150 \cdot \frac{U_{mf} \cdot \mu}{d_p^2} \cdot \frac{(3-2 \cdot \varepsilon)}{\varepsilon^4} + 1.75 \cdot \frac{\rho_g \cdot U_{mf}^2}{d_p} \cdot \frac{3}{\varepsilon^4} \right)}} \quad (3.53)$$

Combining terms

$$\xi_i = \left(\frac{\varepsilon^2}{2 \cdot U_{mf} \cdot \rho_s} \right) \cdot \sqrt{\left(\frac{3 \cdot \rho_s \cdot h_i}{(1-\varepsilon)} \right) \left(150 \cdot \frac{U_{mf} \cdot \mu}{d_p^2} \cdot \frac{3-2 \cdot \varepsilon}{3 \cdot \varepsilon^4} + 1.75 \cdot \frac{\rho_g \cdot U_{mf}^2}{d_p} \cdot \frac{1}{\varepsilon^4} \right)} \quad (3.54)$$

This further reduces down to

$$\xi_i = \left(\frac{1}{2} \cdot h_i^{0.5} \right) \sqrt{\left(\frac{3}{\rho_s \cdot (1-\varepsilon)} \right) \left(150 \cdot \frac{\mu}{3 \cdot U_{mf} \cdot d_p^2} \cdot (3-2 \cdot \varepsilon) + 1.75 \cdot \frac{\rho_g}{d_p} \right)} \quad (3.55)$$

Therefore

$$\xi_i = C_2 \cdot h_i^{0.5} \quad (3.56)$$

For small changes in the equilibrium voidage ($\varepsilon \approx \varepsilon_{mf}$), C_2 is a constant equal to

$$C_2 = \left(\frac{1}{2} \right) \sqrt{\left(\frac{3}{\rho_s \cdot (1-\varepsilon)} \right) \left(150 \cdot \frac{\mu}{3 \cdot U_{mf} \cdot d_p^2} \cdot (3-2 \cdot \varepsilon) + 1.75 \cdot \frac{\rho_g}{d_p} \right)} \quad (3.57)$$

Similar to the process for the natural frequency of a particle being summed across the height (Equation 3.46), the individual damping ratio to determine the weighted-average damping ratio must be determined

$$\xi = \frac{\int_0^H (C_2 \cdot h^{0.5}) \cdot h \, dh}{\int_0^H h \, dh} = \frac{4}{5} \cdot C_2 \cdot H^{0.5} \quad (3.58)$$

therefore,

$$\xi \propto H^{0.5} \quad (3.59)$$

The relationship between the damping ratio and the bed height has been determined and is shown in Equation 3.59. The trend from this equation is that the damping ratio increases as the bed height increases.

Multiple-particle systems

It should be noted that by deriving the natural frequency and damping ratio from a single particle, the dynamic system (i.e., the fluidized bed) was forced to have only one set of eigenvalues (the natural frequency and damping ratio). By coupling 'n' particles together in the derivation, the system may contain up to 'n' sets of different eigenvalues. These additional eigenvalues may be related to the multiple-peak phenomena present in the system's power spectrum. In this research, the fluidized bed was modeled as a dynamic system that had only one set of eigenvalues, and any additional peaks present in the system's power spectrum were considered to be a result of multiple forcing functions acting on the system.

CHAPTER 4. EXPERIMENTAL APPARATUS AND PROCEDURE

The following chapter is divided into two main sections. The first section describes the experimental apparatus used in the testing for this dissertation. The second section discusses the experimental procedure used to gather data for this dissertation, along with the analysis techniques used to evaluate the data.

Experimental Apparatus

The fluidized bed reactor used in this work was part of a pyrolysis system located at the BECON Research Facility in Nevada, IA. The pyrolysis system was used to break down the chemical bonds of biomass such as corn or switch grass and to convert the new constituents into higher-valued products. This conversion occurred at temperatures from 400-550° C in the absence of oxygen. An illustration of this system is given in Figure 4.1.

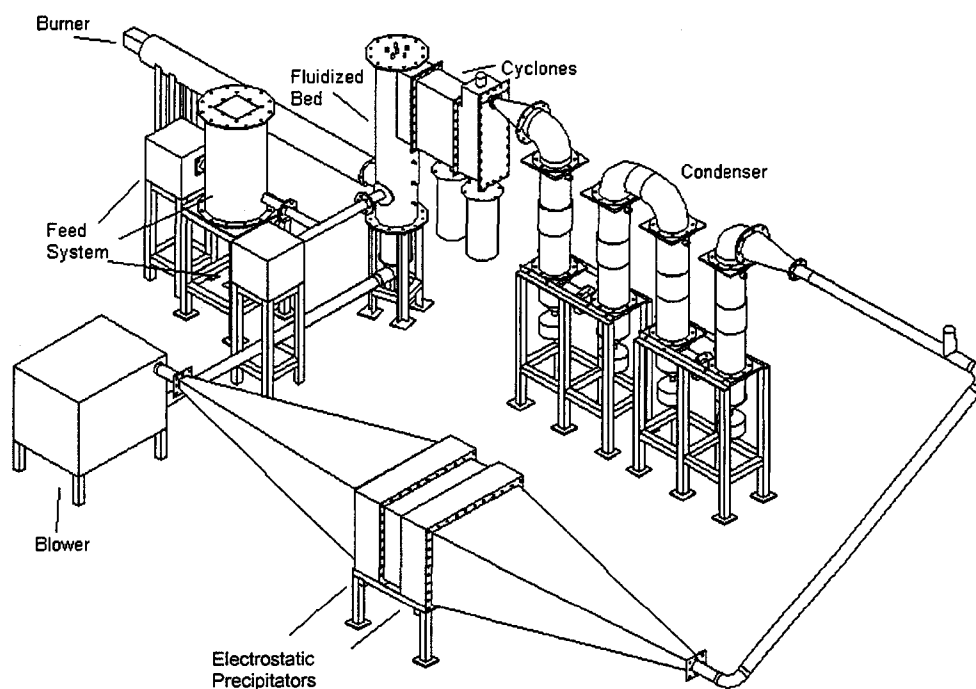


Figure 4.1: Illustration of pyrolysis reactor system

The fluidized bed reactor was constructed of stainless steel and had a diameter of 16.2 cm and a height of 100 cm. This steel bed was well-grounded, which negated any electrostatic effects that may be present in beds constructed of electrically-insulated materials (e.g., Plexiglas). The fluidizing gas entered the plenum and traveled to the bed through a high-restriction distributor plate. This distributor plate had 66 holes with a diameter of 0.28 cm drilled in a square pattern, resulting in a 2% open-area. The fluidizing gas passed through the sand and continued up the freeboard. When pressure fluctuations were measured at ambient temperature, the fluidizing gas was exhausted from the freeboard to the atmosphere. When pressure fluctuations were measured at above ambient temperatures, the fluidizing gas exited the bed to two cyclones through a 1.3 cm by 3.2 cm rectangular section located 77.2 cm above the distributor plate and then to the atmosphere. A natural gas burner provided energy to the bed via a heating jacket annulus around the bed. House air was used as the fluidizing gas for this pressure fluctuation testing.

An example of bed pressure characteristics at fixed and fluidized states is shown Figure 4.2. This test shows that the bed, sand (355-600 micron diameter), and distributor plate performed similarly to fluidized beds in the literature. As shown in this figure, minimum fluidization occurred at a volumetric flow rate of about 220 LPM (liters per minute), which corresponded to a minimum fluidization velocity of 18.2 cm/s for the given conditions. Throughout this dissertation, the flow parameter is stated in terms of volumetric flow through the bed, and the superficial velocity can be determined by dividing this volumetric flow by the cross-sectional area of the bed. Although the graphing technique shown in Figure 4.2 may be used to determine the minimum fluidization velocity (the peak of the pressure differential) for a given bed media, a different procedure was used and explained in the next section.

The probe arms in this study were stainless steel tubes with an inner diameter of 0.46 cm and an outer diameter of 0.64 cm. The tubes were inserted vertically from the top of the bed and held in place with a compression fitting. When pressure fluctuations were measured at ambient temperature, the compression fittings were fastened to a bracket bolted across the top of the bed. The use of this bracket allowed viewing of the bed surface during testing. When the pressure fluctuations were measured above ambient temperature, the compression

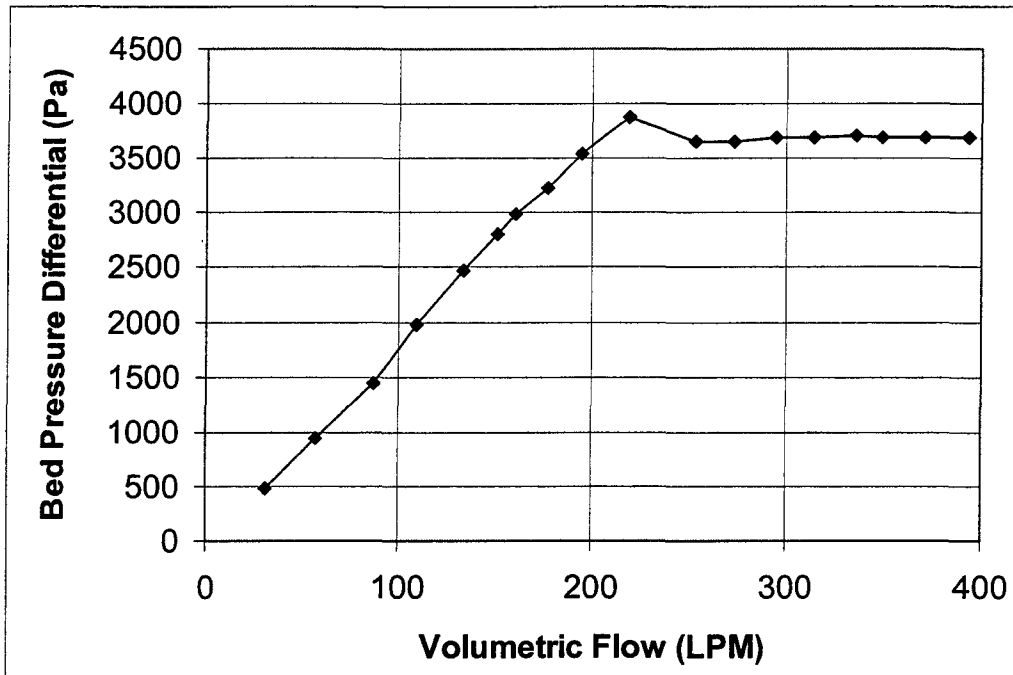


Figure 4.2: Bed pressure effects in a packed and fluidized bed with 355-600 micron diameter sand

fittings were fastened to the bed cover plate. To assure that no effects brought on by arm vibration were present, tests with the arm held solidly in place with another bracket just above the bed surface were performed. These tests were compared to those with an unbracketed arm, and no differences were present between the power spectrums. A wire mesh with 41% open area and a 65 micron open width covered the probe arm openings to prevent bed particles from entering. Testing with different probe meshes showed no differences in the power spectrums. The top end of the probe was attached to the pressure transducer through a short (less than 2 cm) section of plastic tubing. For the tests in this dissertation, the probe lengths varied from 80 cm to 120 cm. Several different probe lengths and diameters were examined in this and other studies [1,11], and no effect of probe diameter or length was found in the power spectrums for the given ranges. Figure 4.3 shows the resulting power spectrums when the probe length was varied from 61 cm to 183 cm, which illustrates that no differences existed in the power spectrums with the different lengths. Calculations of the response time of the probes using equations from Xie and Geldart [64]

showed that the probes were able to measure pressure signals over 500 Hz without attenuation.

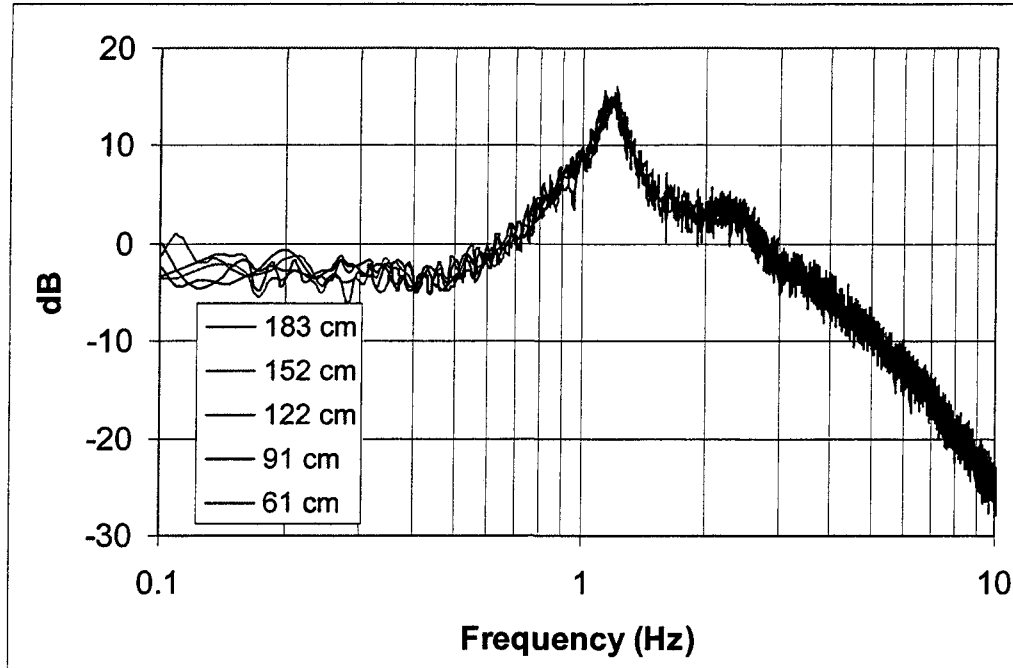


Figure 4.3: Power spectrums for five different probe lengths with 355-600 micron diameter sand and bed height of 60 cm

An Omega PX-140 series and three PX-160 series differential pressure transducers were used to acquire pressure data. The PX-142 pressure transducer (PX142-001D5V) required an 8 VDC (8 mA) input and had a 1 to 6 volt output corresponding to a differential pressure of 0 to 6900 Pa. The three PX-160 series pressure transducers (PX163-2.5BD5V, PX163-005BD5V, and PX164-005D5V) had the same input and output voltages, but the output voltage corresponded to +/-622 Pa, +/- 1244 Pa, and 0-1244 Pa, respectively. The data acquisition board had a 12-bit resolution, and the channel was set to acquire over a range of 0 to 10 volts. This translated to a voltage resolution of 0.00244V, and the corresponding pressure resolution was 3.37 Pa for the PX-142 pressure transducer and much lower for the PX-160 series pressure transducers. To further increase the resolution of the transducer voltage measurement, the software gain was set to 2 or 5 on occasion. For the PX-140 pressure transducer, the linearity, hysteresis, and repeatability errors were 0.75%, 0.3%, and

0.25% of full scale, respectively. These three errors combined were 1.3%, which related to a 90 Pa error for the PX-140 pressure transducer. For the PX-160 series pressure transducers, the linearity error was 1.0% and the combined hysteresis and repeatability error was 0.25%, which related to errors of 15.6 Pa, 31.1 Pa, and 15.6 Pa for the +/-622 Pa, +/- 1244 Pa, and 0-1244 Pa pressure transducers. As errors due to repeatability do not carry through to the frequency domain (any DC component or voltage offset is irrelevant), pressure transducer error was actually smaller than this when results were compared in the frequency domain. All pressure transducers had a response time of one millisecond. Assuming first-order sensor behavior, this related to a cutoff frequency of 160 Hz, more than fast enough to capture the frequency phenomena of the pressure fluctuations, which was below 50 Hz.

The pressure transducer signal was recorded using National Instrument's hardware and software. The pressure transducer was connected to the SCXI-1100 Signal Conditioning Board through a SCXI-1303 Terminal Block. This signal conditioning board was inserted into an SCXI-1000 4-Slot Signal Conditioning Chassis that connected to a 6024E Data Acquisition (DAC) card. This DAC card was connected to the PCI slot of a 500 MHz Dell computer. This computer had 128 MB of RAM and a 4.3 GB hard drive. The National Instruments' LabVIEW software was used to acquire the data and to record the data to a file. Temperatures were measured with a Fluke Digital Thermometer (Model 52-2) during high-temperature testing, and the temperature values were recorded by hand.

Volumetric flow rates were usually measured with an Alicat Scientific Mass Gas Flow Controller Sensor (MC-500SLPM-D/CM). This sensor had a range up to 500 LPM. The accuracy of the sensor was +/-1% full scale (+/-5 LPM), and the sensor had a repeatability of +/-0.5% full scale (+/-2.5 LPM). Dozens of tests in the supply line and in the bed showed that the controller did not influence or introduce any frequency phenomena inside the bed. When a higher-capacity meter was needed (e.g., with large-diameter particle tests), an Omega rotameter (FL4613) was used that measured flow rates up to 566 LPM. This Omega rotameter had an accuracy and repeatability of 2% and 0.5% of full scale, respectively. When a lower-capacity meter was needed (e.g., with plastic particle tests), a Key Instruments rotameter (FR4000A36BL) was used that measured flow rates up to 94 LPM with an accuracy of +/-3% of full scale. Volumetric flow data were recorded by hand.

Table 4.1 lists the bed media used in this research, along with the mean particle diameter and the particle density. The Badger 30x50 sand was predominantly used throughout this testing. Sieve analysis for the two Badger sands is given in Appendix A. The tolerances on the large glass beads, steel shot, and plastic spheres were +/-125 micron, +/-35 micron, and +/-50 micron, respectively.

Table 4.1: Bed media with corresponding particle mean diameter and density

Bed media	Mean diameter (micron)	Density (kg/m ³)
Badger 16x30 sand	878	2650
Badger 30x50 sand	494	2650
Large glass beads	1125	2650
Steel shot	390	7650
Plastic spheres	200	630

Experimental Procedure

For a single test, the bed was operated at steady-state with the set test conditions. About 123,000 data points were acquired at a sampling frequency of 100 Hz. In previous testing [1,11], frequencies as high as 10 Hz were discovered in the bed. This limits the minimum sampling frequency to 20 Hz through the Nyquist sampling frequency theorem [58]. Too high a sampling frequency for the given number of data points makes it difficult to observe low frequency phenomena with the corresponding lower resolution at the lower frequency range. Brue recommended a sampling frequency of 40 Hz to show very low frequency phenomena in the bubbling to turbulent transition regime. As this regime was not examined in this study, a sampling frequency of 100 Hz was chosen for this study. This higher sampling frequency allowed for the detection of higher frequencies that were not measured in Brue's work. Figure 4.4 shows the power spectrums for the pressure fluctuations sampled at 40 Hz and 100 Hz at the same operating conditions, and illustrates that no large differences existed between the two techniques. (The small offset between the two power spectrums is the result of the differences in sampling rates; furthermore, the two

power spectrums lay on top of each other when the power spectral density was plotted for each test.) As the decay slope was used to compare beds with different operating conditions, this sampling frequency also allowed for slope comparisons between the different conditions. To assure that aliasing effects were not present in the frequency domain, several sets of data were post-processed through anti-aliasing, low-pass filters at various frequencies. Filtered and non-filtered data were examined, and the data showed that no aliasing effects were present.

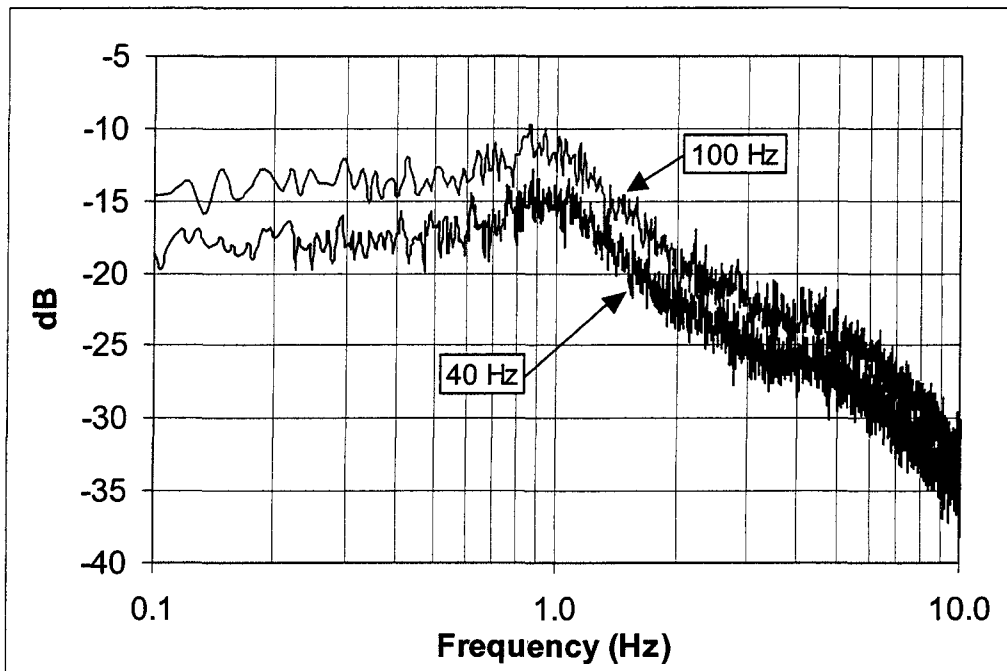


Figure 4.4: Power spectrums for 40 Hz and 100 Hz sampling rates with 355-600 micron diameter sand

The Mathcad software program used to analyze the pressure data is given in Appendix B. The data points were divided into 29 different sections, with each section containing 8192 data points. The program calculated the FFT of each section, and used the FFT to calculate the power spectrum of each section. All 29 power spectrums were averaged, and the log of this average spectrum was taken for graphing on the Bode plot. After the calculation for the log of the power spectrum was done in the Mathcad program, this quantity was copied into MS Excel and graphed. No distinction was made between the

power spectral density and the power spectrum in the Mathcad program or the data presented in this dissertation as the sampling frequency was the same for all data sets and therefore the two quantities differed only by a constant in the Bode plot. Furthermore, reporting the power spectrum as the power spectral density occurs often in the literature.

The combination of sampling frequency, number of total data points, number of data points per section, and averaging produced Bode plots which were meaningful and extremely reproducible. Figure 4.5 shows the power spectrums for three different tests with the same operating conditions on a Bode plot. This figure illustrates the excellent repeatability from test to test, as was observed throughout the entire testing for this dissertation.

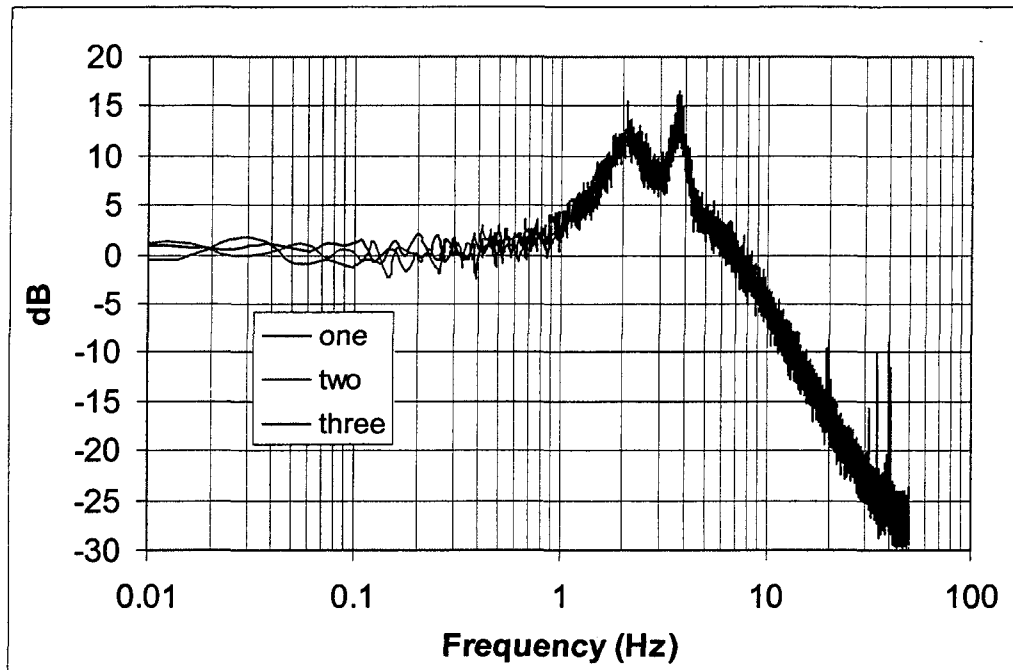


Figure 4.5: Reproducibility for three tests at identical conditions with 355-600 micron diameter sand

Four different probe techniques were examined in this study and are illustrated in Figure 4.6. They were the absolute-static, absolute-dynamic, differential-static, and differential-dynamic probe techniques.

For the absolute probe technique, both probe arms were located in the bed. The first arm was connected to the first port of the pressure transducer to measure the pressure

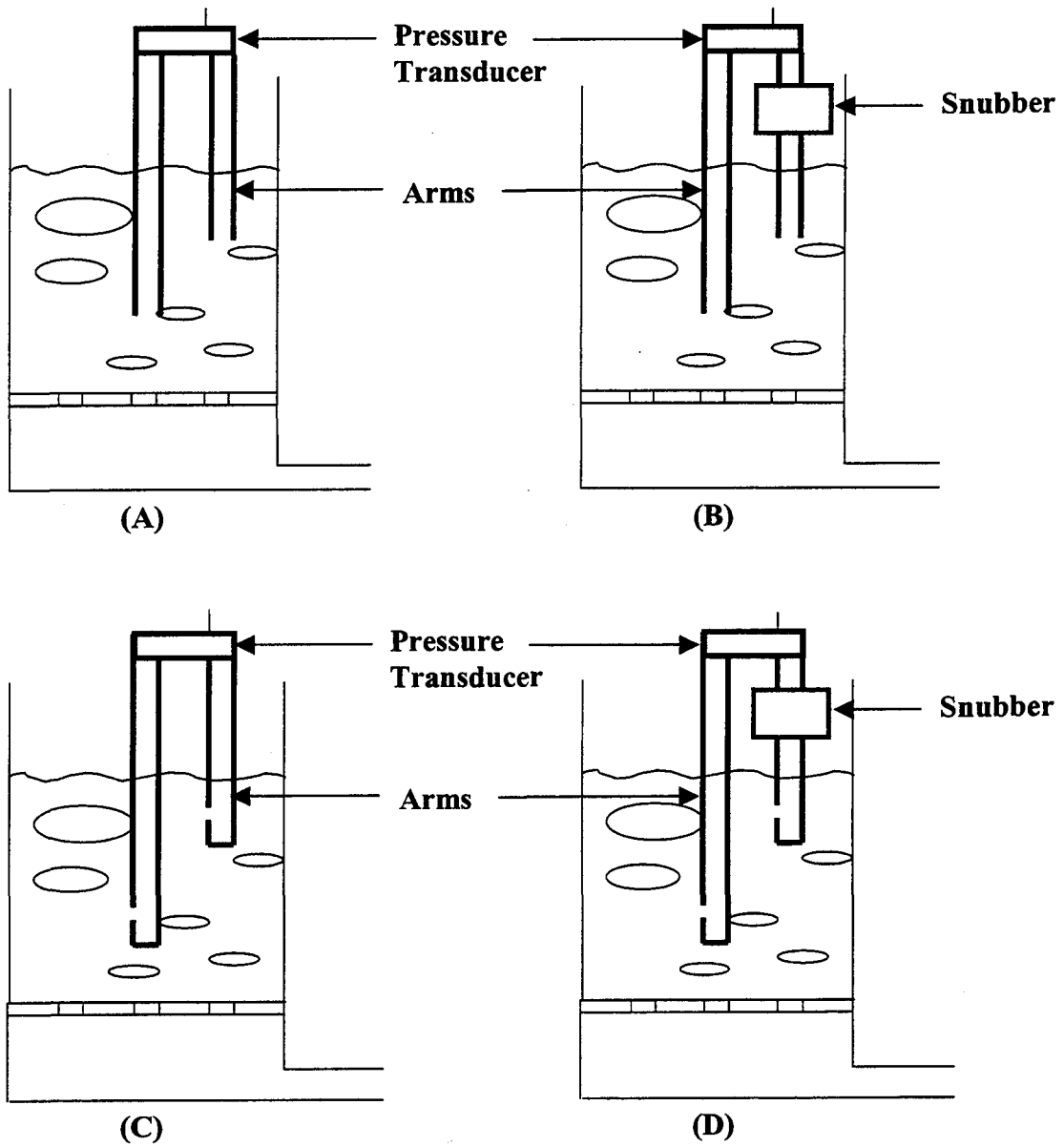


Figure 4.6: Four probe configurations: dynamic-differential (A), dynamic-absolute (B), static-differential (C), and static-absolute (D)

fluctuations at this point. The second arm was connected to the input side of a Ray Solid Body pressure snubber (Model 023B). The output side of the pressure snubber was connected to the second port of the pressure transducer. The horizontal (radial) distance between the two probe arms was 5.08 cm, and the vertical (axial) distance between the two arms was 2.54 cm unless otherwise stated. The pressure snubber filtered out any pressure fluctuations and provided a constant pressure signal to the pressure transducer, which decreased the average pressure of the measured signal by the corresponding pressure at the second arm. This allowed for a more accurate pressure measurement through the use of a narrower-range pressure transducer that more fully encompassed the pressure fluctuations instead of a wider-range transducer that accounted for the higher average pressure and the pressure fluctuations. Figure 4.7 provides an example of how the snubber was used to increase the accuracy of the pressure measurement. By using the constant pressure signal from the snubber, a pressure gauge with a lower range can be used to measure the fluctuations by having the snubber provide a pressure to the second probe port that is near the average of the pressure signal. For the example shown in Figure 4.7, a pressure signal of 900 +/- 40 Pa may be measured with either a 0-1000 Pa pressure gauge or a 0-200 Pa pressure gauge with a snubber providing a pressure signal to the transducer that is near the average of the pressure signal. By using the lower-range pressure transducer, the accuracy of the pressure measurement is increased by a factor of five (assuming that both gauges have the same full-scale accuracy). Over twenty tests were performed that showed that the pressure signal through the pressure snubber was nearly constant (at a threshold nearing the resolution of the data acquisition system), that the frequency peaks in the power spectrum were about 1000 times lower in magnitude than the original signal, and that no differences existed between absolute pressure measurements with and without the snubber in the frequency domain.

The differential probe technique had both inputs of the pressure transducer connected to two arms located in the bed. The horizontal (radial) distance between the two probe arms was 5.08 cm, and the vertical (axial) distance between the two arms was 2.54 cm unless otherwise stated. For the static probe technique, a 0.46 cm diameter hole was located 2.54 cm up from the bottom of the arm on the side to negate edge effects. The dynamic probe

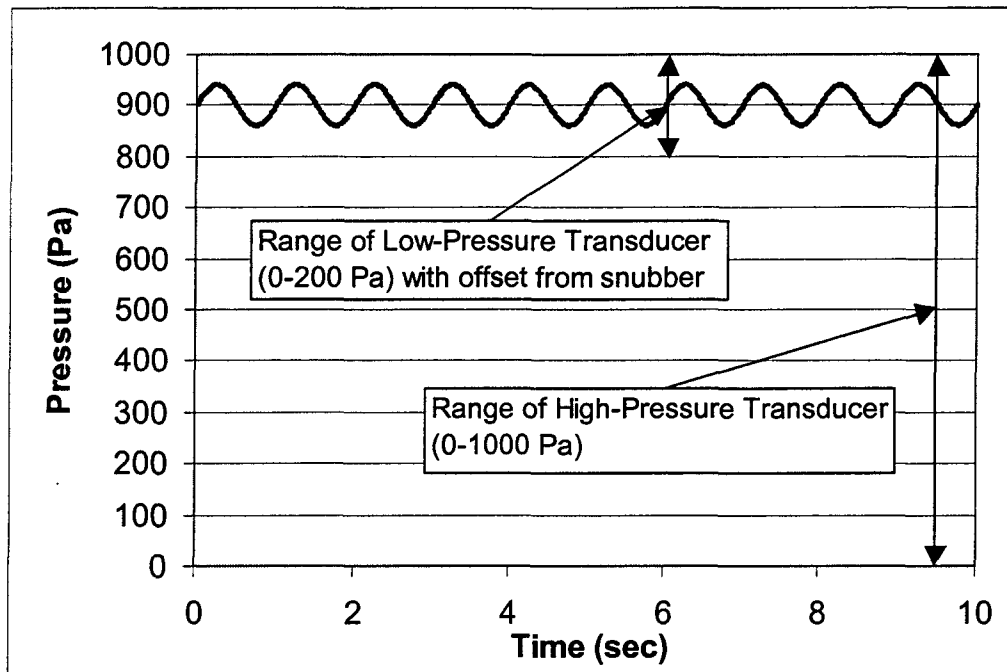


Figure 4.7: An example of increasing the accuracy of the pressure measurement through the use of a pressure snubber with the absolute pressure probe technique

technique had an opening at the end of the arm that was perpendicular to the flow through the bed. The probe arm openings parallel (static) and perpendicular (dynamic) to the flow allowed for any directional pressure effects to be detected. An example of pressure fluctuations in the time domain measured with the dynamic-absolute pressure probe technique is shown in Figure 4.8.

To determine the minimum fluidization velocity, a technique created by Fan et al. [65] was used instead of the graphical method described previously. This technique involved slowly increasing gas flow to the bed until small pressure fluctuations were seen in the pressure signal. This is the point of minimum fluidization, and the presence of pressure fluctuations at this point were very apparent as compared to the constant pressure in a packed bed. Figure 4.9 shows the pressure fluctuations come about with an increase in gas velocity. The abscissa shows the bed pressure, and the ordinate shows the time scale.

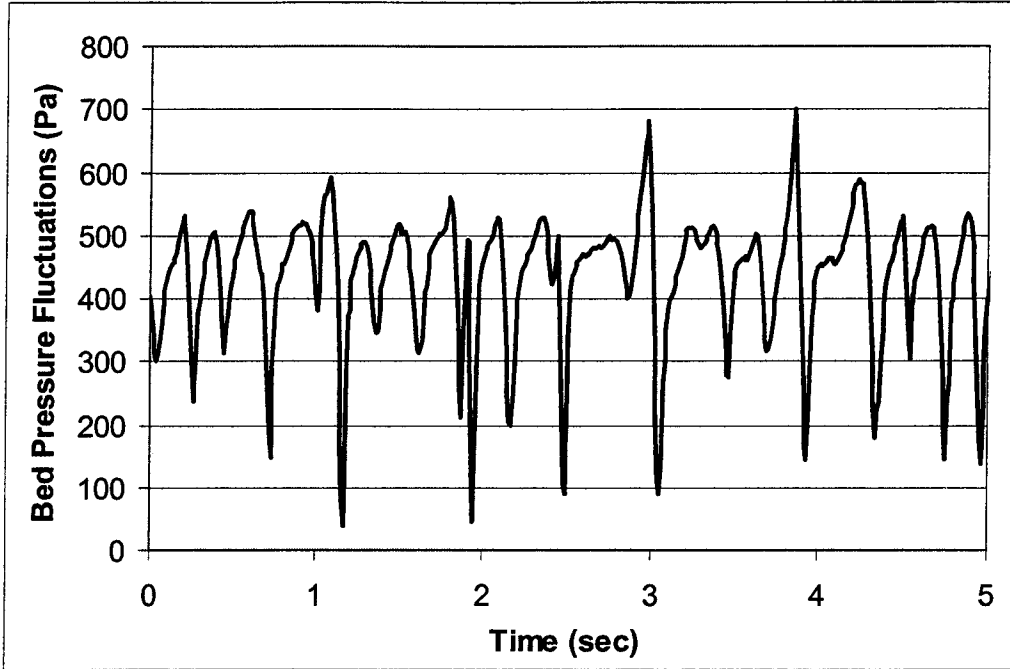


Figure 4.8: Pressure fluctuations with a dynamic-absolute pressure probe

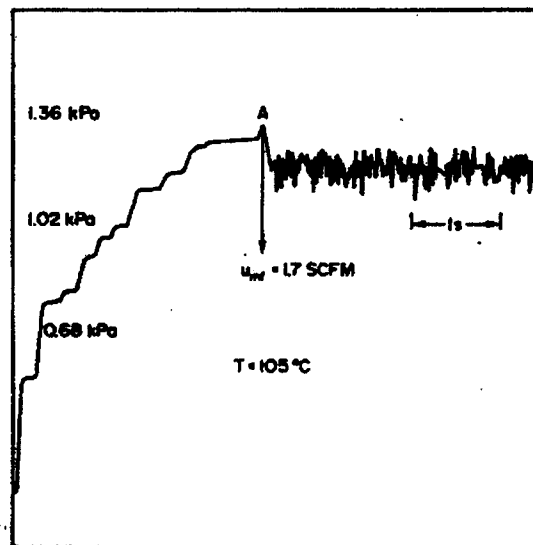


Figure 4.9: A plot of bed pressure (abscissa) against time (ordinate) showing Fan et al.'s technique for determining minimum fluidization [65]

Because bed height was somewhat difficult to measure accurately when the bed was fluidized (measurements within ± 0.3 cm), the mass of the bed media (e.g., sand) was measured with a Setra Model 1000 scale (range from 0-1400 grams, ± 0.01 gram readability). This was done so that nearly identical bed conditions (e.g. bed heights) could be achieved between tests that were not performed consecutively on the same day. The use of equal bed masses between tests at the same bed heights that were to be compared provided high reproducibility between tests.

CHAPTER 5. RESULTS AND DISCUSSION

Chapter 5 is divided into four main sections. The first section discusses the four pressure probe techniques used in this research along with each technique's corresponding power spectrums. It also includes a discussion on the importance of probe arm position in acquiring pressure fluctuation data. Power spectrums with different operating conditions and bed parameters are discussed in the second section. In the third section, the different multiple-peak phenomena that were observed in the bed are addressed and related to bubble effects. The last section involves the modeling of power spectrums with a second-order system. It discusses how the testing and bed parameters related to the pressure fluctuation model, how the model was formulated, and how the model compared to the theoretical and experimental results.

Probe Technique and Position

As described in Chapter 2, researchers have used several different probe techniques to measure the pressure fluctuations in fluidized beds. Among these, the following probe techniques were tested: dynamic-absolute, dynamic-differential, static-absolute, and static-differential. This section is divided into three parts: evaluation of the absolute and differential pressure probe techniques, evaluation of the static and dynamic pressure probe techniques, and the effect of the probe's arm position in the bed on the acquired power spectrums. To determine how the four techniques differed from each other, variables such as bed height and fluidization velocity were varied. The intent of this section is not to determine the exact bed height or fluidization velocity for which the four techniques provide similar or different power spectrums, but rather to show the variation that can occur between the four techniques under certain operating conditions. This knowledge will be used to choose a probe technique for acquiring the pressure fluctuation data for the second-order model.

Absolute and differential probe techniques

Differential probe spacing

As explained in the previous chapter, the absolute technique measures the pressure at a single position in the bed, whereas the differential technique measures the pressure difference between two vertical positions in the bed. To understand the influence of vertical spacing between the two arms of the differential technique, tests were performed at five different differential arm spacings. Figure 5.1 shows power spectrums for a dynamic-absolute probe technique and several dynamic-differential techniques with different spacings between the arms. The power spectrums are offset by 12 dB to clarify the differences between the spectrums. The lowest arm for each probe technique is held constant at 5.1 cm above the distributor plate of a 32.4 cm bed. (The height listed with the “Pressure probe position” entry in the table of Figure 5.1 and other tables to follow is the distance from the lowest probe arm to the distributor plate.) Each differential power spectrum is labeled with the distance between the lowest and highest probe arm in the differential technique in the figure. For example, the bottom power spectrum in this figure had a 1.3 cm vertical spacing between the two probe arms, while the spectrum second from the bottom in the figure has the upper arm raised slightly higher in the bed so that a difference of 2.5 cm existed vertically between the two probe arms. The dynamic-absolute measurement was taken at the low arm position (5.1 cm from the distributor).

As illustrated in Figure 5.1, the spacing between the two arms of the differential technique had a strong influence on the power spectrum. Sitnai et al. [27] generally state that the arm spacing for the differential probe was important in capturing local phenomena, but do not provide any data to support this claim. Clark et al. [35] also mention that they have done testing at three different differential spacings (1.27 cm, 1.9 cm, and 2.54 cm), but do not provide any data or discussion of their results. The effects from the second arm (at a higher position in the bed) in the differential technique yielded a drastically different power spectrum at small arm spacings (e.g., 1.3 cm spacing) than the absolute probe, but the two techniques provided similar power spectrums at large spacings (e.g., 24.1 cm spacing). According to Roy et al. [45], the second arm acts as a filter to the first arm, as any common pressure signal present at both arms are subtracted with the differential technique. The reason that the absolute and differential techniques become similar at large arm spacings

Experimental Operating Conditions for Figure 5.1

Bed media	Badger 30x50 Sand	Bed height	32.4 ± 0.3 cm
Mean particle diameter	494 micron	Bed mass	10554.82 ± 0.01 gm
Particle density	2600 ± 100 kg/m ³	Pressure measurement	Dyn-abs, dyn-dif
Volumetric flow	290 ± 7.5 LPM	Pressure probe position	5.1 ± 0.2 cm
Velocity ratio	1.2	File group	090702f

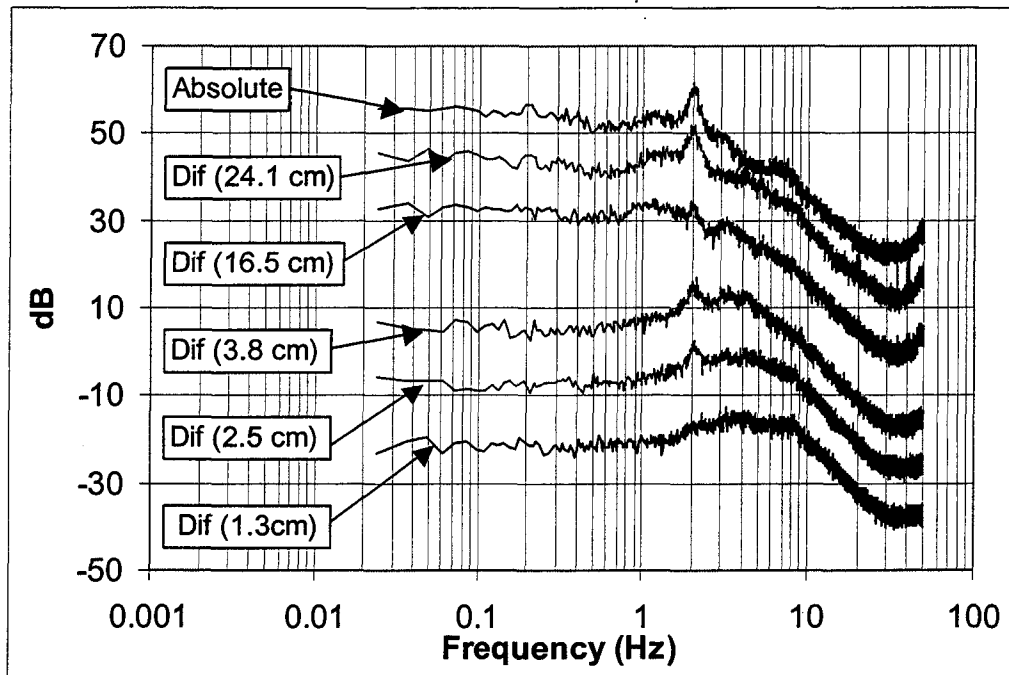


Figure 5.1: Power spectrums acquired with an absolute pressure probe technique (“Absolute”) and several differential pressure probe techniques (“Dif”) with different vertical arm spacings

for the latter is that the large 2 Hz peak filtered in the differential technique with small spacings (1.3 cm) is now dominant at one of the differential probe arms at a large spacing (e.g., 24.1 cm).

Furthermore, the results from the two probes could be used to explain the relevance of each peak in the bed. For example, the dominant frequency peak (2 Hz) associated with the absolute probe technique is not observable in the differential technique with a 1.3 cm spacing. It is therefore likely to be a global phenomena (i.e., its effect present throughout the bed) since the 2 Hz phenomena is filtered out with the differential technique by being present at each arm. In contrast, the 2 Hz to 9 Hz power band with the 1.3 cm spacing differential technique is likely to be from a local phenomena (e.g., bubble effects) that is observable once the 2 Hz phenomena is filtered out.

Test matrix data

To further understand the differences between the absolute and differential techniques, a test matrix consisting of various bed heights and probe locations within the bed was created and pressure data were acquired with each technique. Power spectrums were determined for the pressure data from each of these techniques and examined. Figure 5.2 shows the power spectrums for the four techniques studied in this research at a bed height of 16.7 cm. In the figure legend, the static-absolute pressure probe technique is designated as “Stat-abs”, the dynamic-absolute technique is designated as “Dyn-abs”, the static-differential technique is designated as “Stat-dif”, and the dynamic-differential technique is designated as “Dyn-dif”. (Volumetric flow data were not recorded for this figure, and its value was estimated from the shape of the power spectrum.)

For the dynamic techniques shown in Figure 5.2, the corresponding differential technique yielded a third peak located at just over 5 Hz, while this peak is not present with the dynamic-absolute technique. To determine the reason for this difference between the two power spectrums, a similar test was performed. For this test, the pressure fluctuations were measured with dynamic-absolute technique at the two probe arm locations where the upper and lower differential probe arms were located, along with the corresponding dynamic-differential technique. These power spectrums are shown in Figure 5.3.

Experimental Operating Conditions for Figure 5.2

Bed media	Badger 30x50 Sand	Bed height	16.7 ± 0.3 cm
Mean particle diameter	494 micron	Bed mass	5277.41 ± 0.01 gm
Particle density	2600 ± 100 kg/m ³	Pressure measurement	all
Volumetric flow	285 LPM (estimated)	Pressure probe position	10.2 ± 0.2 cm
Velocity ratio	1.1	File group	062102g

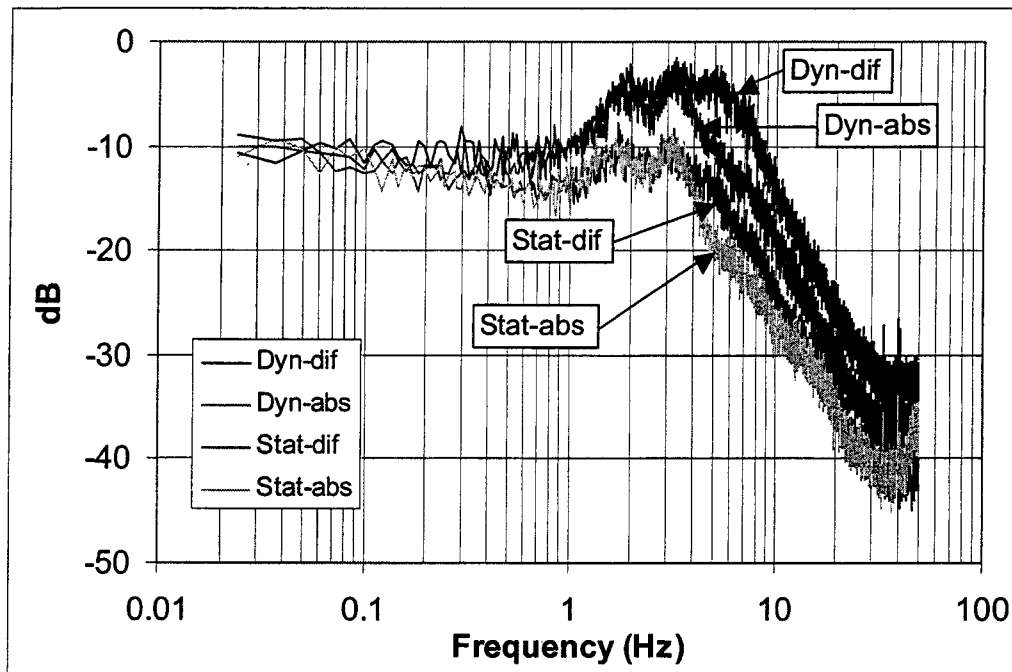


Figure 5.2: Power spectrums for the four different pressure probe techniques with a bed height of 16.7 cm and an arm position of 10.2 cm

Experimental Operating Conditions for Figure 5.3

Bed media	Badger 30x50 Sand	Bed height	16.7 ± 0.3 cm
Mean particle diameter	494 micron	Bed mass	5277.41 ± 0.01 gm
Particle density	2600 ± 100 kg/m ³	Pressure measurement	Dyn-abs, dyn-dif
Volumetric flow	273 ± 7.5 LPM	Pressure probe position	10.2 ± 0.2 cm
Velocity ratio	1.1	File group	090702e

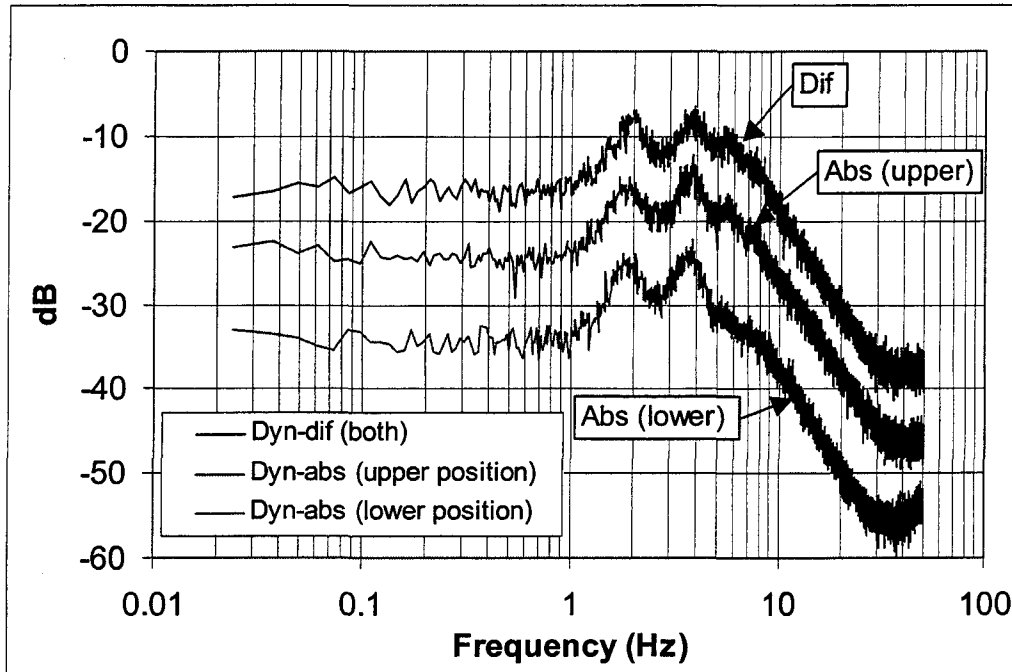


Figure 5.3: Power spectrums acquired with a differential probe technique and the absolute probe technique at the two corresponding differential probe arm positions. The arms at the “upper position” and “lower position” are at 12.7 cm and 10.2 cm, respectively, from the distributor plate.

Notice that the third peak (5-6 Hz) with the differential technique is also observed with the absolute technique at the upper arm position, but is not observed at the lower arm position. Thus, this peak is present with the differential technique because it was present at the upper arm position. In this capacity, the upper arm is not filtering out a common signal, but rather introducing a frequency peak that is only present at the upper arm position. Researchers have commented that the upper probe in the differential technique acts as a filter by canceling out common signals with the lower probe [25], but this research has shown it to be somewhat more complicated. Mainly, the upper probe is as likely to add a frequency peak as it is to subtract one.

Probe arm position effects

To understand the effect of probe arm position on the absolute and differential techniques, pressure data were acquired near the distributor plate and near the surface of a bed with the dynamic-absolute and dynamic-differential techniques. For these tests, the bed height was held constant at 34.0 cm. For the power spectrums shown in Figure 5.4, the probe arms were located at 2.5 cm from the distributor plate. For the power spectrums shown in Figure 5.5, the lower probe arms were located at 25.4 cm up from the distributor plate (8.6 cm below the surface) at the same operating conditions.

Large differences between the absolute and differential techniques were present when the probe arm was placed near the distributor. Figure 5.4 shows that the two techniques can produce extremely different power spectrums. The dynamic-absolute technique has a dominant frequency at 2 Hz and a secondary frequency of about 18 Hz. For the dynamic-differential technique, the dominant frequency is at 8 Hz and any secondary peaks are not easily recognizable. In contrast to the large differences shown in Figure 5.4, the power spectrums near the surface shown in Figure 5.5 are similar. Apparently, the global phenomena that dominated the absolute technique in Figures 5.4 and 5.5 also dominated the pressure signal at one of the differential technique's arms in Figure 5.5. That is, the phenomena's influence is larger at one arm than the other and is not filtered out. These low-frequency effects are equal at both arms near the distributor plate in Figure 5.4 and are

Experimental Operating Conditions for Figure 5.4

Bed media	Badger 30x50 Sand	Bed height	34.0 ± 0.3 cm
Mean particle diameter	494 micron	Bed mass	10554.82 ± 0.01 gm
Particle density	2600 ± 100 kg/m ³	Pressure measurement	Dyn-abs, dyn-dif
Volumetric flow	345 ± 7.5 LPM	Pressure probe position	2.5 ± 0.2 cm
Velocity ratio	1.4	File group	080802a

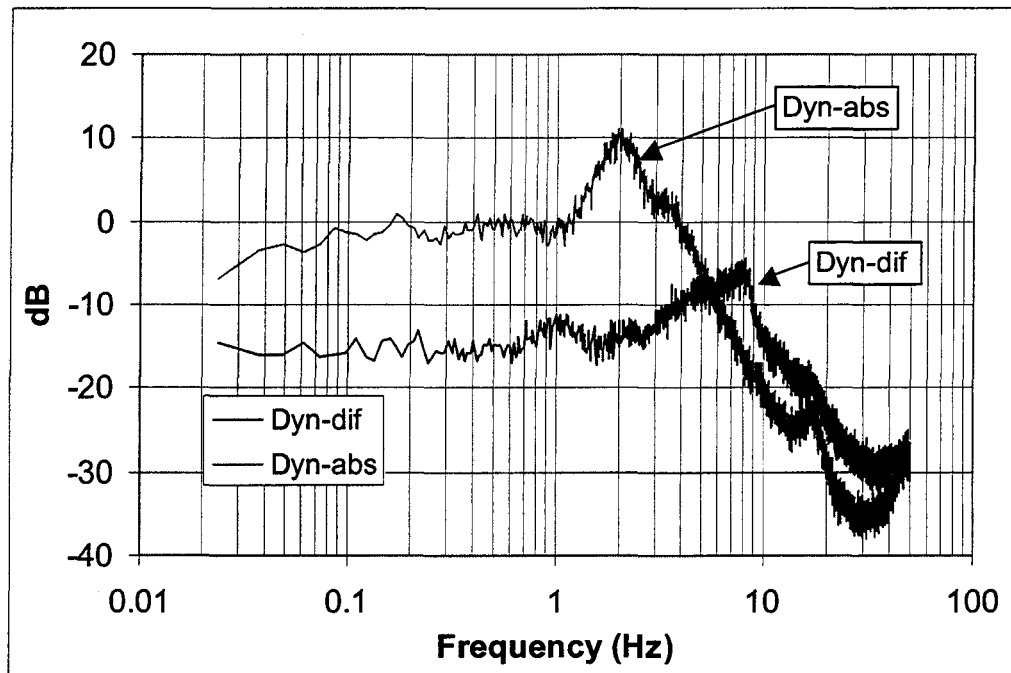


Figure 5.4: Power spectrums acquired with the absolute and differential probe techniques near the distributor plate

Experimental Operating Conditions for Figure 5.5

Bed media	Badger 30x50 Sand	Bed height	34.0 ± 0.3 cm
Mean particle diameter	494 micron	Bed mass	10554.82 ± 0.01 gm
Particle density	2600 ± 100 kg/m ³	Pressure measurement	Dyn-abs, dyn-dif
Volumetric flow	345 ± 7.5 LPM	Pressure probe position	25.4 ± 0.2 cm
Velocity ratio	1.4	File group	080802t

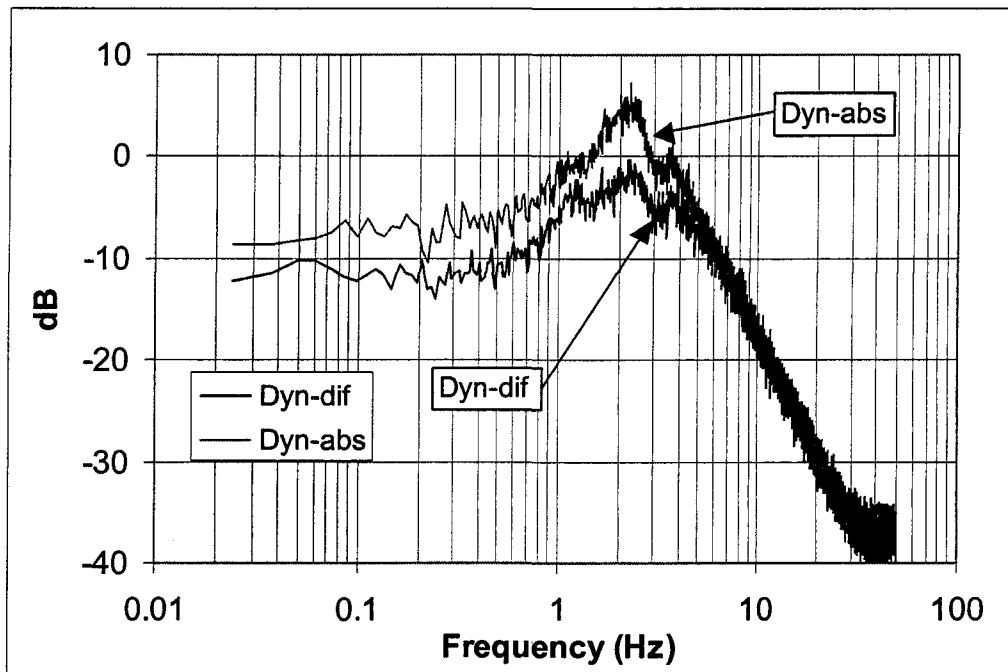


Figure 5.5: Power spectrums acquired with the absolute and differential probe techniques near the surface of the bed

filtered out with the differential technique. The result is a higher-frequency phenomena that is dominant at 8-9 Hz with the differential technique at the lower position (Figure 5.4).

Velocity effects

To understand the influence of velocity on the power spectrums with the different techniques, tests were performed at different fluidization velocities. Figure 5.6 shows the same four probe techniques as Figure 5.2 at the same operating conditions, except the velocity was increased from 23.1 cm/s to 41.5 cm/s (which relates to a velocity ratio increase from 1.1 to 2.1).

The shapes of all four spectrums are similar at the higher fluidization velocity, with both absolute power spectrums lining up and both differential power spectrums lining up. The similar shapes occurred because a turbulent-bubbling phenomena was present in the bed (confirmed visually), and the pressure fluctuations associated with this phenomena dominated the pressure signal for each technique. The absolute and differential techniques differed in magnitude because the pressure at the differential technique's second arm (upper) was subtracted from the pressure at the first (lower), which caused the pressure fluctuation to be lower. Fluidized beds are often operated at velocity ratios above 2, so it is possible that results such as the frequency of the dominant peak may be compared using any of the four techniques. Even with this in mind, it is important to measure the pressure fluctuations at the lower fluidization velocities to better understand the phenomena that occur in the bed.

Large particle effects

To determine if differences existed between the absolute and differential techniques when the bed was operated with large particles (Group D), tests were performed with 878 micron sand particles. Figure 5.7 shows the power spectrums for the static-absolute and static-differential techniques with the bed using 16x30 Badger sand.

The frequency peak at 2.2 Hz is highly visible with the differential technique, but difficult to distinguish with the absolute technique. This is likely a case where the differential technique was able to show a frequency peak that was masked by a more dominant peak (1.3 Hz) with the absolute technique. This belief is supported by the fact that

Experimental Operating Conditions for Figure 5.6

Bed media	Badger 30x50 Sand	Bed height	16.7 ± 0.3 cm
Mean particle diameter	494 micron	Bed mass	5277.41 ± 0.01 gm
Particle density	2600 ± 100 kg/m ³	Pressure measurement	All
Volumetric flow	513 ± 14.2 LPM	Pressure probe position	10.2 ± 0.2 cm
Velocity ratio	2.1	File group	070502e

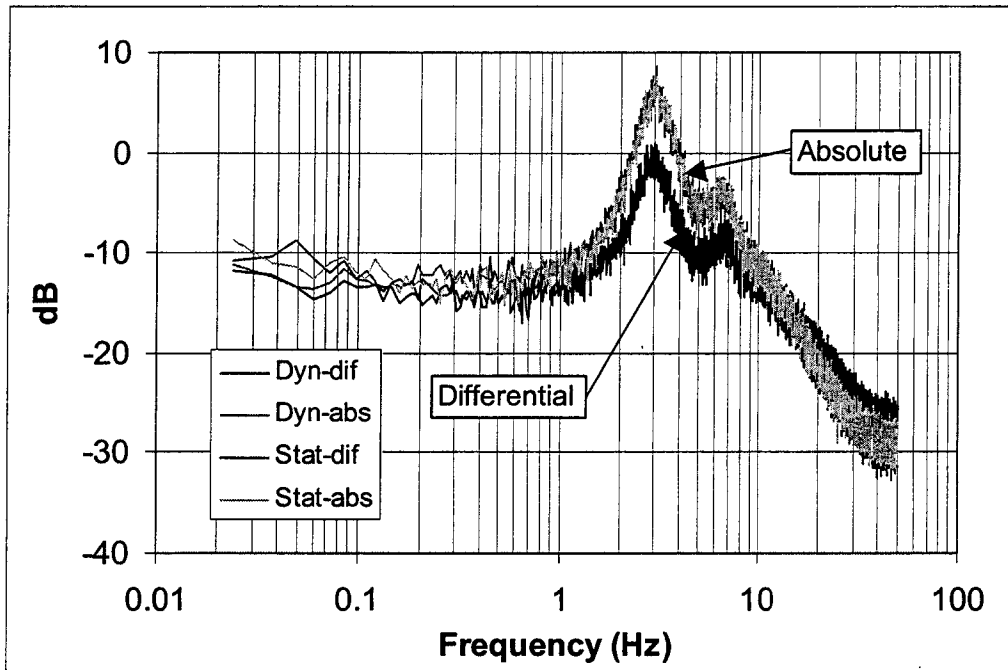


Figure 5.6: Power spectrums showing similar characteristics for the four pressure probe techniques at a fluidization velocity ratio of 2.1

Experimental Operating Conditions for Figure 5.7

Bed media	Badger 16x30 Sand	Bed height	34.0 ± 0.3 cm
Mean particle diameter	878 micron	Bed mass	10554.82 ± 0.01 gm
Particle density	2600 ± 100 kg/m ³	Pressure measurement	Stat-abs, stat-dif
Volumetric flow	479 ± 14.2 LPM	Pressure probe position	10.2 ± 0.2 cm
Velocity ratio	1.3	File group	072702h

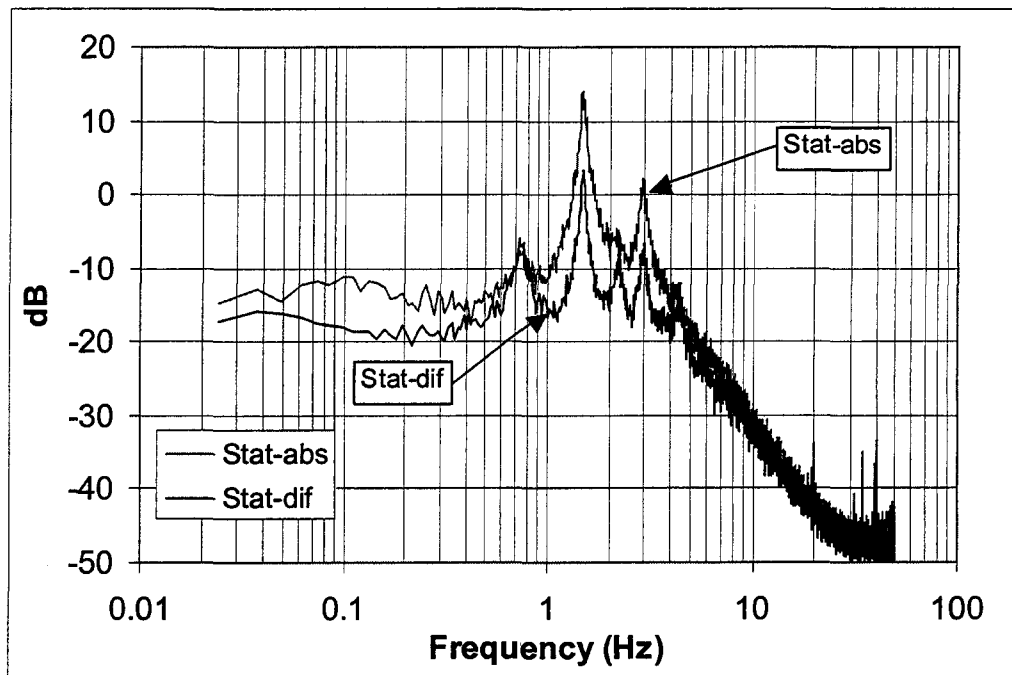


Figure 5.7: Power spectrums showing the difference in peak presence and magnitude between the absolute and differential pressure probe techniques using Group D particles

the absolute technique provides a larger magnitude on the Bode plot than the differential technique under 5 Hz.

Static and dynamic probe techniques

Along with the absolute and differential techniques, tests were also performed to determine the differences between the static and dynamic pressure probe techniques. Figure 5.2 shows all four probe techniques at the operating conditions stated in the table. As observed in this figure, the dominant frequency (3.1 Hz) and secondary (1.9 Hz) were shown with both the static and dynamic techniques. The static-differential technique also shows a small peak growth at 5 Hz that is present in the dynamic-differential power spectrum. Another difference in a few situations was that the static technique was not able to capture the higher amplitude pressure signals within the bed as compared to the dynamic technique. This is shown through the lower magnitude of the static technique compared to the dynamic technique in the Bode plot of Figure 5.2, and supported by the fact that the standard deviation of the pressure data for the dynamic technique was larger than that for the static technique. The reason that the dynamic probe provided a stronger signal (as measured through the variance or standard deviation) than the static probe was likely due to an effect from the extra 2.5 cm spacing from the bottom of the tip arm to the opening for the static probe. This spacing may have introduced flow effects at the opening that dampened the signal. Rowe and Masson [16] provide pictures of the interaction of bubbles on the probe arms that support this idea. The difference in the spectrum magnitudes shown in Figure 5.2 was not due to the influence of flow velocities changing pressure through stagnating the gas flow at the tip of the arm, as the dynamic pressure was calculated as less than one Pascal and the pressure fluctuations for this test were on the order of several hundred Pascal.

Along with the testing performed for absolute and differential techniques, pressure fluctuation data were acquired at different velocities with the static and dynamic techniques to determine its effect. Figures 5.2 and 5.6 show power spectrums measured with the dynamic and static probes at the same operating conditions, except the velocity was increased from 23.1 cm/s to 41.5 cm/s (which relates to a velocity ratio increase from 1.1 to 2.1). The power spectrums lay on top of each other when the velocity is increased, and the differences

shown in the lower-velocity power spectrums (Figure 5.2) become negligible. The spectrums became identical because a turbulent-bubbling phenomena was created as a result of an increase in velocity. This phenomena then dominated the signal measured at each arm by both techniques.

Figure 5.6 provides a good example of how there was little difference between the power spectrums provided by the static and dynamic techniques, ranging over dozens of pressure fluctuation tests. The similarity between these two techniques has been stated in the literature [22,24].

Summary of pressure probe techniques

This work has shown that the absolute and differential pressure probe techniques may produce power spectrums that vary drastically with each other. Most prominently, the magnitude and location of the dominant frequency may be very different between the two techniques. The arbitrary setting of the vertical distance between the two differential probe arms may also lead to large spectrum differences. For these reasons, researchers should proceed with caution in comparing power spectrums provided by the two techniques.

Static and dynamic pressure probe techniques were determined to provide similar power spectrums under most conditions. In a few situations, the dynamic probe provided a stronger pressure fluctuation signal (as measured through the variance) compared to the static technique. The reasons for these differences may involve effects associated with the static probe's extension from the arm opening to the tip of the arm. In summary, only small differences, if any, were observed between the static and dynamic techniques.

Probe position

Effects on dominant peaks

Pressure data were acquired at several positions in a fluidized bed to determine how the dominant frequency was affected by the arm position in the bed. Figure 5.8 shows power spectrums from seven different arm positions ranging from 1.3 cm to 7.6 cm above the distributor in a 12.7 cm fluidized bed. The spectrums are offset to clarify any differences.

Experimental Operating Conditions for Figure 5.8

Bed media	Badger 30x50 Sand	Bed height	12.7 ± 0.3 cm
Mean particle diameter	494 micron	Bed mass	3958.06 ± 0.01 gm
Particle density	2600 ± 100 kg/m ³	Pressure measurement	Dyn-abs
Volumetric flow	345 ± 7.5 LPM	Pressure probe position	Given in figure
Velocity ratio	1.4	File group	102802

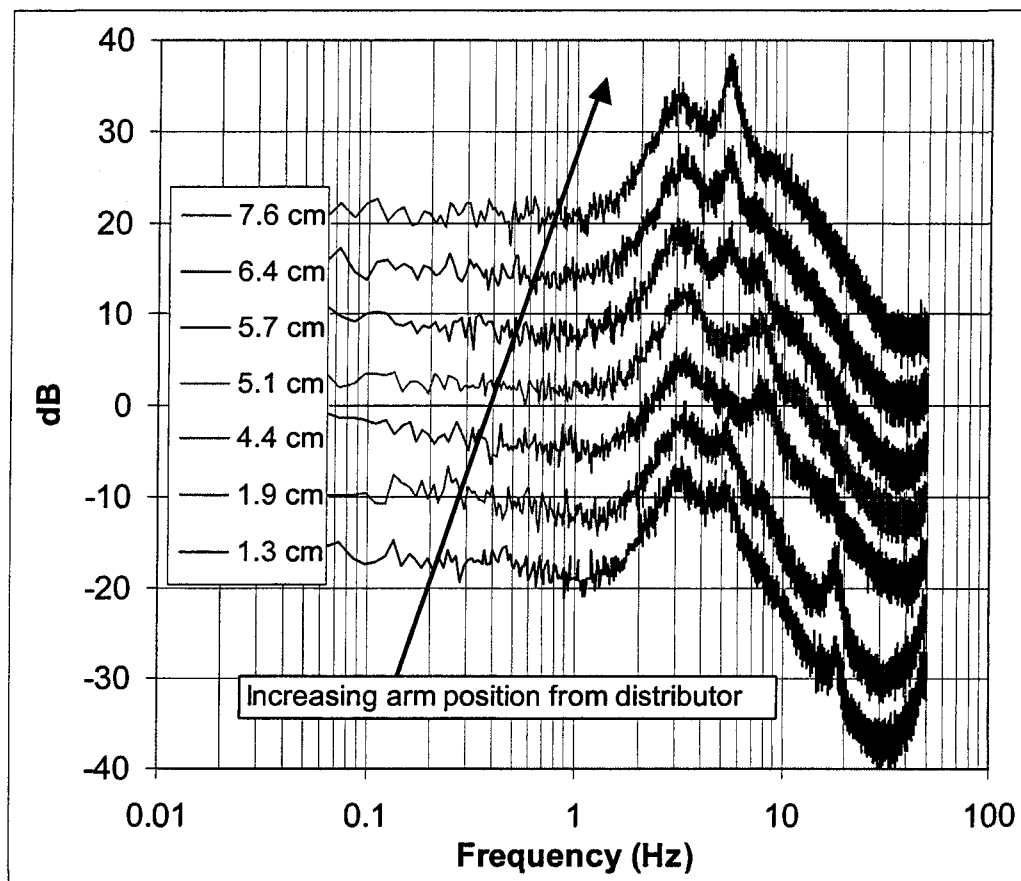


Figure 5.8: Power spectrums at different axial arm positions showing the dominant peak switch between different frequency phenomena

As shown in Figure 5.8, the dominant frequency at the lowest arm position in the bed (1.3 cm) is 3 Hz with a secondary peak at 5 Hz. At the probe arm position of 6.4 cm, both peaks have similar magnitudes, and the 5 Hz peak becomes dominant at the arm position of 7.6 cm. This ability of a secondary peak to grow and become dominant has been mentioned in the literature [2,30], but Figure 5.8 shows explicitly the growth of the secondary peak to dominance. This figure supports the idea that the growth of the 5 Hz peak may be due to the shifting of the 18 Hz peak and 8-9 Hz peak down to 5 Hz, with 7.6 cm of bed height needed for the growth to occur. This figure shows that the position of the probe arm is an extremely important testing parameter in measuring not only the dominant frequency, but also the secondary frequencies.

Effects on secondary peaks

To further understand how the secondary frequencies were affected by the position in the bed, tests were performed at a bed height higher than that used in Figure 5.8 with three different probe arm positions. Figure 5.9 shows power spectrums for three arm positions at 2.5 cm (“lower”), 5.1 cm (“middle”), and 10.2 cm (“upper”) above the distributor plate. The “middle” and “upper” spectrums are offset from the lower power spectrums by 10 dB and 18 dB, respectively, to clarify any differences.

Figure 5.9 shows that secondary peaks (18 Hz at the lower position, 8 Hz at the middle position, and 4.5 Hz at the upper position) are present in each spectrum. Although the change in bed height caused the dominant frequency to shift between Figures 5.8 and 5.9, the secondary peaks at 18 Hz and 8 Hz occurred at the same arm position. This secondary peak phenomena is therefore not a strong function of bed height.

Large-particle effects

Figure 5.7 showed that the magnitude and number of harmonics was affected by the type of probe. Tests were also performed at different probe arm positions to determine if the magnitude and number of harmonics were a function of axial arm position. Figure 5.10 shows power spectrums for two different probe arm positions in a bed with large particles (Group D). The lower arm is 10.2 cm above the distributor plate, and the upper probe is

Experimental Operating Conditions for Figure 5.9

Bed media	Badger 30x50 Sand	Bed height	34.0 ± 0.3 cm
Mean particle diameter	494 micron	Bed mass	10554.82 ± 0.01 gm
Particle density	2600 ± 100 kg/m ³	Pressure measurement	Dyn-abs
Volumetric flow	345 ± 7.5 LPM	Pressure probe position	2.5, 5.1, 10.1 ± 0.2 cm
Velocity ratio	1.4	File group	080802acg

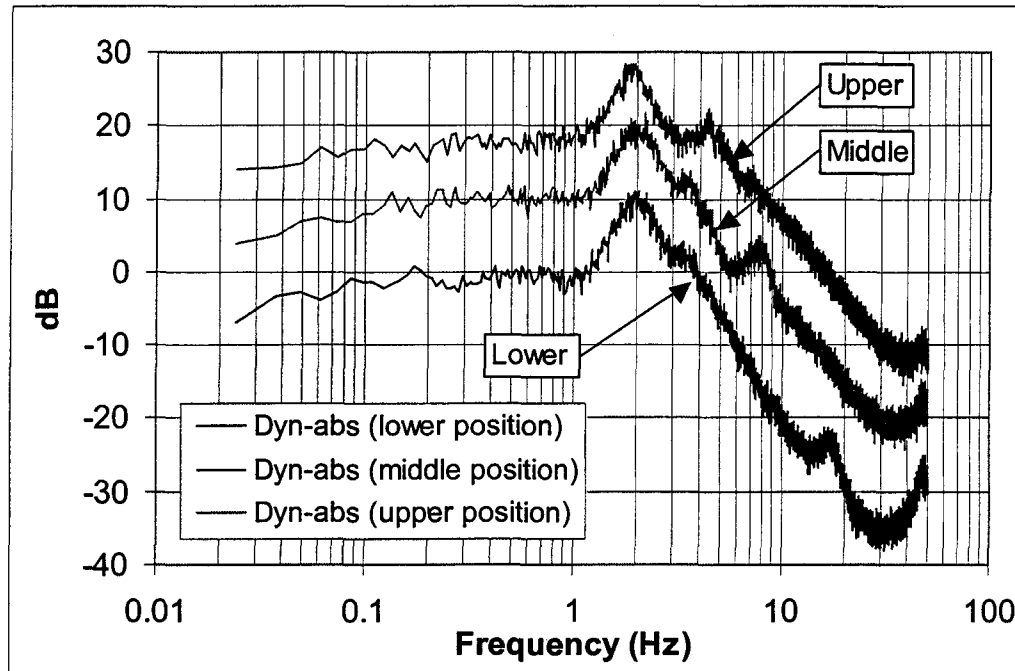


Figure 5.9: The presence of secondary peaks at lower (2.5 cm), middle (5.1 cm), and upper (10.1 cm) axial arm positions above the distributor plate in the bed

Experimental Operating Conditions for Figure 5.10

Bed media	Badger 16x30 Sand	Bed height	34.0 ± 0.3 cm
Mean particle diameter	878 micron	Bed mass	10554.82 ± 0.01 gm
Particle density	2600 ± 100 kg/m ³	Pressure measurement	Stat-dif
Volumetric flow	479 ± 14.2 LPM	Pressure probe position	10.2, 22.9 ± 0.2 cm
Velocity ratio	1.3	File group	072702hk

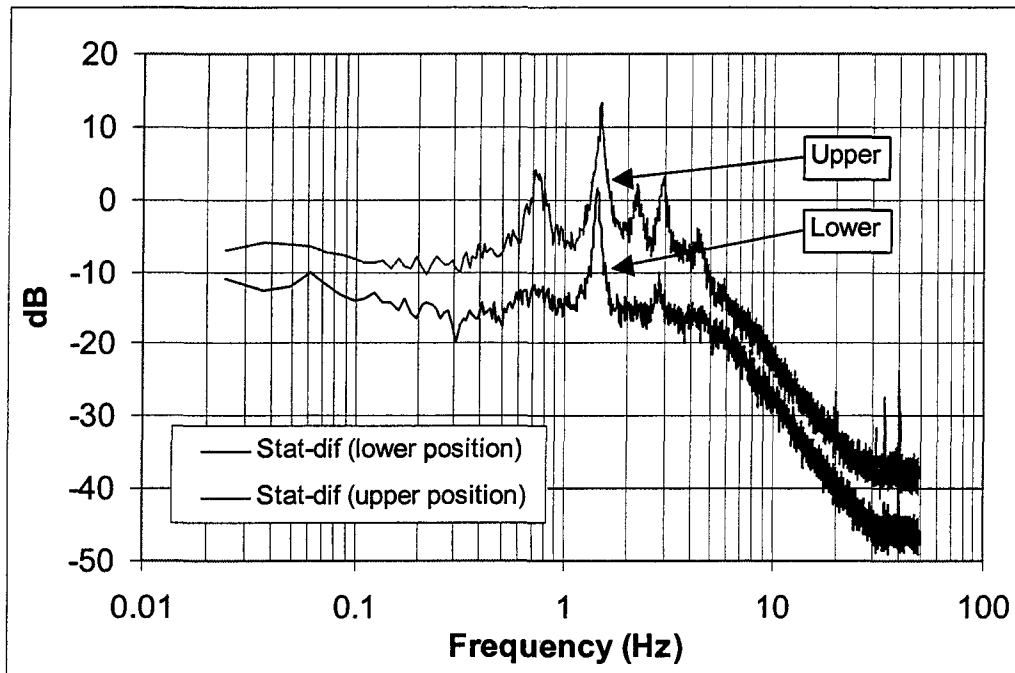


Figure 5.10: Differences in harmonics with axial arm position with the “lower position” and “upper position” at 10.2 cm and 22.9 cm, respectively, above the distributor plate

4.8 cm above the distributor plate. The upper spectrum is offset from the lower spectrum by 10 dB to clarify any differences.

As shown in this Bode plot, arm position not only affected the magnitude of the harmonics, it also showed several harmonics in the upper position (0.7 Hz, 2.2 Hz, 4.4 Hz) that were difficult to recognize in the lower position. Although the magnitude of the dominant peak did not change significantly with the 14.6 cm difference in probe position, this figure shows the importance of arm position in measuring secondary frequencies.

Summary of probe arm position effects

The results above show that the probe arm position is an extremely important testing parameter in acquiring pressure fluctuation data for spectral analysis. It is well-illustrated through Figures 5.8, 5.9, and 5.10 that such spectrum characteristics such as the dominant frequency and the number of secondary frequencies are dependent on the position in the bed. Because of this, comparing the power spectrums at several different arms positions will more accurately describe the differences between the different operating conditions as compared to a single piece of information such as the location of the dominant frequency.

Power Spectrum Characteristics

The following section describes the effect of the fluidized bed parameters on the power spectrums. These parameters include the bed height, fluidization velocity, particle density, particle diameter, and bed temperature.

The influence of bed height

To understand the influence of bed height on the power spectrum, tests were performed at different bed heights with the probe arms positioned at a constant height above the distributor plate. Figure 5.11 shows power spectrums for four different bed heights ranging from 8.6 cm to 50.8 cm with the dynamic-absolute probe arms 3.8 cm above the distributor plate.

Experimental Operating Conditions for Figure 5.11

Bed media	Badger 30x50 Sand	Bed height	Given in figure
Mean particle diameter	494 micron	Bed mass	2638.71 ± 0.01 gm 5277.41 ± 0.01 gm 7916.11 ± 0.01 gm 15832.23 ± 0.01 gm
Particle density	2600 ± 100 kg/m ³	Pressure measurement	Dyn-abs
Volumetric flow	345 ± 7.5 LPM	Pressure probe position	3.8 ± 0.2 cm
Velocity ratio	1.4	File group	102802c

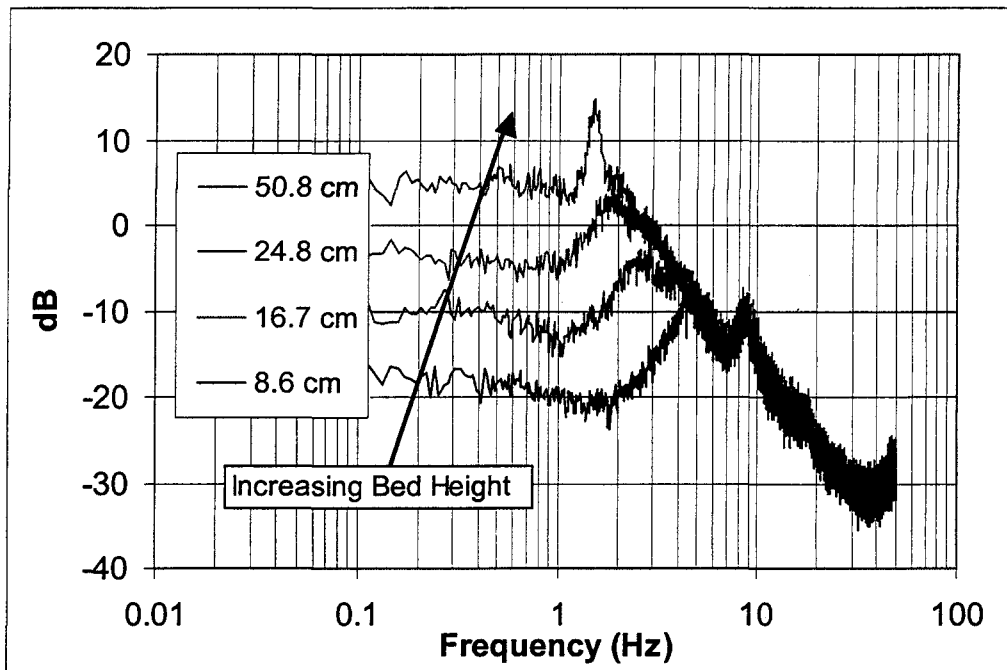


Figure 5.11: Power spectra at four different bed heights with the probe arm at a constant position from the distributor plate

Figure 5.11 shows the dominant frequency decrease in the bed as the bed height was increased with a constant arm position. The shifting of the dominant peak with bed height is a well-documented phenomena [33,43]. Using the four dominant peak frequencies, it can be shown that the frequency is inversely proportional to the bed height raised to the 0.6336 power, which is within the range reported in the literature for shallow (0.5) and deep (1.0) beds [33,43]. An expression for this is given in Equation 5.1.

$$f \propto h^{-0.6336} \quad R^2 = 0.9604 \quad (5.1)$$

The slope from each spectrum's dominant frequency to about 7 Hz (where the 8 Hz peak begins to grow) is -40 dB/decade, as is the slope from the 8 Hz secondary frequency to nearly 40 Hz. The magnitude of this slope corresponds to a second-order system. The frequency (8 Hz) and magnitude of the secondary peak did not change when sand was added to the bed, as was shown in Figures 5.8 and 5.9. Thus, the 8 Hz secondary peak was not a function of the total bed height. This contrasts with the shifting of the dominant frequency documented here and in the literature. No existence of such a secondary peak has been reported in the literature under the given conditions. This is likely due to the secondary peak being more easily recognized through the use of the Bode plot, which was only recently introduced in the literature as a method of characterizing pressure fluctuation data [11].

Power spectrums for different bed heights were also determined with the probe arm positioned at a constant depth below the surface. Figure 5.12 shows eight different bed heights with a range of 9.4 cm to 16.5 cm. For each of these tests, the dynamic-absolute probe was kept 2.5 cm below the bed's surface, and each power spectrum was offset by 6 dB to clarify any differences.

The shifting of the dominant peak to lower frequencies with an increase in bed height was continuous (no 'jumps' in frequency) and was inversely proportional to bed height raised to the 0.6508 power. An expression for this is given in Equation 5.2.

$$f \propto h^{-0.6508} \quad R^2 = 0.9984 \quad (5.2)$$

Experimental Operating Conditions for Figure 5.12

Bed media	Badger 30x50 Sand	Bed height	Given in figure
Mean particle diameter	494 micron	Bed mass	3000.00 ± 0.01 gm to 5100.00 ± 0.01 gm in steps of 300.00 gm
Particle density	2600 ± 100 kg/m ³	Pressure measurement	Dyn-abs
Volumetric flow	345 ± 7.5 LPM	Pressure probe position	Bed ht - 2.5 ± 0.2 cm
Velocity ratio	1.4	File group	110101f

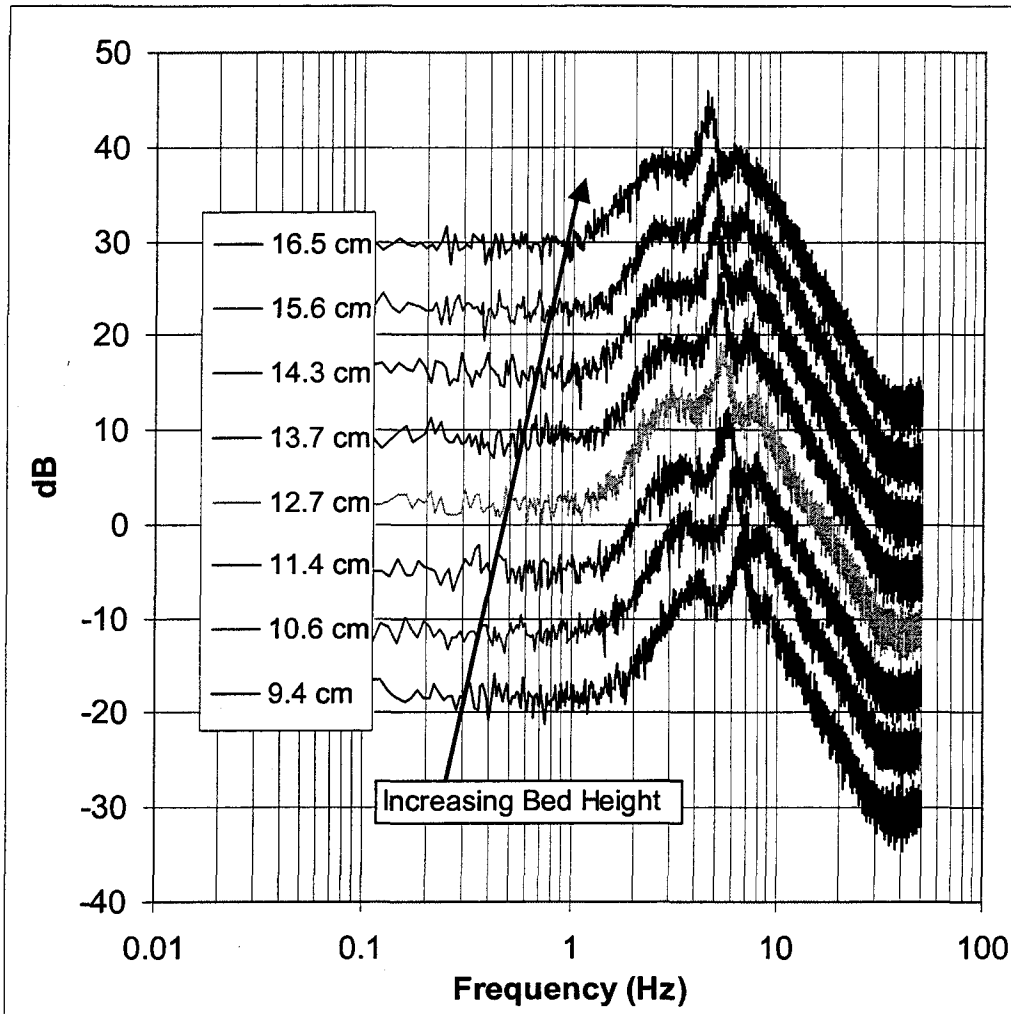


Fig 5.12: Power spectrums at eight bed heights with the probe arm at a constant position of 2.5 cm below the bed surface for each test

Similar to the data of Figure 5.11, this relationship with bed height agreed with the literature. When the arm position was kept near the surface as sand was added, the entire spectrum shifted to lower frequencies while the shape of the spectrum remained similar. This is in contrast with the power spectrums of Figure 5.11, where the amplitude of the power spectrum remained constant above a frequency of 5 Hz all probe arm positions.

Power spectrums for six bed heights (8.6 cm, 12.7 cm, 16.7 cm, 21.6 cm, 24.8 cm, and 34.0 cm) at several dynamic-absolute probe arm positions are given in Appendix C. Pressure fluctuation data for these spectrums were acquired with Badger 30x50 sand and a volumetric flow rate of 345 LPM.

The influence of fluidization velocity ratio

As shown in Figures 5.2 and 5.6, the peaks in the power spectrums changed drastically when the fluidization velocity was varied. To understand this phenomena better, tests were performed at different fluidization velocity ratios. In Figure 5.13, power spectrums are shown for velocity ratios ranging from 1.06 (265 LPM) to a velocity ratio of 1.72 (430 LPM). The velocity ratio for each spectrum is listed in parenthesis with the corresponding volumetric flow rate in the legend. The power spectrums are offset by 6 dB to clarify any differences.

By increasing the fluidization velocity ratio, peaks in the power spectrums were shown to shift in frequency and increase or decrease in magnitude relative to one another. The magnitude of each peak is shown to be a strong function of the fluidization velocity ratio, increasing in magnitude with an increase in velocity. The two dominant peaks in the power spectrum at 265 LPM (1 and 3 Hz) increase in frequency (to 3 and 5 Hz, respectively) with an increase in volumetric flow to 430 LPM. This trend of dominant frequencies increasing with velocity has been reported in the literature [30].

The dominance between these two peaks also changed with an increase in velocity ratio. As the flow was increased, the peak at 2.1 Hz in the 310 LPM power spectrum which was secondary at this flow became dominant at 400 LPM. Svoboda et al. [22] have observed this phenomena and described it as a “jump-like change”, but the Bode plot offers a more informative view of this phenomena. Mainly, both peaks were present but the increase in

Experimental Operating Conditions for Figure 5.13

Bed media	Badger 30x50 Sand	Bed height	16.7 ± 0.3 cm
Mean particle diameter	494 micron	Bed mass	5277.41 ± 0.01 gm
Particle density	2600 ± 100 kg/m ³	Pressure measurement	Dyn-abs
Volumetric flow	265 to 430 ± 7.5 LPM	Pressure probe position	10.2 ± 0.2 cm
Velocity ratio	Given in figure	File group	090902h

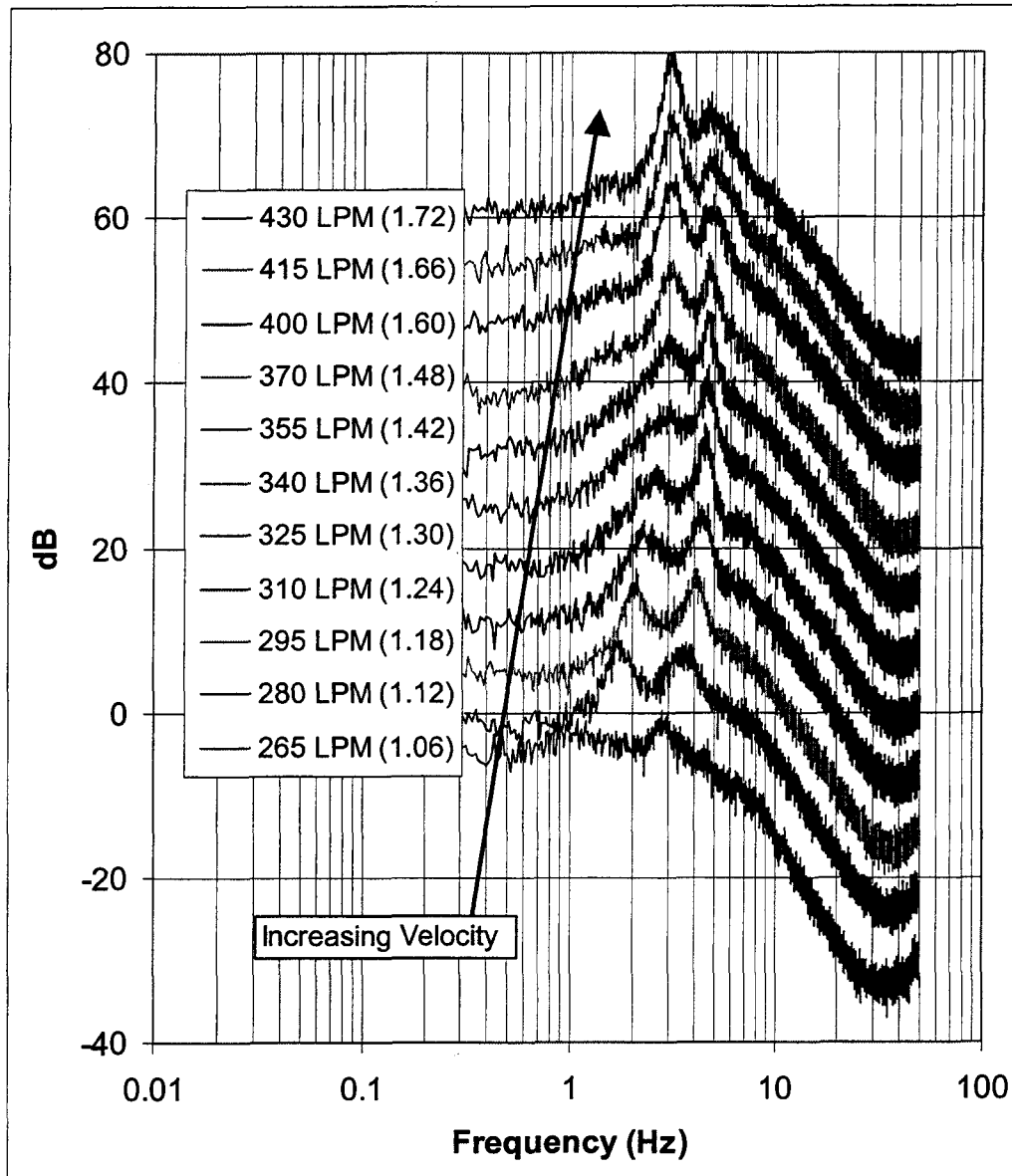


Figure 5.13: Power spectra from the bed operating at different fluidization velocity ratios

fluidization velocity brought about magnitude changes for each peak. With this view provided by the Bode plot, “jump-like changes” were not observed, but rather a gradual growth of a secondary peak to dominance. This trend of secondary peaks becoming dominant with an increase in velocity has also been reported in the literature for circulating fluidized beds [51]. Also, the magnitude change with velocity for each of the peaks has not been reported in the literature, which is useful for the modeling of multiple-peak phenomena.

The dominant peaks for the 295 LPM power spectrum are at 2 Hz and 4 Hz. By only observing this spectrum, it may have been concluded that the phenomena associated with these two peaks are harmonics of a single phenomena since they are even multiples. This theory is shown to be invalid, as the higher velocity frequency spectrums such as the 430 LPM spectrum show the frequencies increase to 3 and 5 Hz.

Figure 5.14 further illustrates the effect of fluidization velocity ratio on the power spectrums. The pressure fluctuations for these spectrums were acquired with a lower bed height than Figure 5.16, and the velocity ratios were varied from 1.18 to 1.66. The velocity ratio for each spectrum is listed in parenthesis with the corresponding volumetric flow in the legend.

By not offsetting the spectrums in Figure 5.14, the natural growth of the dominant peak shows the continuous effect of velocity on the bed. It also illustrates how well the measurement and data analysis techniques captured the physical phenomena in the bed.

The influence of particle diameter and density

In Chapter 2, particle diameter and particle density were related to fluidized bed characteristics through the Geldart classification system. Because of this, particle-diameter and particle-density tests are combined and discussed in this section.

Large-diameter particles (Group D)

It has already been illustrated in Figures 5.7 and 5.10 that when beds with Group D particles were fluidized, harmonics appeared in the power spectrums. To further understand this phenomena, pressure data were acquired with two different Group D particles. Figure 5.15 shows the power spectrums for Badger 16x30 sand and 1.1 mm glass beads, with the

Experimental Operating Conditions for Figure 5.14

Bed media	Badger 30x50 Sand	Bed height	8.3 ± 0.3 cm
Mean particle diameter	494 micron	Bed mass	2638.71 ± 0.01 gm
Particle density	2600 ± 100 kg/m ³	Pressure measurement	Dyn-abs
Volumetric flow	295 to 415 ± 7.5 LPM	Pressure probe position	2.5 ± 0.2 cm
Velocity ratio	Given in figure	File group	100902d

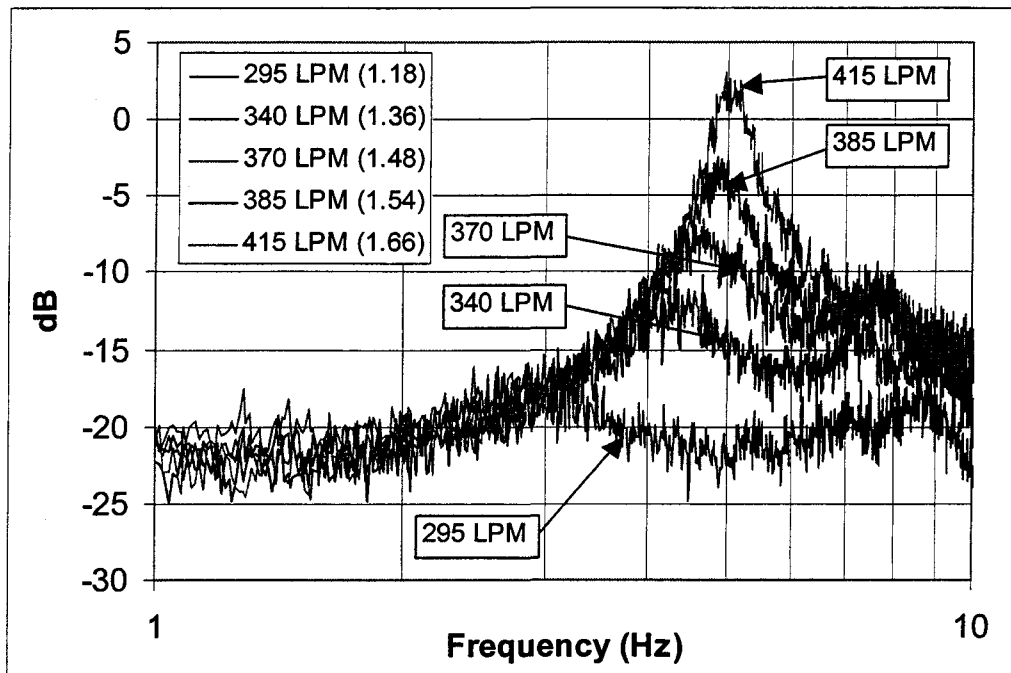


Figure 5.14: Power spectrums showing the continuous growth of the dominant peak at five different fluidization velocity ratios

glass beads spectrum offset by 10 dB. The bed masses were held constant for both tests. In the accompanying table, operating conditions with two entries list the parameter associated with the Badger sand first and the glass beads second.

Visual observation during the two tests of Figure 5.15 showed that slugging occurred in the bed during testing. As shown in this figure, the peak location and magnitude of the dominant and secondary peaks (1.45 Hz and 2.9 Hz, respectively) for the two spectrums are very similar. Agreeing with these results, Baeyens and Geldart [44] have also commented that the dominant frequency does not change for slugging beds at the same height, despite the difference in particle diameter. The use of the Bode plot also makes the secondary peak visible, whereas it would not be easily observable with the PSD technique.

To understand why the harmonics were present, the pressure fluctuations from slugging beds were examined in the time domain. Figure 5.16 shows a five-second pressure fluctuation signal for the 1.1 mm glass beads used in Figure 5.15.

The pressure fluctuations have a somewhat square-wave appearance in Figure 5.16, and visual observation of the bed showed that slugs dominated the surface of the bed. Harmonics of a perfect square wave are odd multiples of the fundamental frequency, but, as shown in Figure 5.16, the need for different multiples is evident in reconstructing the time signal as this is not a perfect square wave. Thus, harmonics are needed to construct the square-wave phenomena, and the presence of harmonics is an indication of slugging with the sand particles.

The exact location of the dominant and secondary peaks were examined to determine how close they were to multiples of each other. Figure 5.17 shows the power spectrum for a bed operating with Badger 16x30 sand. The location of four peaks are labeled on this figure. Examining the peak frequencies in Figure 5.17 shows that the peaks are nearly exact multiples of each other. Taking the fundamental frequency to be 1.465 Hz, the other peaks at 0.754 Hz, 2.905 Hz, and 4.33 Hz are then one-half, second, and third multiples of the fundamental frequency, respectively. Brue is the only other researcher to report the existence of harmonics in the literature [1]. Possible harmonic behavior have been observed in figures in the literature (e.g., Figure 2.16), but have not been commented on as actual harmonics. This phenomena is only commented on here and by Brue [1] because the Bode plot was used,

Experimental Operating Conditions for Figure 5.15

Bed media	Badger 16x30 Sand, 1.1 mm glass beads	Bed height	34.0 ± 0.3 cm, 35.2 ± 0.3 cm
Mean particle diameter	878 micron, 1.1 mm	Bed mass	10554.82 ± 0.01 gm
Particle density	2600 ± 100 kg/m ³	Pressure measurement	Dyn-abs
Volumetric flow	479 ± 14.2 LPM, 552 ± 14.2 LPM	Pressure probe position	10.2 ± 0.2 cm
Velocity ratio	1.3, 1.1	File group	072702h, 080302h

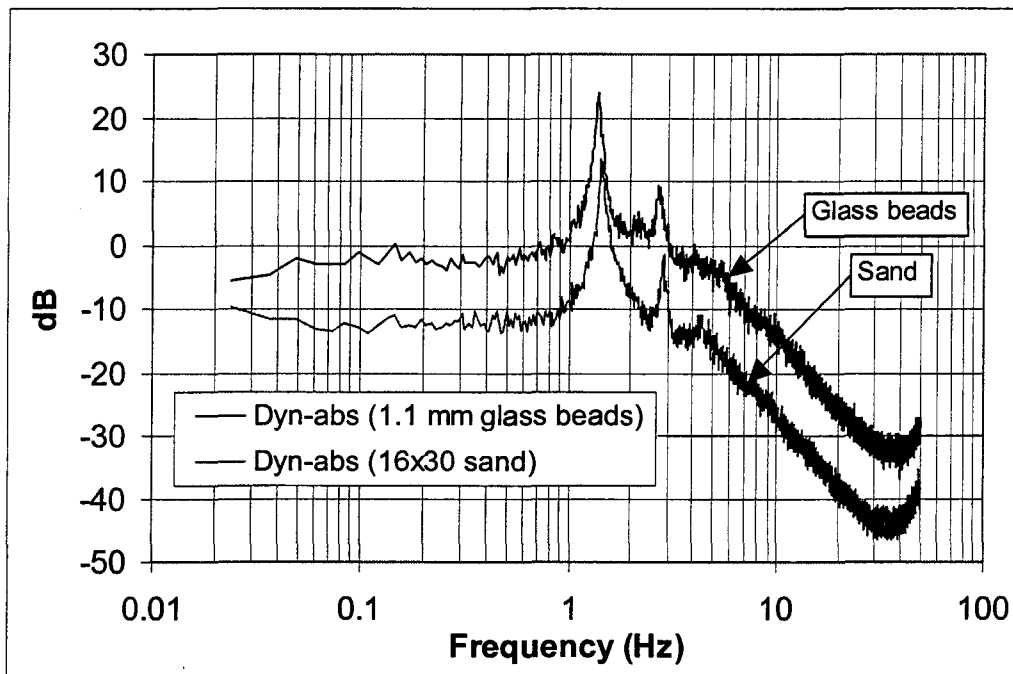


Figure 5.15: The presence of harmonics in the power spectrums with Group D glass beads and sand particles

Experimental Operating Conditions for Figure 5.16

Bed media	Glass beads	Bed height	35.2 ± 0.3 cm
Mean particle diameter	1.1 mm	Bed mass	10554.82 ± 0.01 gm
Particle density	2600 ± 100 kg/m ³	Pressure measurement	Dyn-abs
Volumetric flow	552 ± 14.2 LPM	Pressure probe position	22.9 ± 0.2 cm
Velocity ratio	1.1	File group	080302k

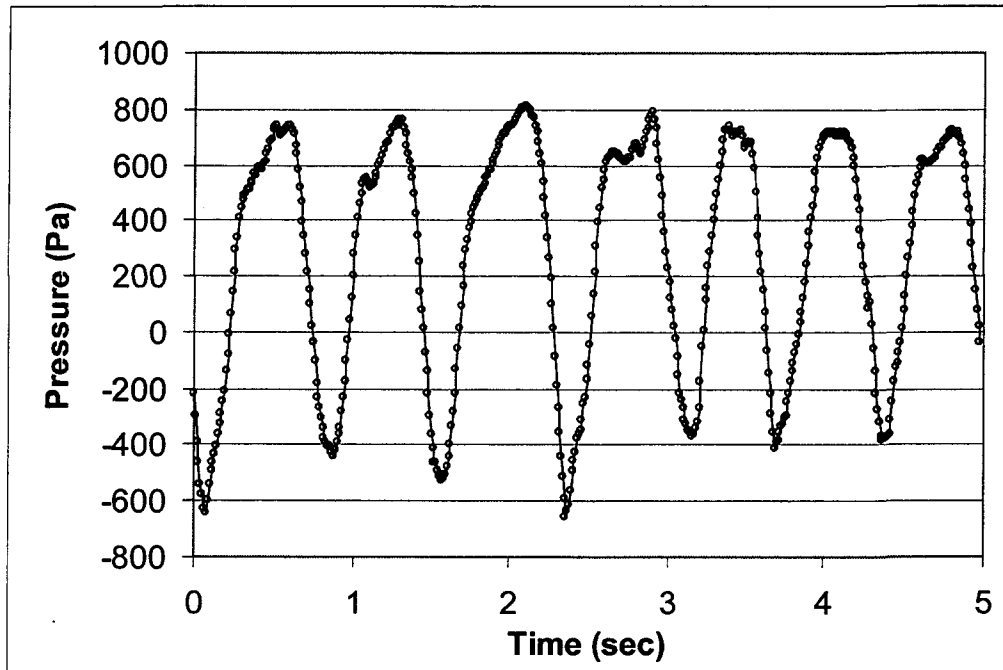


Figure 5.16: The presence of “square-wave” pressure fluctuations in the time domain with 1.1 mm glass beads

Experimental Operating Conditions for Figure 5.17

Bed media	Badger 16x30 Sand	Bed height	34.0 ± 0.3 cm
Mean particle diameter	878 micron	Bed mass	10554.82 ± 0.01 gm
Particle density	2600 ± 100 kg/m ³	Pressure measurement	Dyn-abs
Volumetric flow	479 ± 14.2 LPM	Pressure probe position	22.9 ± 0.2 cm
Velocity ratio	1.3	File group	072702k

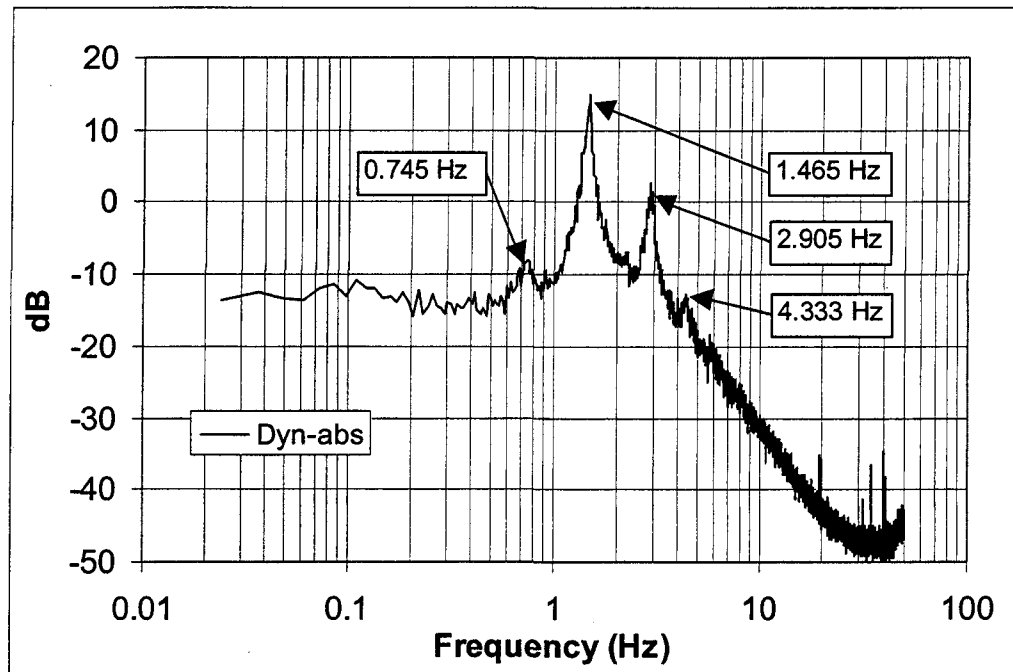


Figure 5.17: Presence of harmonics with Badger 16x30 sand

which is extremely important for recognizing multiple peaks in the power spectrum. For example, both the dominant peak (1.465 Hz, 14 dB) and second largest peak in magnitude (2.905 Hz, 2 dB) are easily recognizable in Figure 5.17, but the non-log magnitudes in the power spectrum are different by a factor of fifteen. This large difference in magnitude leads to difficulty in observing the second peak when viewed with techniques such as the PSD.

The depth of the bed was also studied to determine its effect on the magnitude and number of the harmonic peaks in the power spectrum. Figure 5.18 shows an example of this with two different bed heights. The shallow and deep bed heights are 18.1 cm and 34.0 cm, respectively, and the fluidization velocity and probe position were kept constant.

When sand was added to the lower-height bed, the harmonics were shown to initiate and grow. This is illustrated by the secondary peak increasing in magnitude with an increase in bed height. Also, the pressure fluctuations in the time domain for the shallow bed appeared sinusoidal and less ‘square’ than the pressure fluctuations for the deep bed. Harmonic frequencies were also present in power spectrums that were measured in a boiler by Brue [1]. Brue attributed these harmonics to effects from the coal feed system. This assessment may be in error as it is likely that the bed was slugging as the particle size was up to 1 mm, and the height to bed diameter ratio was over four (18.3 m high with a 4.3 m by 4.3 m square bed).

High-density particles (Group D)

As illustrated in Figure 2.4, the transition from Group B to Group D particles may occur by increasing the particle diameter or by increasing the particle density. As Group D particles with large diameters were examined in the previous section, Group D particles with high density are examined in this section. Steel particles with a diameter of 390 micron and a particle density of 7600 kg/m^3 were fluidized in the bed and the corresponding power spectrum is shown in Figure 5.19. Because the volumetric flow for this test was greater than the range of the rotameter, the flow was set to minimum fluidization with a valve. Since the flow rate exceeded the measurable range, the entries for “Volumetric flow” and “Velocity ratio” in the table are labeled as “Out of range”.

Experimental Operating Conditions for Figure 5.18

Bed media	Badger 16x30 Sand	Bed height	18.1 ± 0.3 cm 34.0 ± 0.3 cm
Mean particle diameter	878 micron	Bed mass	5277.41 ± 0.01 gm 10554.82 ± 0.01 gm
Particle density	2600 ± 100 kg/m ³	Pressure measurement	Dyn-abs
Volumetric flow	479 ± 14.2 LPM	Pressure probe position	10.2 ± 0.2 cm
Velocity ratio	1.3	File group	072702gh

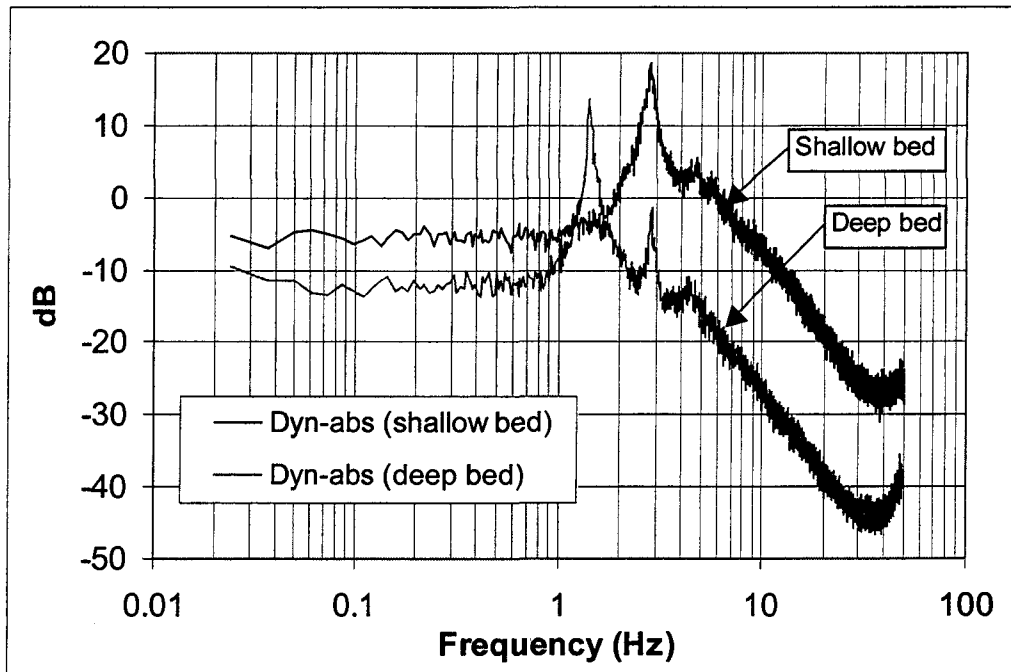


Figure 5.18: Increase of harmonic behavior with an increase in bed height from a shallow bed (18.1 cm) to a deep bed (34.0 cm)

Experimental Operating Conditions for Figure 5.19

Bed media	Steel shot	Bed height	18.1 ± 0.3 cm
Mean particle diameter	390 micron	Bed mass	15832.23 ± 0.01 gm
Particle density	7600 ± 100 kg/m ³	Pressure measurement	Dyn-dif
Volumetric flow	Out of range	Pressure probe position	10.2 ± 0.2 cm
Velocity ratio	Out of range	File group	090602a

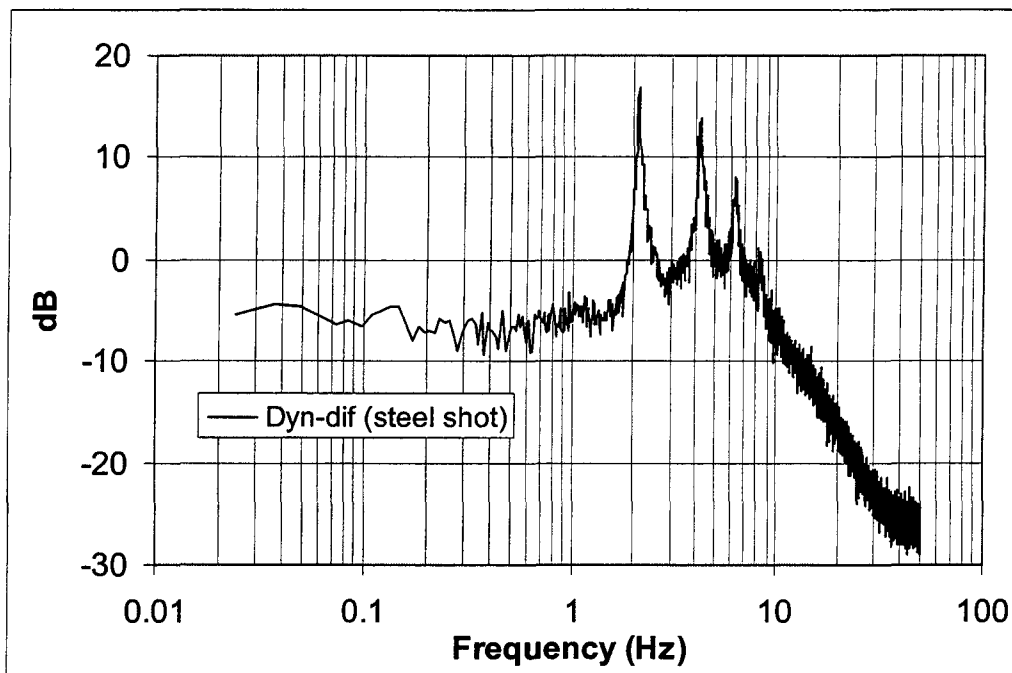


Figure 5.19: The presence of harmonics in the power spectrum with high-density steel particles

Harmonic frequencies are shown in this figure at 2.1, 4.2, 6.3, and 8.4 Hz, and the pressure traces showed the square-wave characteristics in the time domain similar to those for the large sand particles in Figure 5.16. Although harmonics are well-illustrated in this figure, visual observation during fluidization showed individual bubbles at the bed surface, not slugs that covered most of the bed cross-section. The pressure fluctuations had a square-wave appearance in the time domain similar to slugging with Group D sand particles. With the steel particles, the square-wave phenomena is associated with the larger gas forces needed to move the heavier particles. For example, a bubble in a steel-particle bed needs more force to displace the particles compared to a bubble in a sand-particle bed.

Low-density particles (Group A)

To determine the characteristics of power spectrums from Group A particles, tests were performed with low-density particles. Figure 5.20 shows the power spectrum from plastic particles with a diameter of 200 micron and a specific density 0.63.

Testing of these low-density particles produced a power spectrum that had a first-order decay slope of -20dB/decade . Group A particles tend to have small bubbles compared to Group B particles, and it is likely that small-diameter, low-density particles exhibit first-order characteristics due to this decreased effect from the smaller bubbles. An implication to this is that non-bubbling fluidized beds (Group A particles under certain conditions) may always exhibit first-order characteristics. This is supported by Smith and Corripio [63], who showed that the pressure in a tank has first-order response to changes in flow into and out of the tank. Although this first-order phenomena is not well-understood, the Bode plot shown in Figure 5.20 provides initial information for understanding this phenomena.

Summary of particle diameter and density effects

The previous figures have shown several spectrum differences that varied with particle diameter and density. These included first-order characteristics (e.g., Figure 5.20) as established through the decay slope, multiple-peak phenomena occurring in the bed (e.g., Figure 5.2), and harmonic behavior (e.g., Figure 5.17). To understand these characteristics better, the Geldart classification system was re-examined with the types of particles used in

Experimental Operating Conditions for Figure 5.20

Bed media	Plastic spheres	Bed height	29.8 ± 0.3 cm
Mean particle diameter	200 micron	Bed mass	2500.06 ± 0.01 gm
Particle density	630 ± 100 kg/m ³	Pressure measurement	Dyn-abs
Volumetric flow	37.8 ± 2.8 LPM	Pressure probe position	22.9 ± 0.2 cm
Velocity ratio	2.0	File group	080302f6

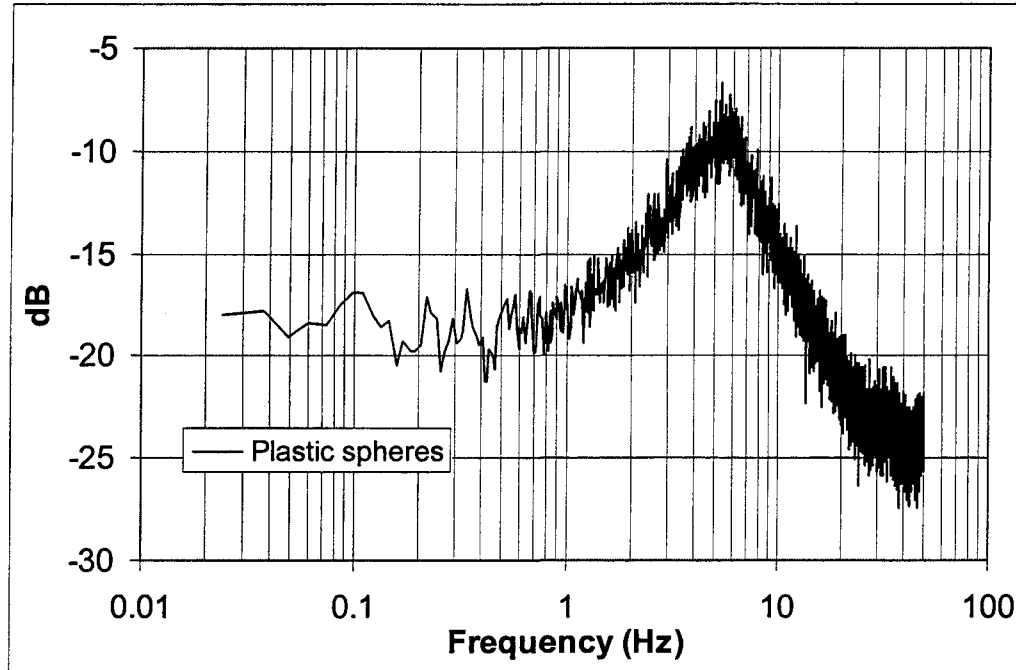


Figure 5.20: Power spectrum with low-density plastic particles showing first-order behavior

this research. Figure 5.21 shows the Geldart classification system from Figure 2.4 with the five types of particles tested in this research noted on the figure. Particle information is listed in the accompanying table.

Particle data for Figure 5.21

Reference number	Particle type	Mean diameter	Density
1	Plastic	200 micron	630 kg/m ³
2	Sand	494 micron	2600 kg/m ³
3	Sand	878 micron	2600 kg/m ³
4	Glass	1100 micron	2600 kg/m ³
5	Steel	390 micron	7600 kg/m ³

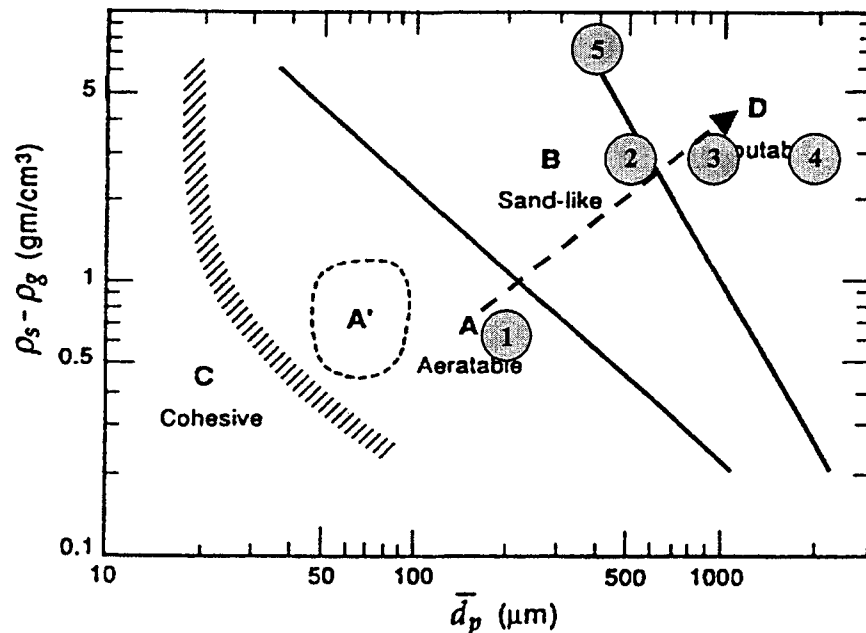


Figure 5.21: Geldart classification system with the plastic (1), sand (2,3), glass (4), and steel (5) particles examined in this research imposed on the figure

Following the dashed arrow in Figure 5.21, bubble size generally increases from relatively small bubbles with the Group A particles, to larger bubbles with the Group B particles, to slugs with the Group D particles. This transition through the Geldart Groups is

accompanied by first-order dynamics (Group A), second-order dynamics with multiple-peak phenomena (Group B), and harmonic behavior (Group D), respectively. As the change in spectrum characteristics occur at the transition between particle classifications, they are likely linked to the same bubble effect phenomena that account for the classification differences (e.g., square-wave pressure fluctuations from slugging yielding the harmonics).

The influence of temperature

As discussed in the literature review of Chapter 2, the effect of temperature on the power spectrum is not well-understood. To study this effect, pressure fluctuation data were acquired with bed temperatures ranging from 21° C to 512° C. The bed height and probe arm position were constant for all tests. The velocity ratios for these nine power spectrums were set within a range of 1.3 to 1.5. Figure 5.22 shows the resulting power spectrums for these tests, with the velocity ratio listed in parentheses after the bed temperature in the legend. The spectrums are offset to clarify any differences.

In Figure 5.22, the dominant frequency (4-5 Hz) and two secondary frequencies (2-3 Hz, 6-7 Hz) remain constant throughout the temperature range. The dominant frequency varied within a 1 Hz range (4-5 Hz), which agreed with the range of shifting in Fan et al.'s [20] dominant frequencies (Figure 2.18). Furthermore, the use of the Bode plot shows that the secondary frequencies and general shape of the power spectrums remain fairly constant for the given temperature range.

Fluidization velocity tests were also performed with the same operating conditions as those in the previous figure at 512° C, except the fluidization velocity ratio was varied from 1.3 to 2.3. These tests are shown in Figure 5.23 (with offset spectrums) and were performed to understand the effect of fluidization velocity on the peaks in the power spectrums.

The two noticeable dominant peaks (1.9-2.9 Hz and 4.6-5.0 Hz) showed growth with increasing velocity similar to velocity tests at ambient temperature shown in Figure 5.13. The main difference between these two figures is that the dominant peak at the highest flow rate in Figure 5.13 was secondary at lower flow rates, whereas the dominant peak remained at 4-5 Hz in all of the spectrums shown in Figure 5.23. More testing should be performed at different velocity ratios and temperatures to determine if any odd frequency “jumping”

Experimental Operating Conditions for Figure 5.22

Bed media	Badger 30x50 Sand	Bed height	16.8 ± 0.3 cm
Mean particle diameter	494 micron	Bed mass	5277.41 ± 0.01 gm
Particle density	2600 ± 100 kg/m ³	Pressure measurement	Dyn-abs
Volumetric flow	345, 204, 192, 146, 118, 96, 98, 81, and 66 ± 7.5 LPM	Pressure probe position	14.0 ± 0.2 cm
Velocity ratio	1.3 – 1.5	File group	110202, 110502

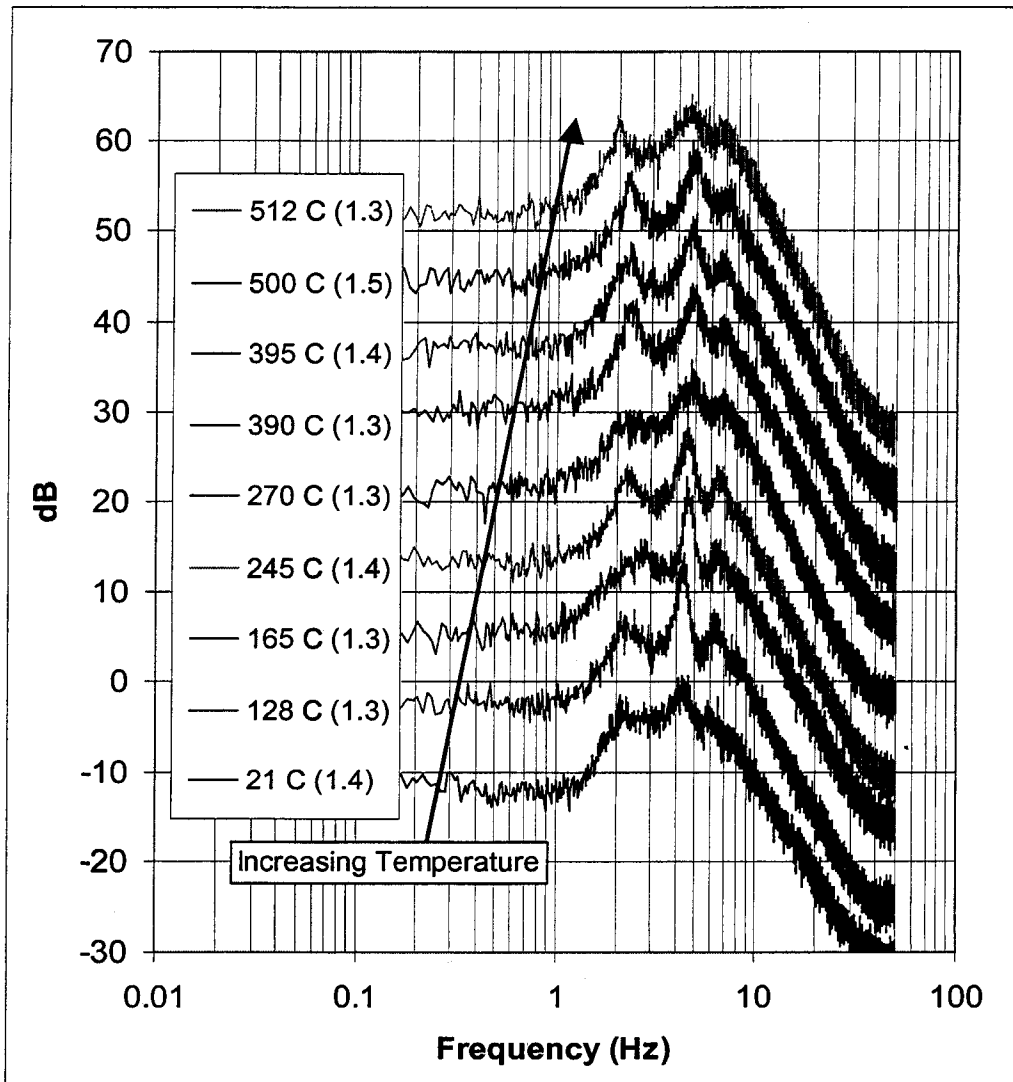


Figure 5.22: Power spectra at bed temperatures ranging from 21° C to 512° C with the velocity ratio set between 1.3 and 1.5

Experimental Operating Conditions for Figure 5.23

Bed media	Badger 30x50 Sand	Bed height	16.8 ± 0.3 cm
Mean particle diameter	494 micron	Bed mass	5277.41 ± 0.01 gm
Particle density	2600 ± 100 kg/m ³	Pressure measurement	Dyn-abs
Volumetric flow	70.2, 81.0, 91.8, 102.6, 113.4, and 124.2 ± 7.5 LPM	Pressure probe position	14.0 ± 0.2 cm
Velocity ratio	Given in figure	File group	110202

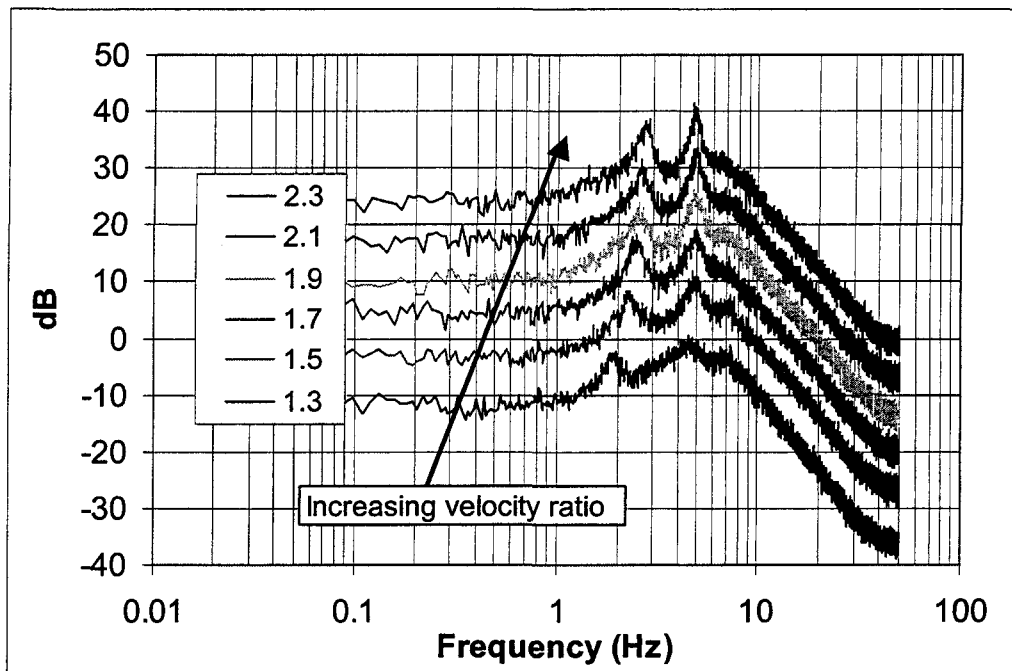


Figure 5.23: Power spectrums at a bed temperature of 512° C with the velocity ratio varied from 1.3 to 2.3

illustrated by Svoboda et al. (Figure 2.17) appears. If changes in fluidization velocity produce changes in the secondary peaks of the power spectrum, such testing may explain the wide scatter and odd trends in Fan et al.'s data [20]. The testing shown in Figures 5.22 and 5.23 provides initial information for understanding the effect of temperature on the multiple peaks in the power spectrums.

Multiple-Peak Phenomena

Several researchers have shown that fluidized beds may have more than one peak present in the power spectrum (e.g., [22]), agreeing with this research. The presence and interaction of these multiple-peak phenomena are well-illustrated with the Bode plot. The Bode plot is extremely important in detecting multiple-peak phenomena as it allows low-magnitude peaks which are not highly apparent with the PSD technique to be more recognizable.

Examples of multiple-peak phenomena in the power spectrums

As observed in the power spectrums of Figure 5.9, high-frequency, low-amplitude peaks are present in the spectrums along with low-frequency, high-amplitude dominant peaks. Similar to these peaks in Figure 5.9, Figure 5.24 shows the spectrums for ten probe arm positions in a 24.8 cm bed. The arm position for each power spectrum is labeled in the legend as the distance that the arm was located above the distributor. For example, the bottom power spectrum was acquired with the arm positioned at 1.3 cm above the distributor in the 24.8 cm bed. The different peaks that were present in these power spectrums are noted in the figure. Each of these peaks will be discussed in the following sections.

In Figure 5.23, peaks "1" to "6" are located at frequencies of 47, 18, 8, 6, 3, and 2 Hz, respectively. Similar figures for six different bed heights (8.6 cm, 12.7 cm, 16.7 cm, 21.6 cm, 24.8 cm, and 34.0 cm) are provided in Appendix C. For the given bed material and fluidization velocity, peaks similar to "1" through "4" were observed at the same probe arm position in the figures in Appendix C. These four peaks are very recognizable with the Bode plot, but it would be very difficult to recognize these peaks with the PSD technique because

Experimental Operating Conditions for Figure 5.24

Bed media	Badger 30x50 Sand	Bed height	24.8 ± 0.3 cm
Mean particle diameter	494 micron	Bed mass	7916.11 ± 0.01 gm
Particle density	2600 ± 100 kg/m ³	Pressure measurement	Dyn-abs
Volumetric flow	345 ± 7.5 LPM	Pressure probe position	Given in figure
Velocity ratio	1.4	File group	092702k

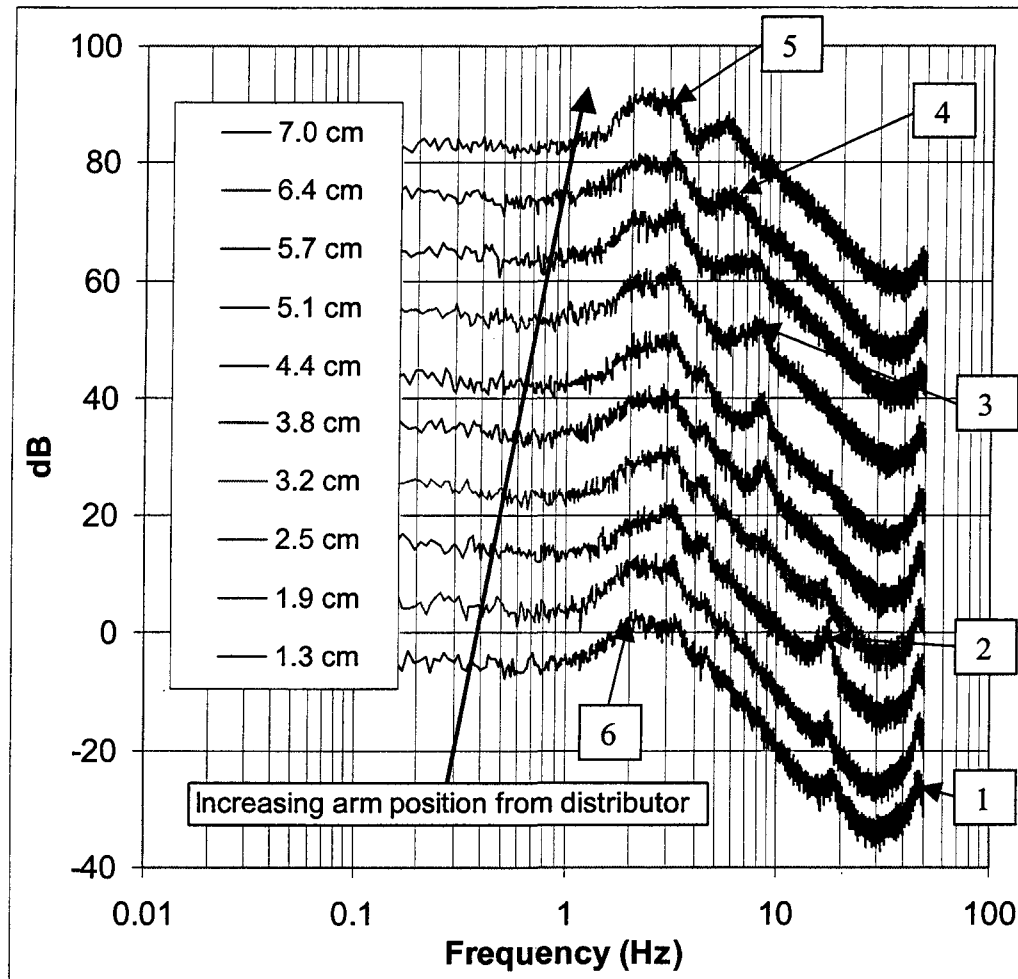


Figure 5.24: The presence of multiple-peak phenomena (numbered 1 to 6) in the power spectrums at different probe arm positions in a fluidized bed with a height of 24.8 cm

their magnitudes are so much lower in magnitude than the dominant frequency. Also observed in these figures, the dominant frequencies in each of these figures (e.g., peaks “5” and “6” in Figure 5.23) were strongly dependent on bed height.

Peak “1” frequency phenomena (47 Hz)

The peak with the highest frequency observed in Figure 5.24 was a low-amplitude phenomena at 47 Hz that was measured at a low position in the bed. This peak is present in all of the power spectrums shown in this figure, but has the largest magnitude at the lowest arm position. The location of this peak shifted slightly from 50 Hz at a bed height of 8.6 cm height to 46 Hz at a bed height of 34.0 cm bed height, as shown in Appendix D.

Researchers have previously attributed this peak to an artifact of the spectral analysis algorithms [66], but this testing has shown that this is an unlikely hypothesis. First, the 46-50 Hz peak was present in power spectrums acquired with the absolute probe technique, but not the differential technique. If this phenomena was due to the algorithm, it would be present with both techniques. Second, the fact that the peak varied in frequency with a change in bed height supports the idea that it is a function of bed parameters and not related to the analysis algorithm.

To understand the physical significance of peak “1”, air was passed through a 1 cm high bed, and the bed surface was observed. It was visually confirmed that no bubbles were present in the bed as the gas flow jetted through the distributor holes and past the sand to the atmosphere. To further understand this jet phenomena, calculations [13] were performed to determine the jet height. These calculations showed that the jet height for the given conditions in Figure 5.24 was 1.5 cm, which is similar to the arm position where peak “1” was present. Thus, peak “1” is linked to jetting effects at the distributor plate.

Testing also showed that the magnitude of this peak was not affected by the radial position of the probe arm. This ubiquitous effect agrees with how the high-restriction distributor spreads flow evenly throughout the bed. In addition, initial CFD modeling (MFIx) has shown that a similar low-magnitude, high-frequency peak was present in the computational pressure data under similar operating conditions [67]. A power spectrum from a limited number of MFIx data points is shown in Figure 5.25.

MFIX Model Operating Conditions for Figure 5.25

Bed diameter	16 cm	Bed height	24 cm
Particle diameter	500 micron	Bed mass	7916.11 ± 0.01 gm
Particle density	2650 kg/m ³	Pressure measurement	Absolute
Volumetric flow	357 LPM	Pressure probe position	18 cm
Velocity ratio	1.4	Sample time (data points)	85 sec (8500 points)

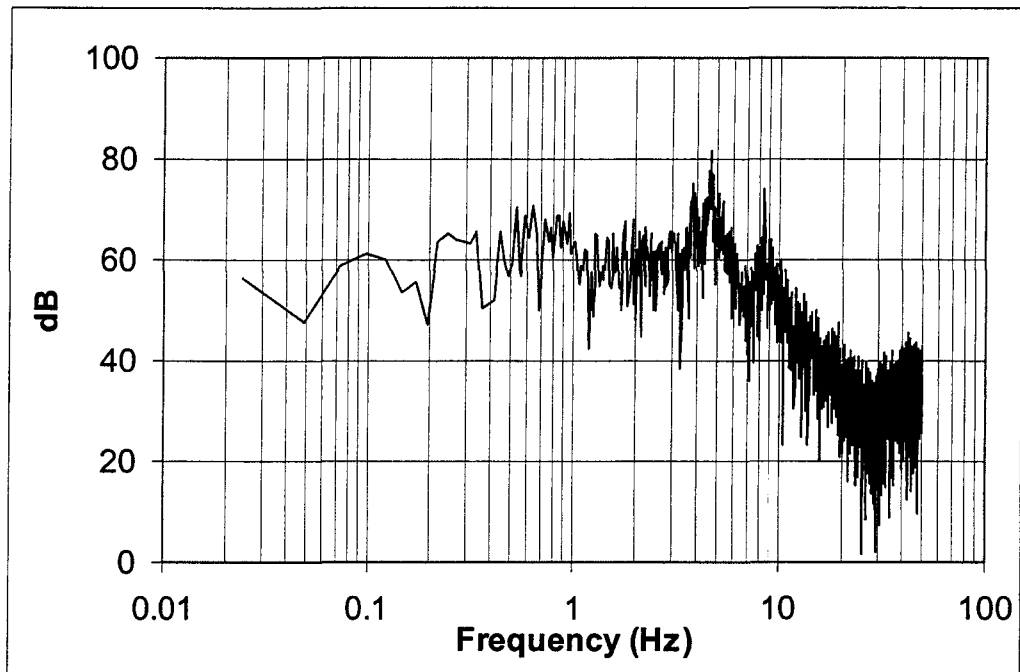


Figure 5.25: A power spectrum with pressure fluctuation data from a CFD modeling software (MFIx)

Along with the presence of the low-magnitude, high-frequency peak similar to peak “1”, Figure 5.25 shows several other characteristics. These include the presence of multiple-peak phenomena (3.8, 4.7, 8.4, and 42 Hz) and a decay slope similar to a second-order system.

Peak “2” frequency phenomena (18 Hz)

A second high-frequency, low-amplitude phenomena was present in several of the power spectrums shown in Figure 5.24. This peak was largest in magnitude at a position of 2.5 cm above the distributor plate and was located at 18 Hz. To understand this 18 Hz peak, pressure fluctuation data were taken at different radial positions with the probe arm 2.5 cm above the distributor plate. Figure 5.26 shows power spectrums at two different radial positions (Position 1 and 2 are at 2.7 cm and 5.4 cm from the center of the bed, respectively) in a 8.6 cm bed. The power spectrums are offset by 10 dB to clarify the differences between the two spectrums.

The “Position 2” spectrum has a large magnitude peak at 18 Hz, while this peak is barely visible in the “Position 1” spectrum. Peaks similar in magnitude to that shown in Position 2 were present in seven of the nine radial positions tested. To further understand this peak, a bed with a height of 2.5 cm was fluidized and visually inspected. The surface of this bed showed small bubbles escaping the surface at various radial positions at high frequencies. The fact these small, high-frequency bubbles were present supports the idea that the 18 Hz peak is associated with bubble phenomena.

Few studies have commented that the magnitude of the pressure fluctuations is a function of radial position (e.g., [30,31]), but there is little mention in the literature of how secondary peaks are related to radial position. Figure 5.26 provides an example of how pressure fluctuation measurements at different radial positions may be used to explain the different frequency phenomena occurring in the bed. This is not mentioned in the literature because the Bode plot, which is needed to observe the low-magnitude phenomena, is a relatively new technique.

Experimental Operating Conditions for Figure 5.26

Bed media	Badger 30x50 Sand	Bed height	8.3 ± 0.3 cm
Mean particle diameter	494 micron	Bed mass	2638.70 ± 0.01 gm
Particle density	2600 ± 100 kg/m ³	Pressure measurement	Dyn-abs
Volumetric flow	290 ± 7.5 LPM	Pressure probe position	2.5 ± 0.2 cm
Velocity ratio	1.2	File group	092202d

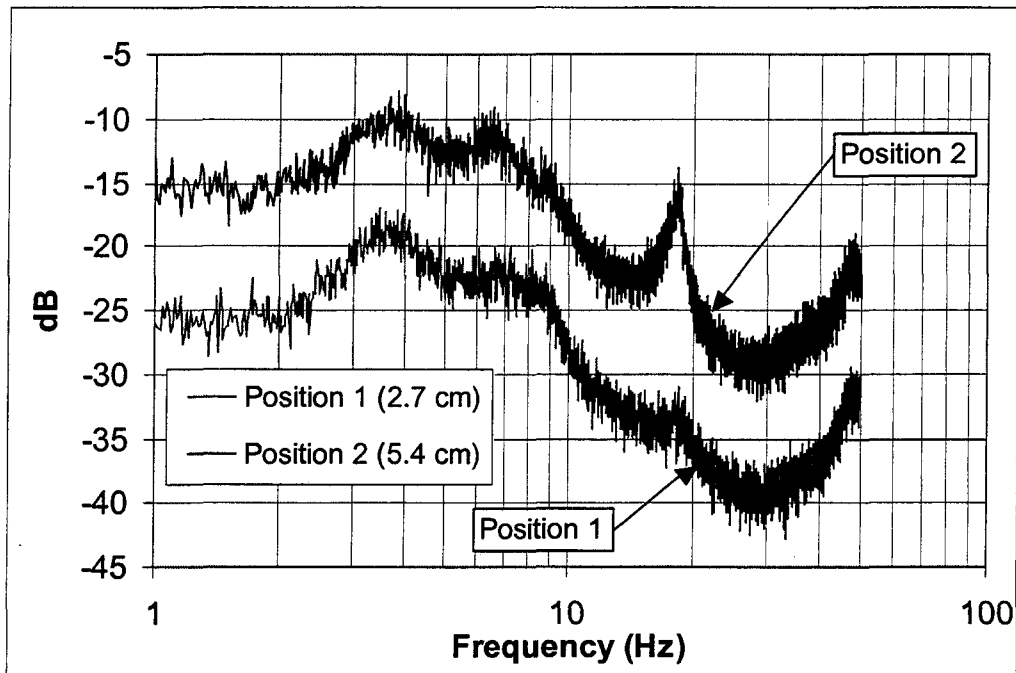


Figure 5.26: Power spectrums for two different radial positions (Positions 1 and 2 at 2.7 cm and 5.4 cm, respectively, from the center of the bed) with the probe arm at a constant height (2.5 cm) from the distributor plate

Peak “3” frequency phenomena (8-9 Hz)

To study the third peak labeled in Figure 5.24, radial position testing similar to that described above for peak “2” was performed and shown in Figure 5.27. The axial position of the probe arm was 4.4 cm from the distributor plate, and the bed height was 16.7 cm. The spectrums are not offset. Position 1 is at the center of the bed, and Position 2 is at 3.9 cm from the center of the bed.

Figure 5.27 shows that the magnitude of the 8-9 Hz peak varied drastically with radial position, suggesting that this peak is a local effect (e.g., bubble coalescence). Testing at twelve other radial positions showed that the center position yielded the highest-magnitude peak. The belief that this is a local effect is further supported by Figure 5.4, which shows the differential (local) probe technique yielding a 8 Hz peak that was not observed in the absolute (global) probe technique. Also, Figure 5.27 shows that the 47 Hz peak may not decrease in magnitude with bed height as shown in Figure 5.24, but may rather be masked by relatively lower-frequency, higher-magnitude frequency phenomena.

Peaks “4”, “5”, and “6” frequency phenomena (1-6 Hz)

Radial testing similar to that shown in Figures 5.26 and 5.27 for peaks “2” and “3” frequency phenomena was done near the surface of the bed to understand the higher-amplitude, lower-frequency phenomena. Figure 5.28 shows two power spectrums with the arm position at 2.5 cm below the surface of a 24.8 cm bed. The arm positions are located radially at the center of the bed (Position 1) and at 6.7 cm from the center of the bed (Position 2). The spectrums in Figure 5.28 are not offset.

Figure 5.28 shows that the magnitude of the frequency peak at 4.5 Hz (peak “4”) was affected by radial position, as was the peak at 3.1 Hz (peak “5”). Other power spectrums measured at radial positions between the two in Figure 5.28 showed that the magnitude of these two peaks decreased as the arm was moved from the center of the bed. Figure 5.24 and those in Appendix C also showed that dominant (and often second-most dominant peak) were located at all axial positions within the bed. As shown in Figure C.4 for this case, peaks “5” and “6” were located at nearly all axial position in the bed, while peak “4” was located across a smaller axial range. This characteristic of peak “4” is similar to those of peaks “2”

Experimental Operating Conditions for Figure 5.27

Bed media	Badger 30x50 Sand	Bed height	16.7 ± 0.3 cm
Mean particle diameter	494 micron	Bed mass	5277.41 ± 0.01 gm
Particle density	2600 ± 100 kg/m ³	Pressure measurement	Dyn-abs
Volumetric flow	290 ± 7.5 LPM	Pressure probe position	4.4 ± 0.2 cm
Velocity ratio	1.2	File group	101102f

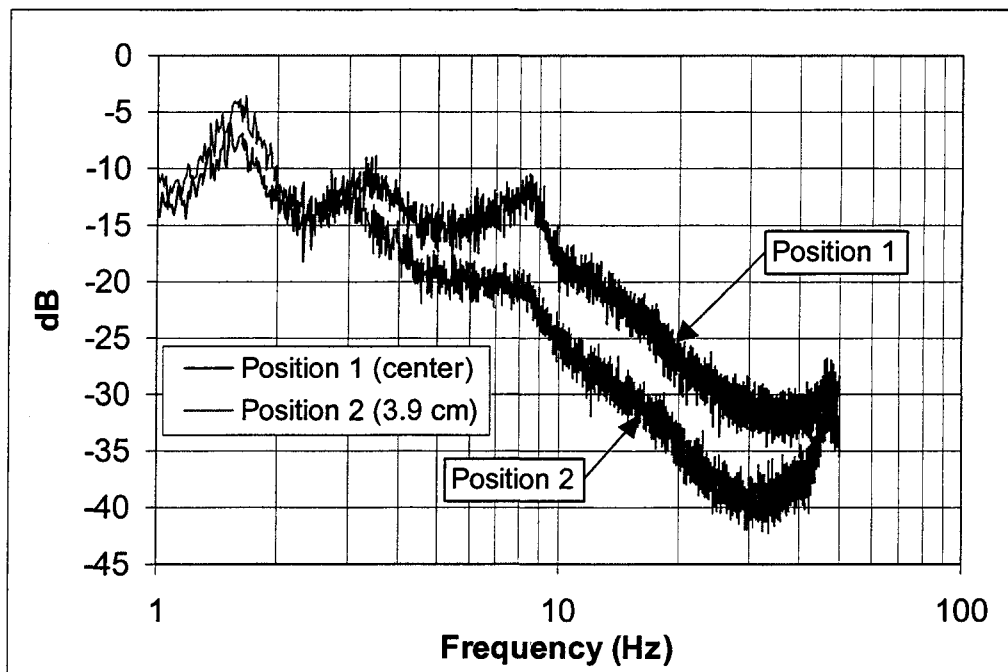


Figure 5.27: Power spectrums for two different radial positions (Positions 1 and 2 at the center of the bed and 3.9 cm from the center of the bed, respectively) with the probe arm at a constant height (4.4 cm) from the distributor plate

Experimental Operating Conditions for Figure 5.28

Bed media	Badger 30x50 Sand	Bed height	24.8 ± 0.3 cm
Mean particle diameter	494 micron	Bed mass	7916.11 ± 0.01 gm
Particle density	2600 ± 100 kg/m ³	Pressure measurement	Dyn-abs
Volumetric flow	345 ± 7.5 LPM	Pressure probe position	22.3 ± 0.2 cm
Velocity ratio	1.4	File group	110302k

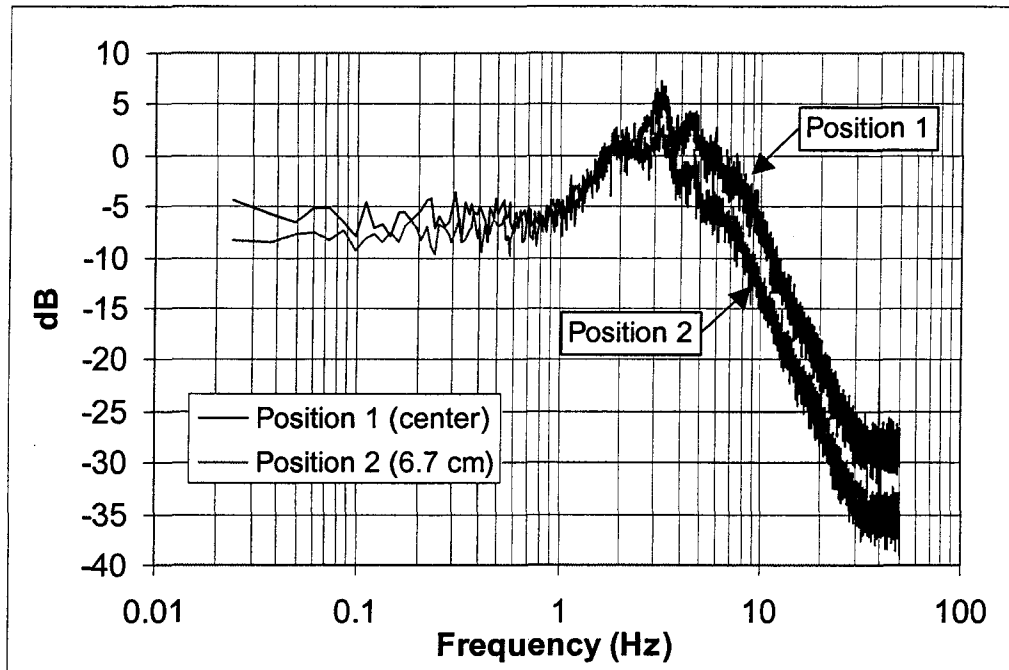


Figure 5.28: Power spectrums for two different radial positions (Positions 1 and 2 at the center of the bed and 6.7 cm from the center of the bed, respectively) with the probe arm at a constant height (22.3 cm) from the distributor plate

and “3”, and is therefore also a local phenomena.

Summary of multiple-peak phenomena

The figures presented in this section have shown that the location and magnitude of frequency phenomena are strongly dependent on the location in the bed. The highest frequency phenomena (peak “1”) shown in Figure 5.24 was linked to jet effects at the distributor plate. Peaks “2”, “3”, and “4” were attributed to local phenomena. The testing associated with the lower-frequency, higher-magnitude dominant peaks (peaks “5” and “6”) showed that the largest peak magnitudes occurred at the center of the bed and were present at all axial positions within the bed.

Bubble coalescence theory

One theory to explain some of the multiple-peak phenomena (peaks “2”, “3”, and “4”) observed in the above section is that bubble coalescence is associated with the frequency phenomena. Bubble coalescence has been reported as a cause of pressure fluctuation by several researchers [34,43]. The Darton model on bubble coalescence explained in Chapter 2 is re-illustrated in Figure 5.29. As an extension to this model, it is theorized here that the bubble coalescence causes a pressure fluctuation at the coalescence frequency and coalescence location within the bed. Also, the coalescence of larger bubbles causes a correspondingly larger-amplitude pressure phenomena in the power spectrum.

Several specific characteristics of the Darton model agree with the data. The first common characteristic involves the experimental frequency peaks (“2”, “3”, and “4”) and the number of bubbles predicted by the model. If the experimental frequencies are related to bubble coalescence phenomena, then the experimental frequencies (as a function of axial position in the bed) should be proportional to the number of bubbles in the bed (as a function of axial position). This is because the number of bubbles is proportional to the frequency of bubbles coalescing (i.e., coalescence occurs more often when more bubbles are available).

As a first step in determining the number of bubbles as a function of axial position from the distributor, the equivalent bubble diameter “ D_e ” (Equation 5.3) was calculated from the Darton equation [53],

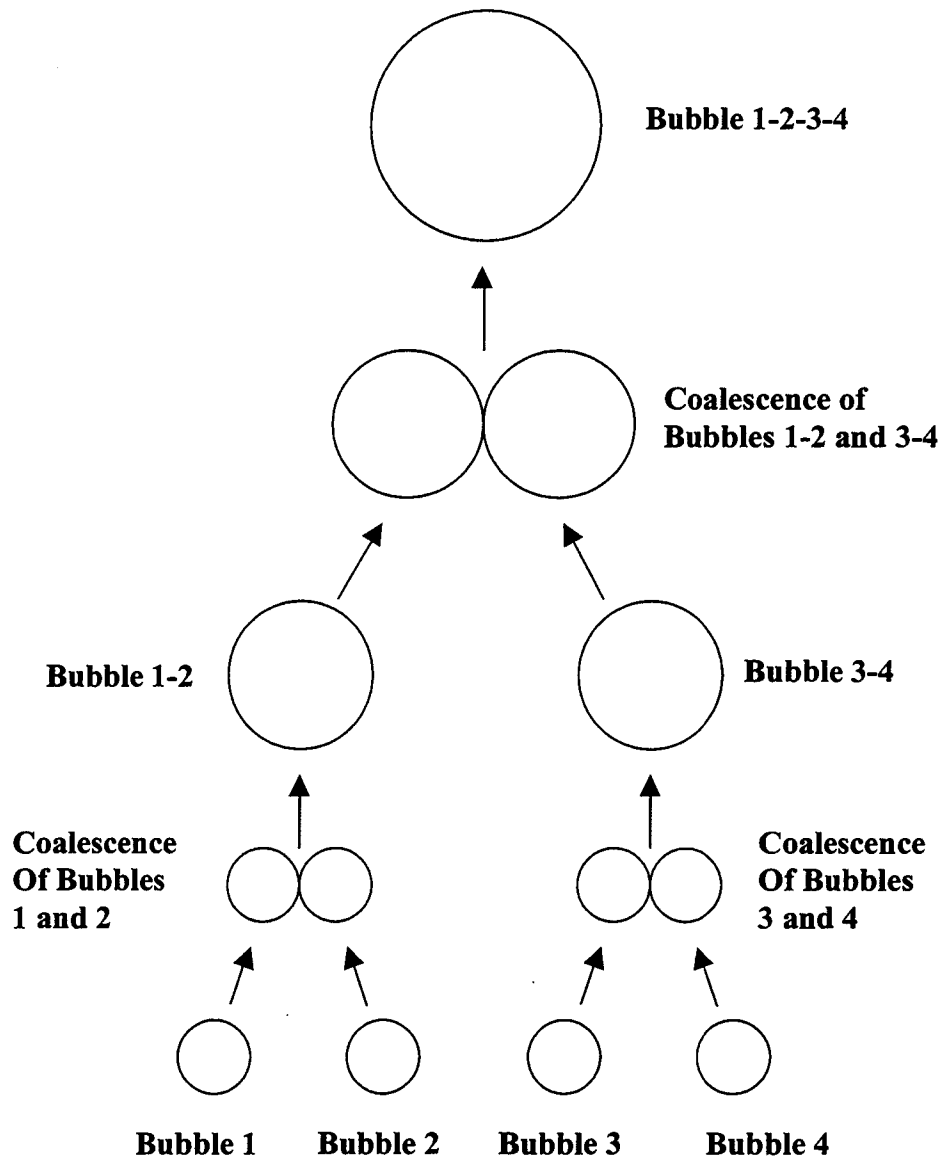


Figure 5.29: A re-illustration of the bubble coalescence model developed by Darton et al. [53] and described in Chapter 2

$$D_e = 0.54 \cdot (u - u_{mf})^{\frac{2}{5}} \cdot (z + 4 \cdot \sqrt{A_o})^{\frac{4}{5}} \cdot g^{-\frac{1}{5}} \quad (5.3)$$

where “ u ” is the superficial velocity, “ u_{mf} ” is the minimum fluidization velocity, “ z ” is the axial position in the bed above the distributor plate, “ A_o ” is the distributor plate area per distributor hole, and “ g ” is the gravitational constant. The equivalent bubble diameter is diameter of the sphere that would have the same bubble volume. This diameter was then used in Equation 5.4 to calculate the volume of a single bubble.

$$\text{Single bubble volume} = \frac{\pi}{6} \cdot D_e^3 \quad (5.4)$$

To determine the volume of fluidizing gas that passes through the bed via bubbles, a postulate of the two-phase flow theory [13] was used. This postulate states that the volumetric flow of fluidizing gas passing through the bed via bubbles can be estimated as the volumetric flow of gas above which is needed to fluidize the bed. The total bubble volumetric flow is then given in Equation 5.5,

$$\text{Total bubble volumetric flow} = (u - u_{mf}) \cdot A_{dis} \quad (5.5)$$

where “ A_{dis} ” is the distributor plate area. Using Equations 5.4 and 5.5, the number of bubbles “ N_b ” that pass through the bed per second at the given height can be calculated by Equation 5.6.

$$N_b = \frac{\text{Total bubble volumetric flow}}{\text{Single bubble volume}} \quad (5.6)$$

The theoretical number of bubbles from the equations above are shown in Table 5.1 at the axial positions that correspond to each peak. These axial positions of the experimental

frequency peaks are determined from Figure 5.24. Along with this, the experimental frequencies corresponding to each peak are given.

Table 5.1: Axial positions, bubble quantities, and experimental frequencies for peaks 2, 3, and 4

Peak	Axial position (cm)	Number of bubbles	Exp. frequency (Hz)
2	2.5	459	18
3	4.4	297	8.5
4	7.0	182	5.5

Using the data from Table 5.1, the experimental frequencies were plotted against the axial positions, and a power curve was fitted to the data points. This fitted curve is shown in Equation 5.7.

$$\text{Exp. frequency} = 50.5 \cdot (z)^{-1.158} \quad R^2 = 0.9909 \quad (5.7)$$

where “z” is the axial position in centimeters. Similarly, the number of bubbles were plotted against the axial position, and a power curve was fitted to the data points. This curve is shown in Equation 5.8.

$$\text{Number of bubbles} = 1064 \cdot (z)^{-0.894} \quad R^2 = 0.9917 \quad (5.8)$$

The exponents of the above power curves (-1.158, -0.894) are in good agreement, indicating that the two curves provide the same trend. To compare the two equations graphically, Equations 5.7 and 5.8 are plotted together in Figure 5.30. The constant in Equation 5.8 was modified so that 36 bubbles exist at the lowest axial position tested (2.5 cm).

Figure 5.30 shows that the general trend of the experimental frequencies of peaks “2”, “3”, and “4” along the axial position agrees with the number of bubbles calculated from theory. As the number of bubbles decreases due to coalescence, this figure supports the

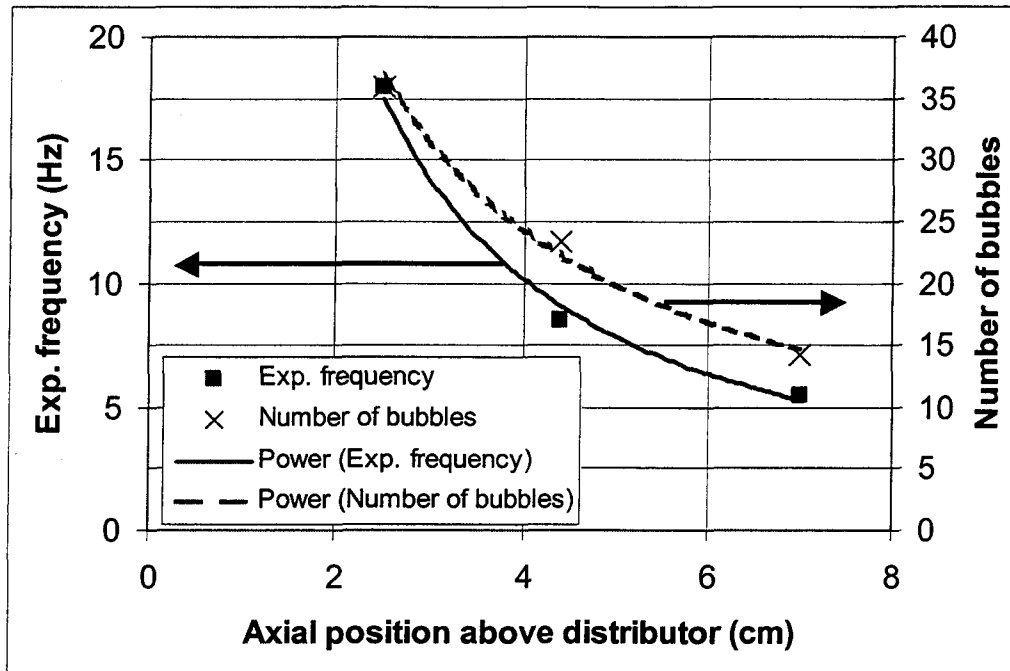


Figure 5.30: Experimental frequencies from peaks “2”, “3”, and “4” and the theoretical number of bubbles from Equation 5.8 for the given axial position above the distributor

belief that the decrease in the frequency of peaks “2”, “3”, and “4” with axial position is due to bubble coalescence.

The second characteristic that links the experimental frequencies to the bubble coalescence model involves the amplitude of the experimental frequencies. In the model, the amplitude of coalescence increases with distance from the distributor plate; thus, higher-frequency phenomena have a smaller amplitude peaks. This relationship was observed experimentally, as the relationship between peaks “2”, “3”, and “4” in Figure 5.24 show this trend.

Another characteristic of the bubble coalescence theory is that the bubble coalescence effects tend to move toward the center of the bed. This aspect is supported by the spectrums shown in Figure 5.28, as the largest magnitude peaks were observed at the center of the bed.

Peaks “5” and “6” may be associated with bubble eruption. This theory is supported by Figure 5.12, which shows a smooth transition of the dominant peak to lower frequencies

with an increase in height, not the “step-changes” in frequency (e.g., peaks “2” to “3”) attributed to bubble coalescence.

Darton et al. [53] state that bubble coalescence effects should favor certain paths and radial positions in the bed, and provide examples of this in the literature. The experimental testing presented in Figures 5.26 and 5.27 has shown that certain frequency phenomena were more dominant at some radial positions than others, agreeing with the model. Furthermore, these experimental frequencies occurred at only specific frequencies and positions as they do in the model.

Pressure Fluctuation Modeling

The following section discusses the modeling of power spectrums from a bubbling fluidized bed with a second-order system. It discusses the measurement techniques (e.g., probe type) used to acquire the data, the parameters that influence the pressure fluctuations, and how certain parameters related to the modeling. In the last part of this section, a single second-order model that describes the dominant frequency’s location and magnitude in terms of the bed height is developed and compared to the experimental data.

Modeling and measurement techniques

The first section of this chapter illustrated the importance of the type of pressure probe technique used in acquiring the pressure fluctuation data and its ability to measure different power spectrum characteristics as shown in the Bode plot. As stated above, the type of probe can mask certain peaks in the power spectrum (Figure 5.7), yield different dominant peaks (Figure 5.4), not measure certain frequency peaks altogether (Figure 5.2), and yield entirely different power spectrum shapes (Figure 5.1).

After reviewing the data, the dynamic-absolute pressure probe technique was chosen for acquiring the pressure fluctuation data for the following reasons. First, the dynamic technique captured the pressure fluctuations more adequately (i.e., as measured through the signal’s variance) compared to the static technique in certain situations. As compared to the differential probe technique, the absolute probe technique captures global events in the bed,

does not cancel out or add frequencies through filtering or addition effects, and is not affected by the arbitrary choice of the distance between probe arms.

In the literature, pressure fluctuations are measured and reported at nearly all bed positions ranging from the distributor plate to the bed surface, with no position established as standard. With this in mind, the arm position was arbitrarily set at 2.5 cm below the surface.

Modeling and bed parameters

Bed height is the most well-documented bed parameter that affects the magnitude and location of the frequency peaks. As bed height is also one of the most influential parameters affecting the characteristics of the power spectrums, it was included in the model.

Fluidization velocity has a profound effect on the spectrum characteristics. Testing has shown that changing the fluidization velocity may shift the position of the peaks and switch the dominance between frequency phenomena (Figure 5.13). Because the purpose of this modeling is to provide a first step, fluidization velocity will be held constant at 27.9 cm/s (345 LPM, a velocity ratio of 1.4) while acquiring the pressure fluctuation data for the model. This velocity provided strong bubbling in the bed without slugging, as viewed visually.

Pressure fluctuation data for the model were acquired with Badger 30x50 sand. With an average particle diameter of 494 micron, this sand is classified as a Group B particle and produced a bubbling fluidized bed. Particles with smaller diameters and lower densities (Group A) were tested and not included in the model because of complexities with the power spectrums possessing first-order behavior (e.g., Figure 5.20). Particles with larger diameters and higher densities (Group D) were also tested and not included in the model because of complexities with the power spectrums possessing harmonic behavior (e.g., Figure 5.17). Neglecting the effect of particle density in the model should not effect the model's "real-world" application as sand is a very common fluidized bed media.

Pressure fluctuation data for the model were acquired at ambient temperature with air as the fluidization gas. Although temperature effects are not included in the model, data acquired at higher temperatures (Figure 5.22) suggests that the addition of this parameter into the model may be somewhat straightforward.

In summary, the second-order model was developed as a function of bed height with the probe arm position (from the surface), fluidization velocity, and particle diameter/density held constant. The pressure fluctuations were acquired at ambient temperature with the dynamic-absolute pressure probe technique. Figure 5.31 shows the fourteen experimental power spectrums used for this modeling, with a bed height range of 10.6 cm to 23.0 cm.

Modeling of the power spectrum

A single, second-order system was used to model the dominant frequency of each experimental power spectrum. The relationship between the model output and the model's natural frequency (ω_{n1}) and damping ratio (ξ_1) for this model is given in Equation 5.9.

$$\text{Model Output (dB)} = 20 \cdot \log \left(\frac{1}{1 + \frac{2 \cdot \xi_1}{\omega_{n1}} \cdot (i \cdot \omega) + \frac{(i \cdot \omega)^2}{\omega_{n1}^2}} \right) \quad (5.9)$$

The following seven steps explain the procedure used to model the dominant peak of each power spectrum shown in Figure 5.31 with a second-order system.

1. The average magnitude (dB) of the experimental power spectrum at low frequencies (below 1 Hz) was determined. This was done by taking an average of all of the data points in the given frequency range in the power spectrum.
2. The average magnitude from Step 1 was added to the experimental spectrum to produce an offset spectrum that had a magnitude of 0 dB under 1 Hz. An example of this is provided in Figure 5.32 for a bed height of 15.6 cm.
3. The model output was plotted on the offset experimental spectrum from Step 2 with the damping ratio in Equation 5.9 approximated such that the model

Experimental Operating Conditions for Figure 5.31

Bed media	Badger 30x50 Sand	Bed height	Given in figure
Mean particle diameter	494 micron	Bed mass	3300.00 ± 0.01 gm to 7200.00 ± 0.01 gm in steps of 300.00 gm
Particle density	2600 ± 100 kg/m ³	Pressure measurement	Dyn-abs
Volumetric flow	345 ± 7.5 LPM	Pressure probe position	Bed ht - 2.5 ± 0.2 cm
Velocity ratio	1.4	File group	110102f

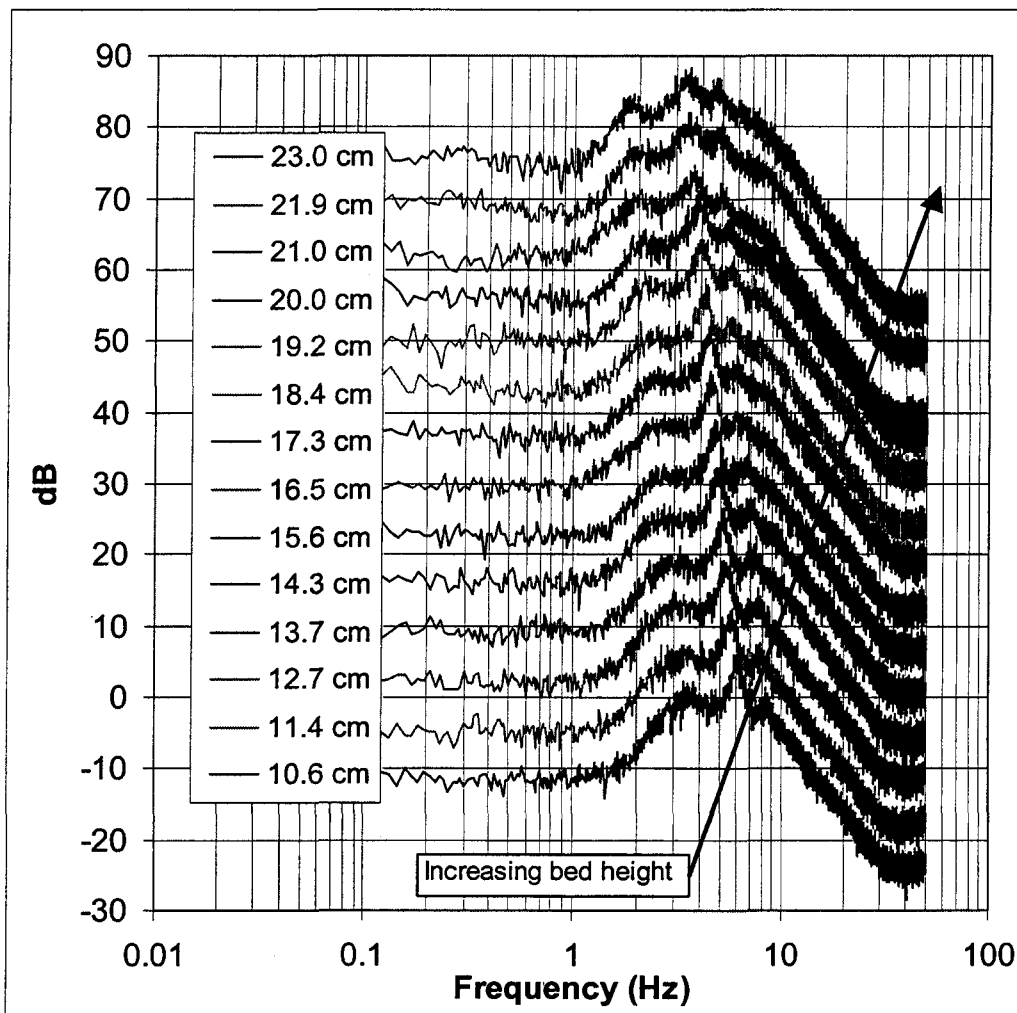


Figure 5.31: Experimental power spectra that were used in the modeling with the given test conditions

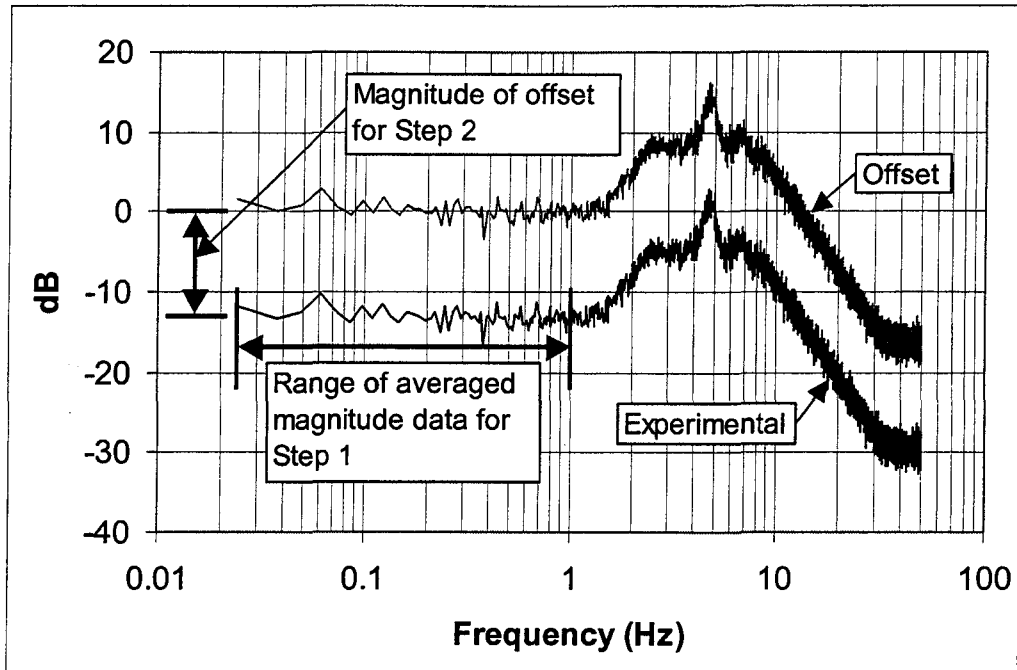


Figure 5.32: Experimental and offset power spectrums from Steps 1 and 2 of the modeling process

output yielded a magnitude (in dB) similar to the experimental spectrum's dominant peak.

4. The model's natural frequency in Equation 5.9 was set so that it aligned with the experimental spectrum's dominant frequency on the Bode plot. As determined through visual observation, the model's natural frequency could be set to the experimental dominant frequency within ± 0.1 Hz.
5. The resonant natural frequency was calculated from Equation 3.22 with the damping ratio from Step 3 and the natural frequency from Step 4.
6. To determine the magnitude of the damping ratio, the magnitude of the experimental spectrum at the modeled resonant natural frequency (Step 5) was located in the offset experimental data and averaged with the magnitudes of

the five data points before and after the experimental natural frequency. This covered a frequency range of 0.12 Hz. An example of the range of the eleven averaged points is provided in Figure 5.33 for a bed height of 15.6 cm.

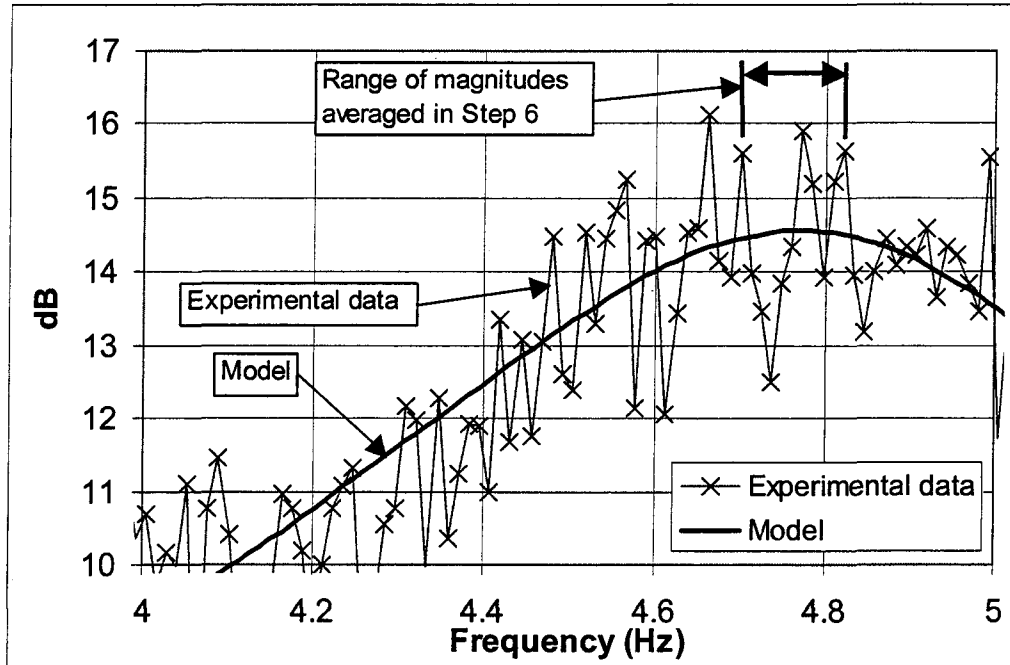


Figure 5.33: A magnified view of a power spectrum showing the range of data points used in the averaging process of Step 6

7. The model's damping ratio was determined by setting it in the Mathcad program to match the magnitude of the dominant frequency from the experimental spectrum determined in Step 6 within 0.001.

An example of the model output plotted with the experimental data is shown in Figure 5.34. The data for this experimental power spectrum were taken from a 15.6 cm bed.

This seven-step procedure was repeated for each experimental power spectrum in Figure 5.31. Table 5.2 shows the relevant information from the modeling procedure as described above. The program for this procedure is located in Appendix B with the highest bed height modeled (23.0 cm).

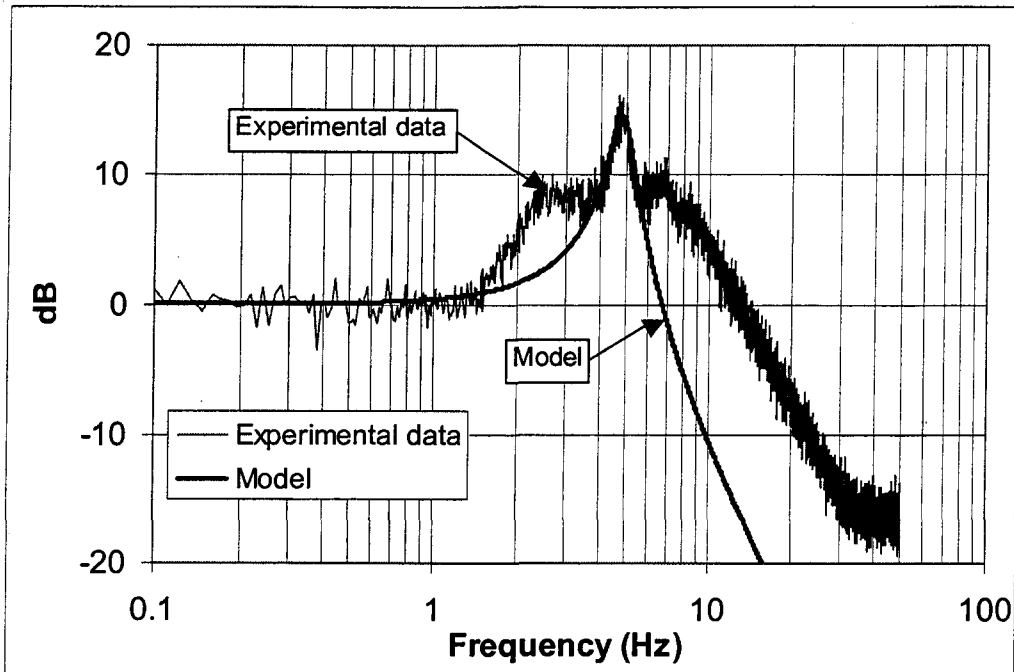


Figure 5.34: Power spectrum from a second-order, fitted system and the corresponding experimental data at a bed height of 15.6 cm

Table 5.2: Experimental data and model parameters

	Steps 1	Step 4	Step 5	Step 6	Step 7
Bed Height (cm)	Offset (dB)	Natural Frequency (Hz)	Resonant natural frequency (Hz)	Magnitude of offset peak (dB)	Damping ratio
10.6	17.57	6.1	6.067	16.59	0.074
11.4	16.79	5.7	5.662	15.38	0.085
12.7	15.82	5.4	5.361	15.56	0.084
13.7	14.75	5.2	5.162	15.63	0.083
14.3	13.80	5.0	4.962	15.17	0.087
15.6	13.20	4.8	4.756	14.51	0.094
16.5	12.35	4.6	4.555	14.04	0.100
17.3	11.22	4.5	4.457	14.75	0.092
18.4	10.42	4.3	4.240	13.01	0.113
19.2	10.00	4.1	4.049	13.04	0.112
20.0	9.66	4.0	3.942	13.16	0.111
21.0	10.15	3.8	3.714	11.34	0.137
21.9	9.00	3.6	3.517	11.36	0.136
23.0	8.79	3.5	3.433	11.31	0.137

Determination of model parameters

Figure 5.35 shows the modeled dominant frequency (Step 4) from Table 5.2 plotted against the experimental bed height. A power-curve was fitted to the data, and an equation for the natural frequency as a function of height was determined (Equation 5.10).

$$f_{n, model} = 31.95 \cdot (h)^{-0.6970} \quad (5.10)$$

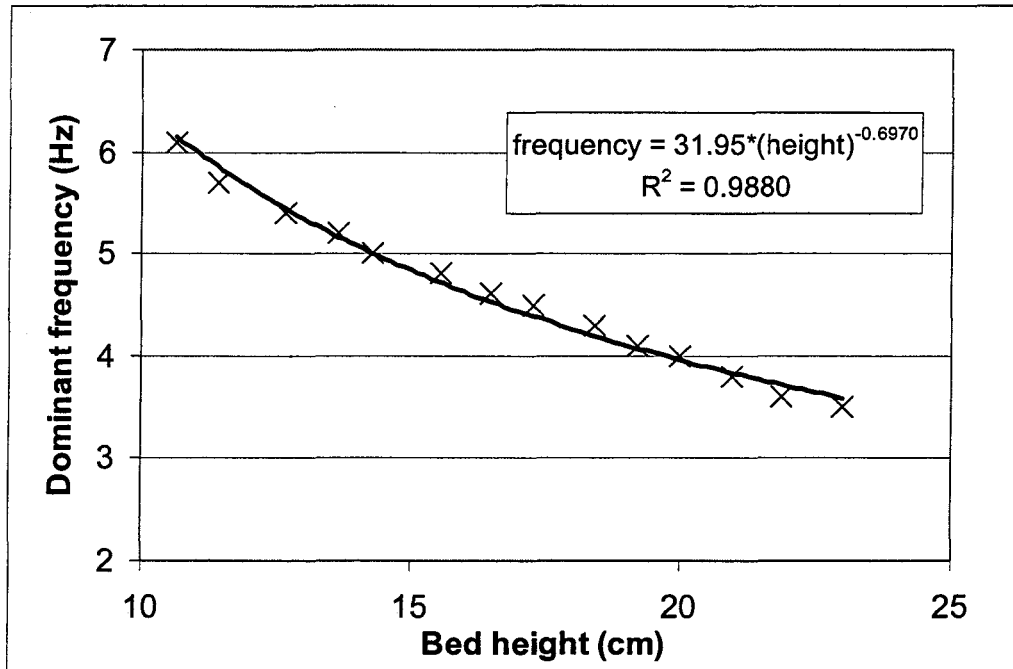


Figure 5.35: A power-curve fitted to the modeled natural frequency data listed in Table 5.2

In Equation 5.10, “ $f_{n, model}$ ” is the model’s natural frequency and “ h ” is the bed height in centimeters. The experimental value of the height exponent (-0.6970) in Equation 5.10 agrees with the experimental range reported in the literature for shallow (0.5) and deep (1.0) beds [33,43].

To determine how the experimental natural frequency shown in Equation 5.10 compares to the theoretical natural frequency derived by Hiby [33] and Brue [1] in Chapter 3, the constant C_1 from Equation 3.45 was determined for the given conditions. Using this

information, the equation for the theoretical natural frequency from Equation 3.46 was calculated in terms of bed height and is shown in Equation 5.11.

$$f_{n, theory} = 23.31 \cdot (h)^{-0.5} \quad (5.11)$$

In Equation 5.11, “ $f_{n, theory}$ ” is the theoretical natural frequency and “ h ” is the bed height in centimeters. The magnitudes of the exponent for the theoretical natural frequency (-0.5) and the experimental natural frequency (-0.6970) differ slightly, but provide the same trend of natural frequency with bed height. The constants from Equation 5.10 (“31.95”) and Equation 5.11 (“23.31”) for the experimental and theoretical frequency equations, respectively, are also in good agreement. This shows that the forcing function (i.e., the bubble phenomena related to the dominant peak) was acting on the dynamic system (i.e., fluidized bed) near its theoretical natural frequency.

Similarly, Figure 5.36 shows the modeled damping ratio (Step 7) from Table 5.2 plotted against the experimental bed height. When a power-curve was fitted to the data, an equation for the damping ratio as a function of bed height was determined (Equation 5.12).

$$\xi_{model} = 0.01124 \cdot (h)^{0.7860} \quad (5.12)$$

In Equation 5.12, “ ξ_{model} ” is the modeled damping ratio and “ h ” is the bed height in centimeters.

To determine how the experimental damping ratio shown in Equation 5.12 compares to the theoretical damping ratio derived in Chapter 3, the constant C_2 from Equation 3.57 was determined for the given conditions. Using this information, the equation for the theoretical damping ratio from Equation 3.58 was calculated in terms of bed height and is shown in Equation 5.13.

$$\xi_{theory} = 0.3070 \cdot (h)^{0.5} \quad (5.13)$$

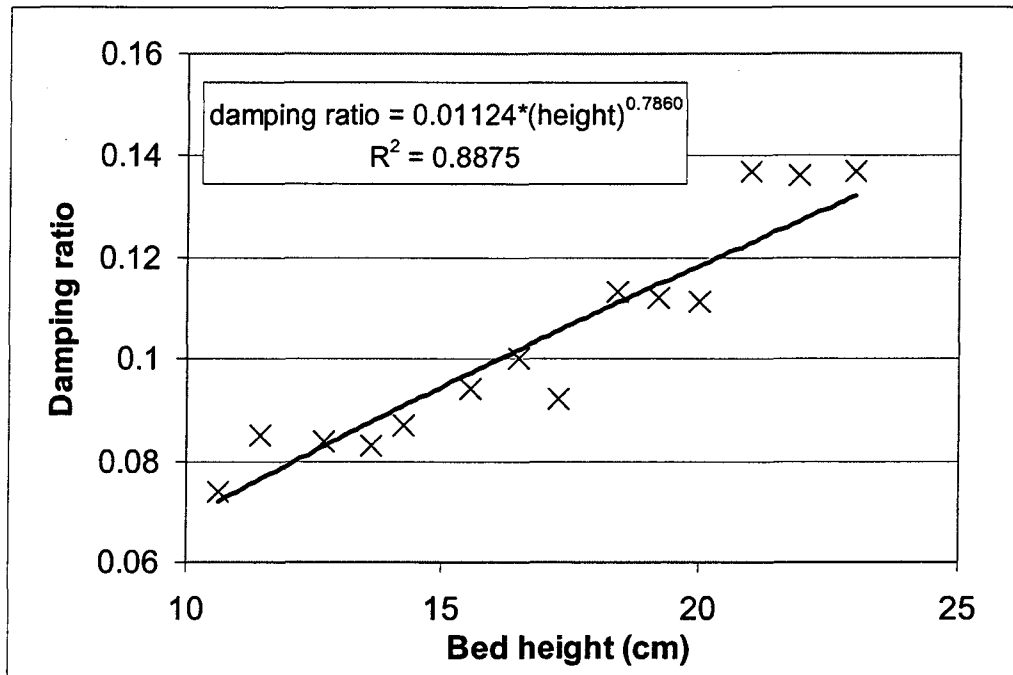


Figure 5.36: A power-curve fitted to the modeled damping ratio of Table 5.2

In Equation 5.13, “ ξ_{theory} ” is the theoretical damping ratio and “ h ” is the bed height in centimeters. The magnitudes of the exponent for the experimental damping ratio (0.7860) in Equation 5.12 and the theoretical damping ratio (0.5) in Equation 5.13 are similar and provide the same trend of damping ratio with bed height. The proportionality constants from Equation 5.12 (“0.01124”) and Equation 5.13 (“0.3070”) for the experimental and theoretical damping ratios, respectively, differ by a factor of 27. These two constants are not similar because they describe different phenomena: the experimental damping ratio is a measure of the amplitude of the forcing function (e.g., bubble phenomena), while the theoretical damping ratio describes the entire dynamic system (i.e., fluidized bed).

As shown in Figures 5.35 and 5.36, the R^2 correlation for the damping ratio (0.8875) was lower than the correlation for the natural frequency (0.9880) because the variance of the damping ratio was large compared to the variance of the dominant frequency. The main reason for the lower correlation was that the random nature of the data brought about large spikes in the power spectrums as shown in Figure 5.33. Although the experimental power spectrums were an average of 29 periodograms (15 independent periodograms), spikes were

still present. These spikes brought about a large variation in the eleven point average of the dominant frequency's magnitude in Step 6 and, in return, a large variance in the damping ratios calculated in Step 7.

A second reason for the variation in the damping ratio is associated with a change in the general shape of the power spectrum. The power spectrums of three highest beds in Figure 5.31 show that some effect has occurred with the increase in bed height as the dominant peaks in these spectrums are not as dominant to the secondary peaks compared to the dominant peaks of the other spectrums at lower bed heights. This leads to a variation between the calculated damping ratios from the above procedure between these three spectrums and the lower-height spectrums.

Determination of second-order model equation and comparison to experimental data

The natural frequency from Equation 5.10 and the damping ratio from Equation 5.12 can be substituted into equation 5.9 to yield an equation for the model output in terms of bed height (based on centimeters). This formulation is shown in Equation 5.14.

$$\text{Model Output (dB)} = 20 \cdot \log \left(\frac{1}{1 + 0.0007036 \cdot (i \cdot f) \cdot (h)^{1.483} + 0.0009796 \cdot (i \cdot f)^2 \cdot (h)^{1.394}} \right) \quad (5.14)$$

To illustrate the general trend in magnitude and dominant frequency given by the above equation, seven of the bed heights used in the power spectrums shown in Figure 5.31 were input into Equation 5.14 and the corresponding output is shown in Figure 5.37. This figure shows that the model provides a smooth transition of the dominant peak from high to low frequencies with an increase in bed height, along with a decrease in the magnitude of the dominant peak with an increase in bed height. This agrees with the experimental power spectrums of Figure 5.31.

Figure 5.38 shows the model output from Equation 5.14 plotted with the experimental power spectrum for a bed height of 10.6 cm. As observed in this figure, the model describes the dominant frequency of the experimental spectrum qualitatively well. All fourteen power spectrums shown in Figure 5.31 are shown in Appendix D with the model output from

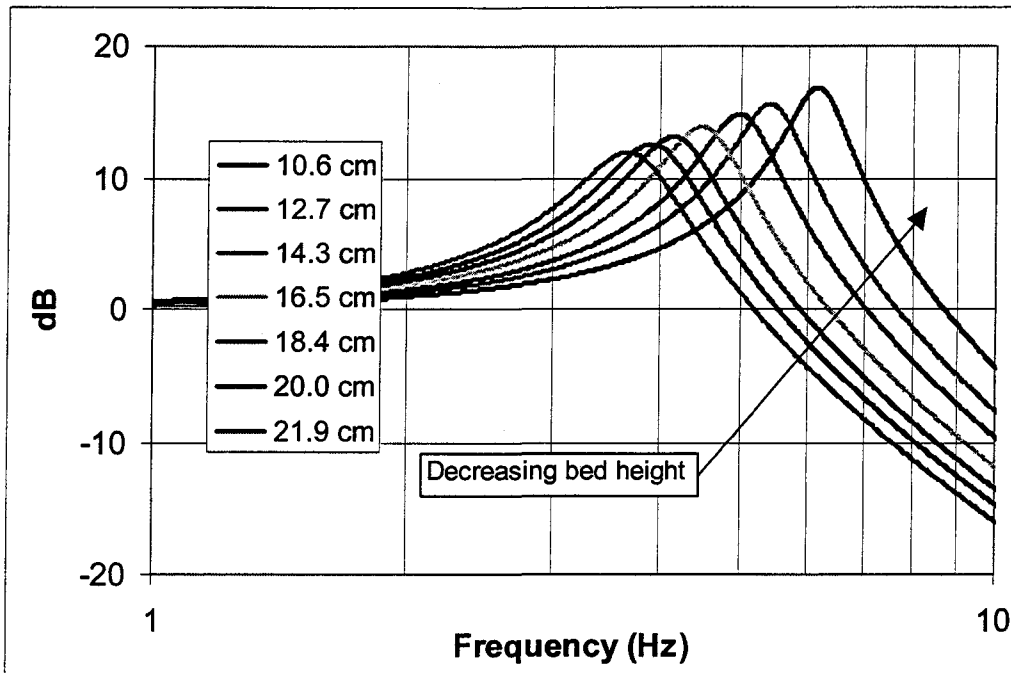


Figure 5.37: Modeled power spectrums for five bed heights using Equation 5.14

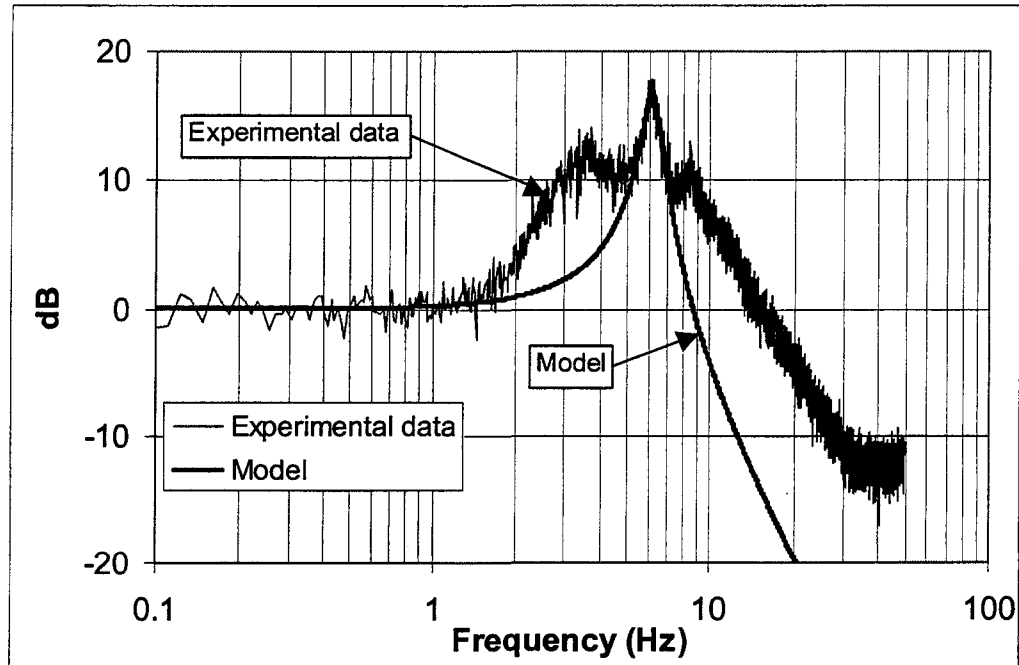


Figure 5.38: Model output from Equation 5.14 and experimental data for a bed height of 10.6 cm

Equation 5.14 using the corresponding bed height. Visual observation of these spectrums shows that Equation 5.14 adequately describes the experimental power spectrums.

To determine how well the model output describes a spectrum not used to develop Equation 5.14, the model output was compared to a power spectrum taken from an independent set of data with a bed height of 12.7 cm. This spectrum and the corresponding model output are shown in Figure 5.39. Similar to Figure 5.38, the model describes the experimental data qualitatively well.

Experimental Operating Conditions for Figure 5.39

Bed media	Badger 30x50 Sand	Bed height	12.7 ± 0.3 cm
Mean particle diameter	494 micron	Bed mass	3958.06 ± 0.01 gm
Particle density	2600 ± 100 kg/m ³	Pressure measurement	Dyn-abs
Volumetric flow	345 ± 7.5 LPM	Pressure probe position	10.2 ± 0.2 cm
Velocity ratio	1.4	File group	102802

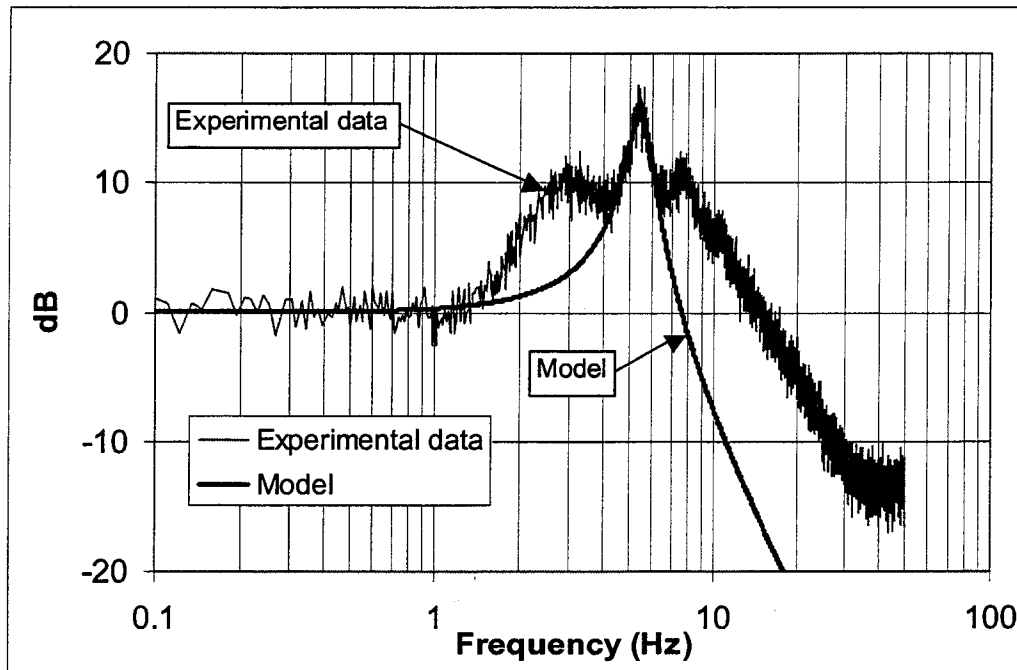


Figure 5.39: Model output from Equation 5.6 and experimental data for a bed height of 12.7 cm

CHAPTER 6. CONCLUSIONS AND RECOMMENDATIONS

Several issues associated with pressure fluctuations in a fluidized bed were examined in this research. These included the probe techniques used to acquire the pressure fluctuation data, the use of the Bode plot to better-understand the bed parameters, the extension of a bubble coalescence model to explain the frequency phenomena observed in power spectrums, and the modeling of the power spectrums with a second-order system. In the first part of this chapter, conclusions for the four main sections of this research are given along with a brief discussion. In the second part, recommendations are made to further this work.

Conclusions

Probe technique and position

Dynamic-absolute pressure probes should be used to measure pressure fluctuations in a fluidized bed, and the position of the probe arm is an important testing parameter.

- The absolute and differential pressure probe techniques yielded power spectrums that differed drastically in several cases. This difference arises from the fact that the absolute technique measures the pressure at only one position in the bed while the differential technique measures difference in pressure at two positions. The choice of spacing between the two differential probe arms is also arbitrary. Because of this spacing issue and the complexities of measuring pressure fluctuations at two positions in the bed, differential pressure probes should be used with caution.
- The static and dynamic pressure probe techniques yielded power spectrums that were similar in most cases. Small differences in the magnitudes of the power spectrums were observed in some situations, and

these differences were attributed to the edge effects from the bottom of the probe tip.

- The location and magnitude of the dominant and secondary peaks were shown to vary drastically with axial and radial position in the bed.

Power spectrum characteristics

The Bode plot is a very useful technique in studying the power spectrums from fluidized beds. It offers a new perspective on fluidized beds as dynamic systems.

- The shifting of the dominant peak with changes in bed height that was observed in this research agreed with the trend presented in the literature [1,30]. A secondary peak that was not a function of bed height was also observed, which has not been presented in the literature.
- The power spectrums acquired with fluidization velocity testing showed the growth of dominant and secondary peaks as a dynamic system. The use of the Bode plot may provide further insight into the physical phenomena associated with each parameter.
- Harmonics were present in the power spectrum of beds that operated with Group D particles and were attributed to the pressure data having a square-wave appearance in the time domain. With sand and glass beads used as the bed media, visual observation showed that slugs were present at the surface of the bed. Harmonics were also observed with steel particles. Although slugging was not visually observed in the bed with steel particles, the pressure data had a square-wave appearance in the time domain.

- First-order characteristics were present in the power spectrum with Group A particles. This phenomena is not well-understood, but may be a characteristic of Group A particles.
- The power spectrums acquired with bed temperature testing showed that bed temperature had little effect on the power spectrums for the given range of fluidization velocities. The use of the Bode plot may provide further insight into the physical phenomena associated with each parameter.

Multiple-peak phenomena

Multiple-peak phenomena observed in the power spectrums were linked to bubble phenomena and jetting effects at the distributor.

- Testing at different probe arm positions (axial and radial) showed that at least six different frequency peaks occurred in a power spectrum. A bubble coalescence model was extended to explain the occurrence of several of these peaks. Some tests suggested that the dominant and secondary peaks were associated with bubble eruption at the surface. High-frequency, low-amplitude pressure phenomena were linked to jetting effects at the distributor.

Pressure fluctuation modeling

A second-order system was shown to model the dominant frequency of power spectrums qualitatively well.

- A second-order model was developed that modeled the dominant frequency across a height range of 10.6 cm to 23.0 cm. The model is a first step in an improvement over equations that only predict the location in that it describes not only the location, but also the magnitude of the

dominant frequency. Further models that include multiple-peak phenomena could then show when one peak phenomena is dominant over another by comparing these magnitudes.

- An equation for the natural frequency that was determined from experimental data agreed with the trends provided by theoretical derivation and experimental data in the literature.
- An equation for the damping ratio was determined from experimental data, and its trend agreed with the theoretical derivation developed in this research.

Recommendations

- The magnitude of peaks in the power spectrum were shown to change in magnitude across the axis of the bed. With this magnitude change, dominant peaks were shown to become secondary, and secondary peaks were shown to become dominant. As dominant peaks from power spectrums are often used to validate if similitude is reached between two different cases, the effect of axial position should be further studied.
- Under certain operating conditions, testing has shown that the dominant peak is a function of bed height while the secondary peak is not. If the entire power spectrum for each similitude case is used to validate if similitude is reached, this may causes issues if the two cases have different bed heights as scaling between the two cases may cause one peak to move while the other remains constant.

- The presence of harmonics in the power spectrums should be further studied to determine the differences between Group B and Group D particles. This presence may be used as a criteria for determining the type of bed behavior under the given operating conditions. The influence of bed diameter on harmonics should also be studied, as this parameter has been shown to influence slugging. Testing of Group D particles at various radial and axial locations should be performed and compared to those for Group B particles to determine and understand any fundamental differences.
- Group A particles should be further studied to understand the reason that they exhibit first-order characteristics. This further research may show that the transition between Group A and Group B particles can be characterized by a shifting from first-order characteristics to second-order characteristics. Testing of Group A particles at various radial and axial locations should be performed and compared to those for Group B particles to determine and understand any fundamental differences.
- The effect of bed temperature on the power spectrums is still not a well-understood phenomena. Testing at high temperature with different bed heights, fluidization velocities, and probe locations may help explain the odd trends shown in the literature [20].
- Graphing techniques such as 3-D mapping that are able to show both the axial and radial positions in the bed height simultaneously should be examined to understand the structure of the frequency phenomena in the bed.

- Visual observation of a “see-through” 2-D bed should be performed to better understand the link between the frequency phenomena and the bubble coalescence model.
- Methods of determining the magnitude and location of dominant and secondary peaks quantitatively should be examined to use these quantities in modeling. These methods may include Auto-Regressive, Moving-Average (ARMA) models [68], Prony analysis [69], or Loop-shaping [70].
- Effects such as axial location in the bed, fluidization velocity, and bed temperature should be added to the model to increase its ability to describe the power spectrums. Multiple-peak phenomena should also be introduced into the model through second-order systems acting in parallel. Each of the peaks in the model should be correlated to bed parameters to predict when one peak is dominant over another.
- The initial results from the CFD modeling of pressure fluctuations using MFIX code was presented in this research and shown to possess characteristics (multiple-peak phenomena, second-order slope) similar to the experimental power spectrums. Further MFIX testing should be performed to determine if the model can describe the pressure fluctuation data adequately.
- The pressure fluctuation measurement and analysis techniques presented in this research should be used to study the frequency phenomena in liquid-fluidized beds. This may provide insight into the mechanisms affecting the frequency phenomena in both liquid-fluidized and gas-fluidized beds.

REFERENCES

- [1] Brue, E. "Pressure fluctuations as a diagnostic tool for fluidized beds." Ph.D. Dissertation, Iowa State University, Ames, 1994.
- [2] Brue, E. and Brown, R.C. "Use of pressure fluctuations to validate hydrodynamic similitude in fluidized media: bubbling beds." *Powder Technology* 2001, 119, 117-127.
- [3] Nicastro, M.T. and Glicksman, L.R. "Experimental verification of scaling relationships for fluidized beds." *Chemical Engineering Science* 1984, 19(9), 1381-1391.
- [4] Glicksman, L.R., Hyre, M.R. and Farrell, P.A. "Dynamic similarity in fluidization." *Int. J. Multiphase Flow* 1994, 20, 331-386.
- [5] Davidson, J.F. "The two-phase theory of fluidization: successes and opportunities." *AIChE Symposium Series: Advances in Fluidized Systems* 1991, 1-12.
- [6] Zukowski, W. "The pressure pulses generated by the combustion of natural gas in bubbling fluidized beds." *Combustion and Flame* 2002, 130, 15-26.
- [7] Schouten, J.C. and van den Bleek, C.M. "Monitoring the quality of fluidization using the short-term predictability of pressure fluctuations." *AIChE Journal* January 1998, 44(1), 48-60.
- [8] Trnka, O., Vesely, V. and Hartman, M. "Identification of the state of a fluidized bed by pressure fluctuations." *AIChE Journal* March 2000, 46(3), 509-514.

- [9] Bai, D., Shibuya, E., Nakagawa, N. and Kato, K. "Characterization of gas fluidization regimes using pressure fluctuations." *Powder Technology* 1996, 87, 105-111.
- [10] Fan, L.S., Satija, S. and Wisecarver, K. "Pressure fluctuation measurements and flow regime transitions in gas-liquid-solid fluidized beds." *AIChE Journal* February 1986, 32(2), 338-340.
- [11] Brue, E. "Process model identification of circulating fluidized bed hydrodynamics." M.S. Thesis, Iowa State University, Ames, 1994.
- [12] Brown, R.C. and Brue, E. "Resolving dynamical features of fluidized beds from pressure fluctuations." *Powder Technology* 2001, 119, 68-80.
- [13] Kunni, D. and Levenspiel, O. Fluidization Engineering; Butterworth-Heinemann: Boston, 1991.
- [14] Geldart, D. "Characterization of fluidized powders." In *Gas Fluidization Technology*; D. Geldart, Ed; John Wiley & Sons: Chichester, 1980; 1-52.
- [15] Yates, J.G. and Simons, S.J.R. "Experimental methods in fluidization research." *Int. J. Multiphase Flow* 1994, 20, 297-330.
- [16] Rowe, P.N. and Masson, H. "Interaction of bubbles with probes in gas fluidized beds." *Trans IChemE* 1981, 59, 177-185.
- [17] Lirag, R.C. Jr., and Littman, H. "Statistical study of the pressure fluctuations in a fluidized bed." *Fluidization: AIChE Symposium Series*, H. Littman and R. Pfeffer, Eds. *AIChE J.* 1971, 67(116), 11-22.

- [18] Wong, H.W. and Baird, H.I. "Fluidisation in a pulsed gas flow." *The Chemical Engineering Journal* 1971, 2, 104-113.
- [19] Kage, H., Iwasaki, N. and Matsuno, Y. "Frequency analysis of pressure fluctuations in plenum as a diagnostic method for fluidized beds." In *Fluid-Particle Processes, AIChE Symposium Series*. A.W. Weimer, Ed.; AIChE: New York, 1993.
- [20] Fan, L.T., Huang, Y.W., Neogi, D. and Yutani, N. "Statistical analysis of temperature effects on pressure fluctuations in a gas-solid fluidized bed." *Fluidization '85* 1985, 37-50.
- [21] Clark, N.N. and Atkinson, C.M. "Amplitude reduction and phase lag in fluidized bed pressure measurements." *Chemical Engineering Science* 1988, 43 (7), 1547-1557.
- [22] Svoboda, K., Cermak, J., Hartman, M., Drahos, J., and Selucky, K. "Pressure fluctuations in gas-fluidized beds at elevated temperatures." *Ind Eng, Chem. Process Des. Dev.* 1983, 22, 514-520.
- [23] Botterill, J.S.M., and Hawkes, G.D. "Apparent change in heat transfer mechanism and corresponding bed behavior with change in operating temperature." *Fluidization V* 1986, 393-400.
- [24] Dent, D., LaNauze, R.D., Joyce, T., Fulford, V., and Peeler, P. "Differential pressure measurements – their application to measurement of fluidized bed combustion parameters." *10th Int. Conf. On Fluidized Bed Combustion* 1989, 451-456.
- [25] Roy, R. and Davidson, J.F. "Similarity between gas-fluidized beds at elevated temperature and pressure." *Fluidization VI* 1989, 293-300.

- [26] Bi, H.T., Grace, J.R., and Zhu, J. "Propagation of pressure waves and forced oscillations in gas-solid fluidized beds and their influence on diagnostics of local hydrodynamics." *Powder Technology* 1995, 82, 239-253.
- [27] Sitnai, O., Dent, D.C. and Whitehead, A.B. "Preliminary communication: bubble measurement in gas-solid fluidized beds." *Chemical Engineering Science* 1981, 36(9), 1583.
- [28] Dhodapkar, S.V. and Klinzing, G.E. "Pressure fluctuation analysis for a fluidized bed." In *Fluid-Particle Processes, AIChE Symposium Series*. A.W. Weimer, Ed.; AIChE: New York, 1993.
- [29] Fan, L.T., Ho, T.C., Hiraoka, S. and Walawender, W.P. "Pressure fluctuations in a fluidized bed." *AIChE J.* 1981, 27(3), 388-396.
- [30] Van der Schaaf, J., J.C. Schouten, Johnsson, F. and van den Bleek, C.M. "Multiples modes of bed mass oscillation in gas-solids fluidized beds." *ASME: Proceedings of the 15th International Conference on Fluidized Bed Combustion* 1999, Paper No. FBC99-0201.
- [31] Musmarra, D., Poletto, M., Vaccaro, S., and Clift, R. "Dynamic waves in fluidized beds." *Powder Technology* 1995, 82, 255-268.
- [32] Tamarin, A.I. "The origin of self-excited oscillations in fluidized beds." *International Chemical Engineering* 1964, 4(1), 50-54.
- [33] Hiby, J.W. "Periodic phenomena connected with gas-solid fluidization." In *Proceedings of the International Symposium on Fluidization, Eindhoven*; Netherlands University Press: Amsterdam, 1967; 99.

- [34] Kang, W.K., Sutherland, J.P. and Osberg, G. L. "Pressure fluctuations in a fluidized bed with and without screen cylindrical packings." *Ind. Eng. Chem. Fundamentals* 1967, 6(4), 499-504.
- [35] Clark, N.N., McKenzie, E.A., Jr., and Gautam, M. "Differential pressure measurements in a slugging fluidized bed." *Powder Technology* 1991, 67, 187-199.
- [36] Darcy, H. Les Fontaines Publiques de la Ville de Dijon; Victor Dalmon; Paris, 1856.
- [37] Ergun, S. "Fluid flow through packed columns." *Chem. Eng. Prog.* 1952, 48(2), 89-94.
- [38] Baskakov, A.P., Tuonogov, V.G. and Filippovsky, N.F. "A study of pressure fluctuations in a bubbling fluidised bed." *Powder Technology* 1986, 45, 113-117.
- [39] Sun, J., Chen, M.M., and Chao, B.T. "On the fluctuation motions due to surface waves in gas fluidized beds." In *Proceedings of the First World Conference on Experimental Heat Transfer, Fluid Mechanics and Thermodynamics, Dubrovnik*. R.K. Shah, E.N. Ganic, and K.T. Yang, Eds.; Elsevier: New York, 1988; 1310.
- [40] Sun, J., Chen, M.M., and Chao, B.T. "Modeling of solids global fluctuations in bubbling fluidized beds by standing surface waves." *Int. J. Multiphase Flow* 1994, 20, 315-338.
- [41] Bi, H.T. and Grace, J.R. "Comment on 'Modeling of solids global fluctuations in bubbling fluidized bed by standing waves' by Sun et al. (1994)" *Int. J. Multiphase Flow* 1996, 22(1), 203-205.

- [42] Sadasivan, S., Barreteau, D., and LaGuerie, C. "Studies on frequency and magnitude of fluctuations of pressure drop in gas-solid fluidized beds." *Powder Technology* 1980, 26, 67-74.
- [43] Verloop, J. and Heertjes, P.M. "Periodic pressure fluctuations in fluidized beds." *Chem. Eng. Science* 1974, 29, 1035-1042.
- [44] Baeyens, J., and Geldart, D. "An investigation into slugging fluidised beds." *Chem. Engng. Sci.* 1974, 29, 255-265.
- [45] Roy, R., Davidson, J.F. and Tuponogov, V.G. "The velocity of sound in fluidized beds." *Chem. Eng. Sci.* 1990, 45(11), 3233-3245.
- [46] Fan, L.T., Ho, T.C. and Walawender, W.P. "Measurements of the rise velocities of bubbles, slugs, and pressure waves in a gas-solid fluidized bed using pressure fluctuation signals." *AIChE J.* 1983, 29(1), 33-39.
- [47] Leva, M., Weintaub, M., Grummer, M., Pollchik, M., and Storch, H. *U.S. Bureau of Mines Bulletin 504* 1951.
- [48] Otake, T., Tone, S., Kawashima, M., and Shibata, T. "Behavior of rising bubbles in a gas-fluidized bed at elevated temperature." *Journal of Chemical Engineering of Japan* 1975, 8(5), 388-392.
- [49] Mii, T, Yoshida, K., and Kunii, D. "Temperature-effects on the characteristics of fluidized beds." *Journal of Chemical Engineering of Japan* 1973, 6(1), 100-102.
- [50] Kai, T. and Furusaki, S. "Behavior of fluidized beds of small particles at elevated temperatures." *Journal of Chemical Engineering of Japan* 1985, 18(2), 113-118.

- [51] Svensson, A., Johnsson, F. and Leckner, B. "Fluidization regimes in non-slugging fluidized beds: the influence of pressure drop across the air distributor." *Powder Technology* 1996, 86, 299-312.
- [52] Davidson, J.F. and Harrison, D. Fluidized Particles; Cambridge Univ. Press.: New York, 1963.
- [53] Darton, R.C., LaNauze, R.D., Davidson, J.F. and Harrison, D. "Bubble growth due to coalescence in fluidized beds." *Trans. I. Chem. E.* 1977, 55, 274-279.
- [54] Geldart, D. *Powder Technology* 1968, 1, 355.
- [55] Van der Schaaf, J., Schouten, J.C. and van den Bleek, C.M. "Origin, propagation and attenuation of pressure waves in gas-solid fluidized beds." *Powder Technology* 1998, 95, 220-233.
- [56] Van der Schaaf, J., Schouten, J.C. and van den Bleek, C.M. "Experimental observation of pressure waves in gas-solds fluidized beds." *AIChE Symposium Series: Fluidization and Fluid Particle Systems* 1998, 94(318), 48-52.
- [57] Rao, S.S. Mechanical Vibrations, 2nd Ed; Addison-Wesley Publishing Company: New York, 1990.
- [58] Brown, R.G. and Hwang, P.Y.C. Introduction to Random Signals and Applied Kalman Filtering, 3rd Ed; John Wiley & Sons: New York, 1997.
- [59] Lynn, P.A. An Introduction to the Analysis and Processing of Signals, 3rd Ed.; Macmillan Press: Hong Kong, 1989.

- [60] Komo, J.J. Random Signal Analysis in Engineering Systems; Academic Press Inc.: Orlando, 1987.
- [61] Thomson, W.T., and Dahleh, M.D. Theory of Vibration with Applications, 5th Ed.; Prentice Hall: New Jersey, 1998.
- [62] Ogata, K. Modern Control Engineering, 2nd Ed; Prentice Hall: New Jersey, 1990.
- [63] Smith, C.A. and Corripio, A.B. Principles and Practice of Automatic Process Control; John Wiley & Sons: New York, 1985.
- [64] Geldart, D. and Xie, H.Y. "The response time of pressure probes." *Powder Technology* 1997, 90, 149-151.
- [65] Fan, L.T., Huang, Y.W. and Yutani, N. "Determination of the lower bound minimum fluidization velocity: application at elevated temperatures." *Chemical Engineering Science* 1986, 41(1), 189-192.
- [66] Brown, R.C. Personal communication. May 14th, 2002.
- [67] Battaglia, F. Personal communication. July 23rd, 2002.
- [68] Marple, S.L. Digital Spectral Analysis with Applications; Prentice Hall: New Jersey, 1987.
- [69] Kommareddy, M.A. "Prony Analysis: A Tool for Modal Identification in Power Systems." M.S. Thesis, Iowa State University, Ames, 1994.
- [70] Vinnicombe, G. Uncertainty and Feedback; Imperial College Press: London, 2001.

APPENDIX A. BADGER SAND SIEVE ANALYSIS

Table A.1: 16x30 Ind

Mesh	Range (micron)	Average diameter	% retained	(x/dp)l
16	> 1180	1290	0.2	0.000155
20	> 850	1015	48.0	0.047291
25	> 710	780	49.6	0.063590
30	> 600	655	1.9	0.002901
40	> 425	512.5	0.3	0.000585
Pan		212.5	0.0	0.000000

16x30 Ind mean diameter = 878 micron

Table A.2: 30x50 Ind

Mesh	Range (micron)	Average diameter	% retained	(x/dp)l
30	> 600	655	2.1	0.003206
35	> 500	550	39.7	0.072182
40	> 425	462.5	48.9	0.105730
50	> 300	362.5	8.9	0.024552
70	> 212	256	0.3	0.001172
Pan		106	0.1	0.000943

30x50 Ind mean diameter = 494 micron

APPENDIX B. MATHCAD ANALYSIS PROGRAM

BFB Pressure Fluctuation Analysis Program
Dave Falkowski (w/ Ethan Brue) - ISU - Fall 2001
 (Use in connection w/ DIS5.vi data acquisition program)

Reading Experimental Data:

aa := READPRN(bedpres)

sfreq := 100

i := 0.. 122999

Calculate average pressure:

$$\text{avepress} := \frac{\sum_i aa_i}{123000} \quad \text{avepress} = 2.5192 \quad \sigma := \text{stdev}(aa) \quad \sigma = 0.3681$$

$$a_i := aa_i - \text{avepress}$$

Divide data set into 29 segments of 8192 data points: j := 0.. 8191 n := 4096

$$a1_j := a_{(j+0 \cdot n)} \quad a5_j := a_{(j+4 \cdot n)} \quad a9_j := a_{(j+8 \cdot n)} \quad a13_j := a_{(j+12 \cdot n)} \quad a17_j := a_{(j+16 \cdot n)} \quad a21_j := a_{(j+20 \cdot n)}$$

$$a2_j := a_{(j+1 \cdot n)} \quad a6_j := a_{(j+5 \cdot n)} \quad a10_j := a_{(j+9 \cdot n)} \quad a14_j := a_{(j+13 \cdot n)} \quad a18_j := a_{(j+17 \cdot n)} \quad a22_j := a_{(j+21 \cdot n)}$$

$$a3_j := a_{(j+2 \cdot n)} \quad a7_j := a_{(j+6 \cdot n)} \quad a11_j := a_{(j+10 \cdot n)} \quad a15_j := a_{(j+14 \cdot n)} \quad a19_j := a_{(j+18 \cdot n)} \quad a23_j := a_{(j+22 \cdot n)}$$

$$a4_j := a_{(j+3 \cdot n)} \quad a8_j := a_{(j+7 \cdot n)} \quad a12_j := a_{(j+11 \cdot n)} \quad a16_j := a_{(j+15 \cdot n)} \quad a20_j := a_{(j+19 \cdot n)} \quad a24_j := a_{(j+23 \cdot n)}$$

$$a25_j := a_{(j+24 \cdot n)} \quad a26_j := a_{(j+25 \cdot n)} \quad a27_j := a_{(j+26 \cdot n)} \quad a28_j := a_{(j+27 \cdot n)} \quad a29_j := a_{(j+28 \cdot n)}$$

Take the fft of each segment:

$$\begin{aligned} b1 &:= \text{fft}(a1) & b6 &:= \text{fft}(a6) & b11 &:= \text{fft}(a11) & b16 &:= \text{fft}(a16) & b21 &:= \text{fft}(a21) & b26 &:= \text{fft}(a26) \\ b2 &:= \text{fft}(a2) & b7 &:= \text{fft}(a7) & b12 &:= \text{fft}(a12) & b17 &:= \text{fft}(a17) & b22 &:= \text{fft}(a22) & b27 &:= \text{fft}(a27) \\ b3 &:= \text{fft}(a3) & b8 &:= \text{fft}(a8) & b13 &:= \text{fft}(a13) & b18 &:= \text{fft}(a18) & b23 &:= \text{fft}(a23) & b28 &:= \text{fft}(a28) \\ b4 &:= \text{fft}(a4) & b9 &:= \text{fft}(a9) & b14 &:= \text{fft}(a14) & b19 &:= \text{fft}(a19) & b24 &:= \text{fft}(a24) & b29 &:= \text{fft}(a29) \\ b5 &:= \text{fft}(a5) & b10 &:= \text{fft}(a10) & b15 &:= \text{fft}(a15) & b20 &:= \text{fft}(a20) & b25 &:= \text{fft}(a25) \end{aligned}$$

Calculate Power Spectral Density of each segment: k := 0.. 4096

$$p1_k := b1_k \cdot \overline{b1_k} \quad p6_k := b6_k \cdot \overline{b6_k} \quad p11_k := b11_k \cdot \overline{b11_k} \quad p16_k := b16_k \cdot \overline{b16_k} \quad p21_k := b21_k \cdot \overline{b21_k} \quad p26_k := b26_k \cdot \overline{b26_k}$$

$$p2_k := b2_k \cdot \overline{b2_k} \quad p7_k := b7_k \cdot \overline{b7_k} \quad p12_k := b12_k \cdot \overline{b12_k} \quad p17_k := b17_k \cdot \overline{b17_k} \quad p22_k := b22_k \cdot \overline{b22_k} \quad p27_k := b27_k \cdot \overline{b27_k}$$

$$p3_k := b3_k \cdot \overline{b3_k} \quad p8_k := b8_k \cdot \overline{b8_k} \quad p13_k := b13_k \cdot \overline{b13_k} \quad p18_k := b18_k \cdot \overline{b18_k} \quad p23_k := b23_k \cdot \overline{b23_k} \quad p28_k := b28_k \cdot \overline{b28_k}$$

$$p4_k := b4_k \cdot \overline{b4_k} \quad p9_k := b9_k \cdot \overline{b9_k} \quad p14_k := b14_k \cdot \overline{b14_k} \quad p19_k := b19_k \cdot \overline{b19_k} \quad p24_k := b24_k \cdot \overline{b24_k} \quad p29_k := b29_k \cdot \overline{b29_k}$$

$$p5_k := b5_k \cdot \overline{b5_k} \quad p10_k := b10_k \cdot \overline{b10_k} \quad p15_k := b15_k \cdot \overline{b15_k} \quad p20_k := b20_k \cdot \overline{b20_k} \quad p25_k := b25_k \cdot \overline{b25_k}$$

Find the average PSD function:

$$\text{sum1}_k := p1_k + p2_k + p3_k + p4_k + p5_k + p6_k + p7_k + p8_k + p9_k + p10_k + p11_k + p12_k + p13_k + p14_k + p15_k$$

$$\text{sum2}_k := p16_k + p17_k + p18_k + p19_k + p20_k + p21_k + p22_k + p23_k + p24_k + p25_k + p26_k + p27_k + p28_k + p29_k$$

$$\text{PSD}_k := \frac{\text{sum1}_k + \text{sum2}_k}{29}$$

$$\text{Hz}_k := \frac{k}{4096} \cdot \frac{\text{sfreq}}{2} \quad \text{freq}_k := \text{Hz}_k \cdot 2 \cdot \pi$$

n := 1..4095

bedpres ≡ "C:\FALK\DATA\110102\110102f15.PF

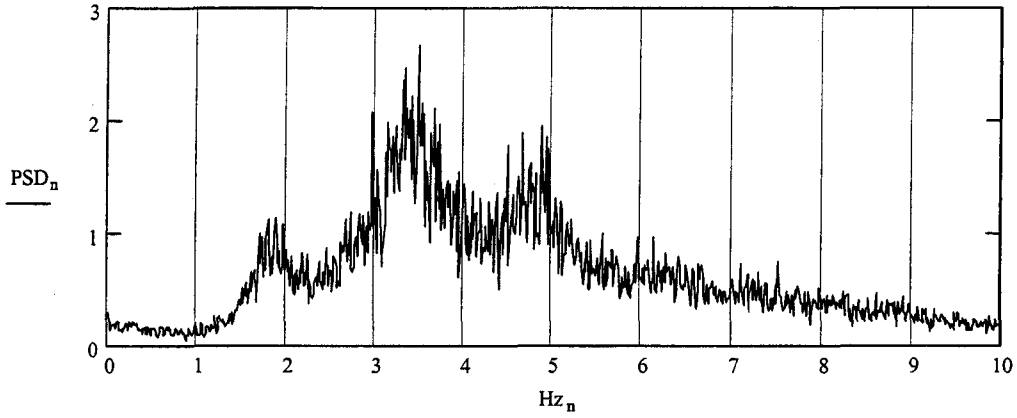
Calculate system Bode plot: $dB1_k := 10 \cdot \log(PSD_k)$

sfreq = 100

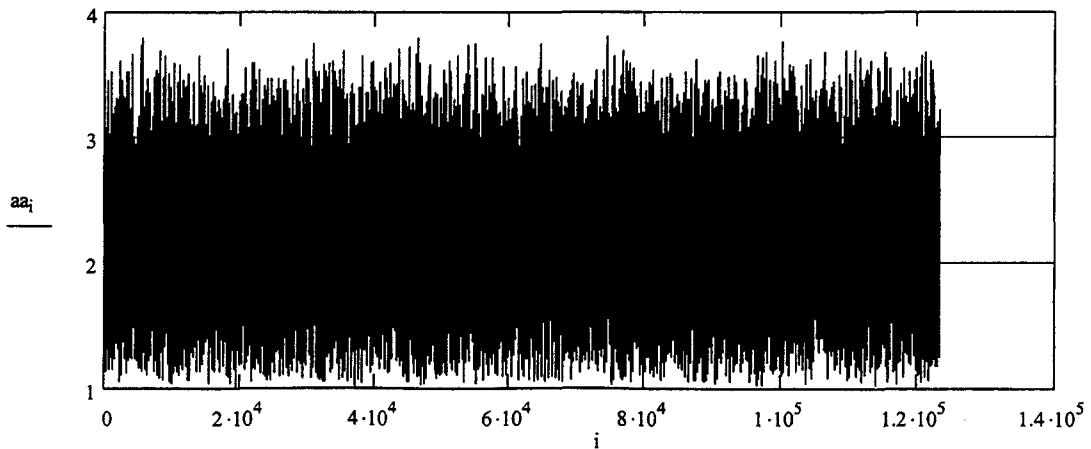
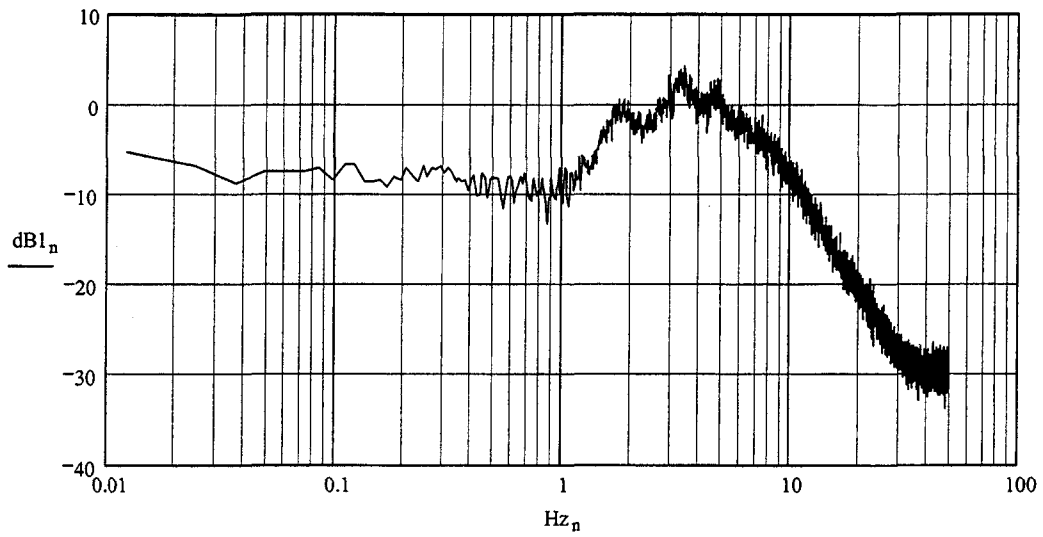
avepress = 2.519

$\sigma = 0.368$

PSD OF BFB PRESSURE FLUCTUATIONS



BODE PLOT OF BFB PRESSURE FLUCTUATIONS



sfreq := 100

k := 0..4096

j := 0..8191

dboffset := 8.79

$$Hz_z_k := \left(\frac{k}{4096} \right) \cdot \frac{sfreq}{2}$$

i := $\sqrt{-1}$

$$dB2_k := (dB1_k + dboffset)$$

num1 := 1

Hz1 := 3.5

gam1 := .137

bedpres = "C:\FALK\DATA\110102\110102f15.PRN"

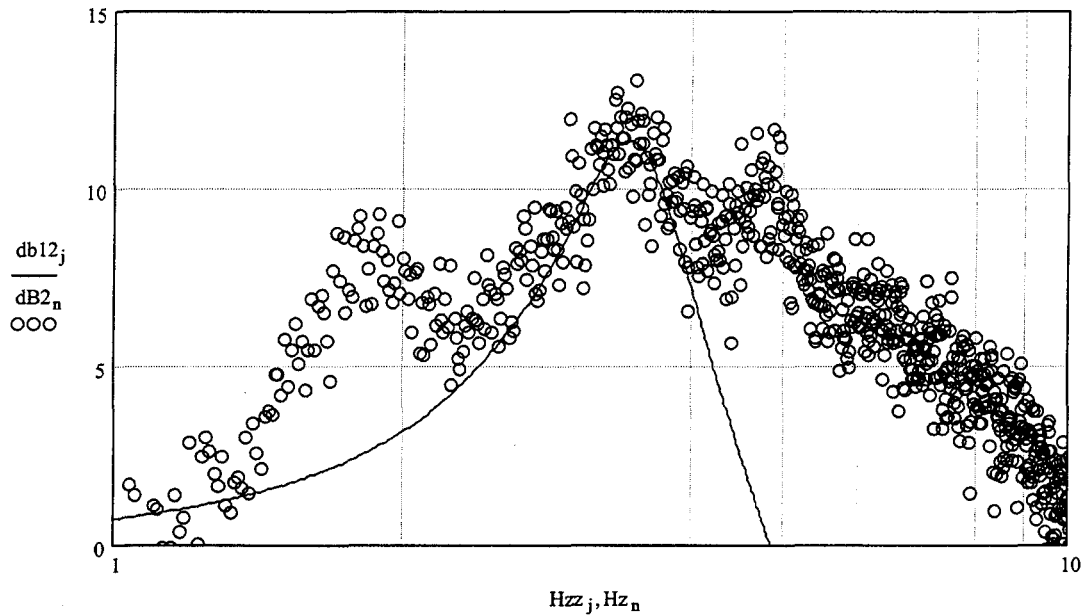
$$db12_k := \left[\text{Re} \left[20 \log \left[\frac{\text{num1}}{1 + 2 \cdot i \cdot \text{gam1} \cdot \frac{Hz_z_k}{Hz1} + \left(\frac{i \cdot Hz_z_k}{Hz1} \right)^2} + 0 \right] \right] \right]$$

peakraw := 2.52

numtomatch := peakraw + dboffset

numtomatch = 11.31

max(db12) = 11.327



**APPENDIX C. POWER SPECTRUMS AT SIX BED HEIGHTS
WITH DIFFERENT PROBE ARM POSITIONS**

Experimental Operating Conditions for Figure C.1

Bed media	Badger 30x50 Sand	Bed height	8.6 ± 0.3 cm
Mean particle diameter	494 micron	Bed mass	2638.71 ± 0.01 gm
Particle density	2600 ± 100 kg/m ³	Pressure measurement	Dyn-abs
Volumetric flow	345 ± 7.5 LPM	Pressure probe position	Given in figure
Velocity ratio	1.4	File group	100902

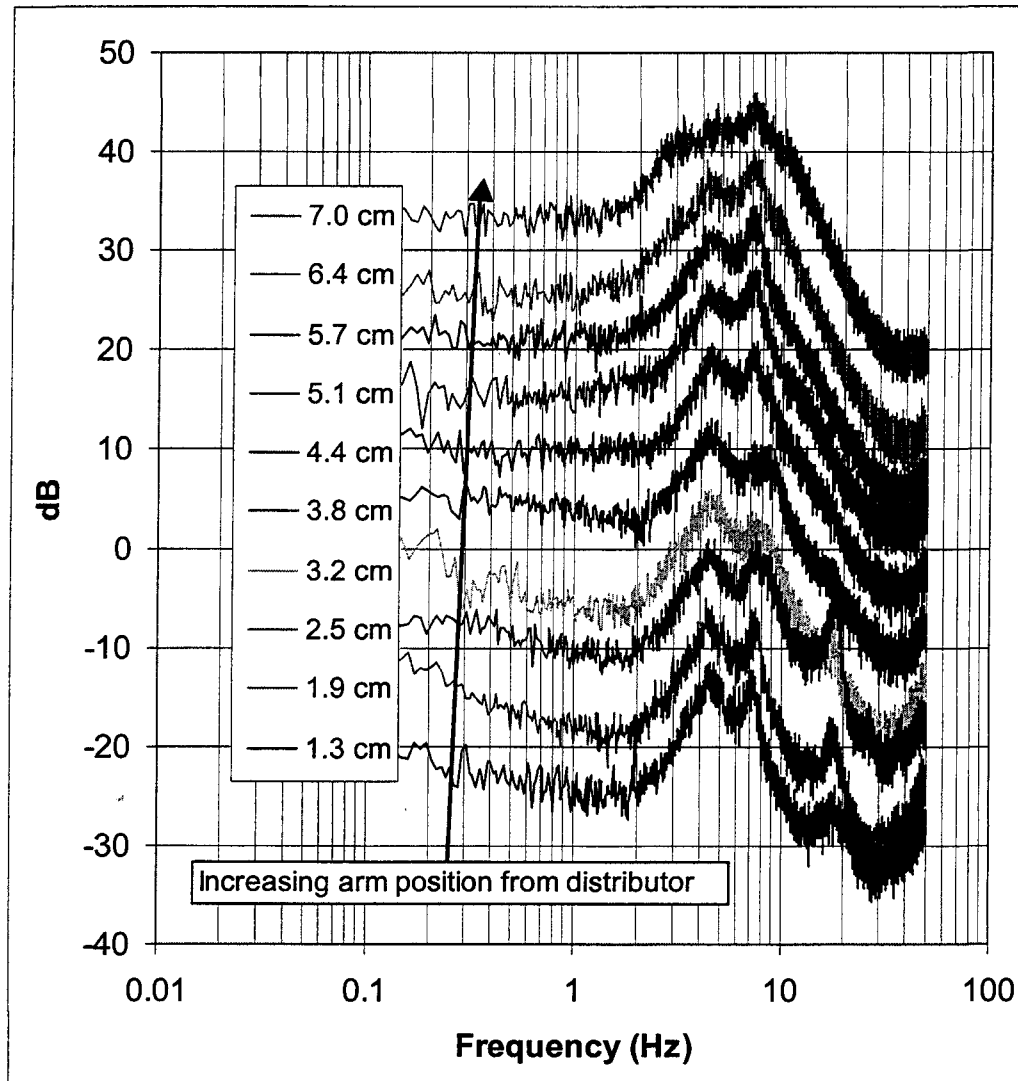


Figure C.1: Power spectra at different probe positions in a 8.6 cm bed

Experimental Operating Conditions for Figure C.2

Bed media	Badger 30x50 Sand	Bed height	12.7 ± 0.3 cm
Mean particle diameter	494 micron	Bed mass	3958.06 ± 0.01 gm
Particle density	2600 ± 100 kg/m ³	Pressure measurement	Dyn-abs
Volumetric flow	345 ± 7.5 LPM	Pressure probe position	Given in figure
Velocity ratio	1.4	File group	102802

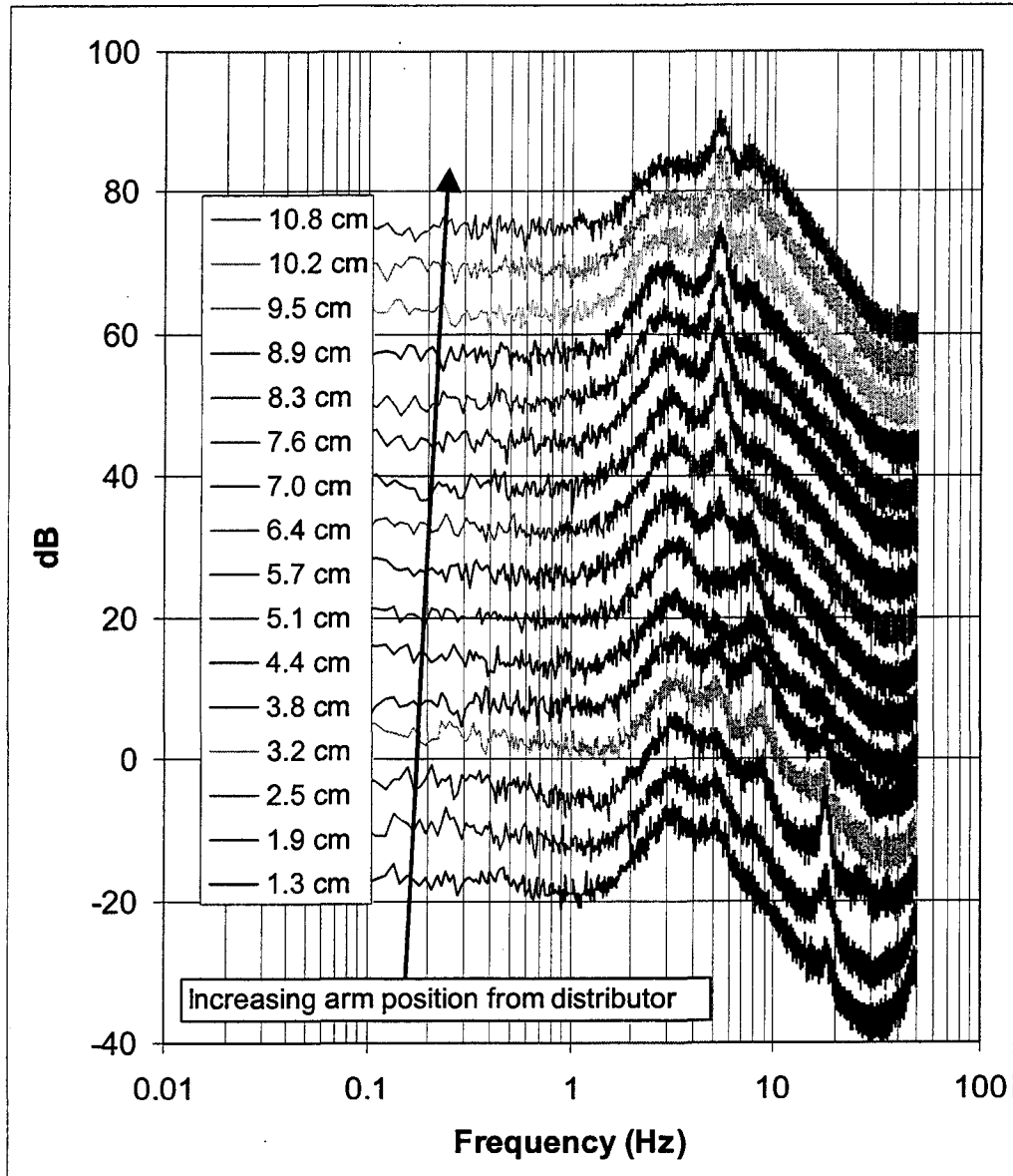


Figure C.2: Power spectrums at different probe positions in a 12.7 cm bed

Experimental Operating Conditions for Figure C.3

Bed media	Badger 30x50 Sand	Bed height	16.7 ± 0.3 cm
Mean particle diameter	494 micron	Bed mass	5277.41 ± 0.01 gm
Particle density	2600 ± 100 kg/m ³	Pressure measurement	Dyn-abs
Volumetric flow	345 ± 7.5 LPM	Pressure probe position	Given in figure
Velocity ratio	1.4	File group	102902

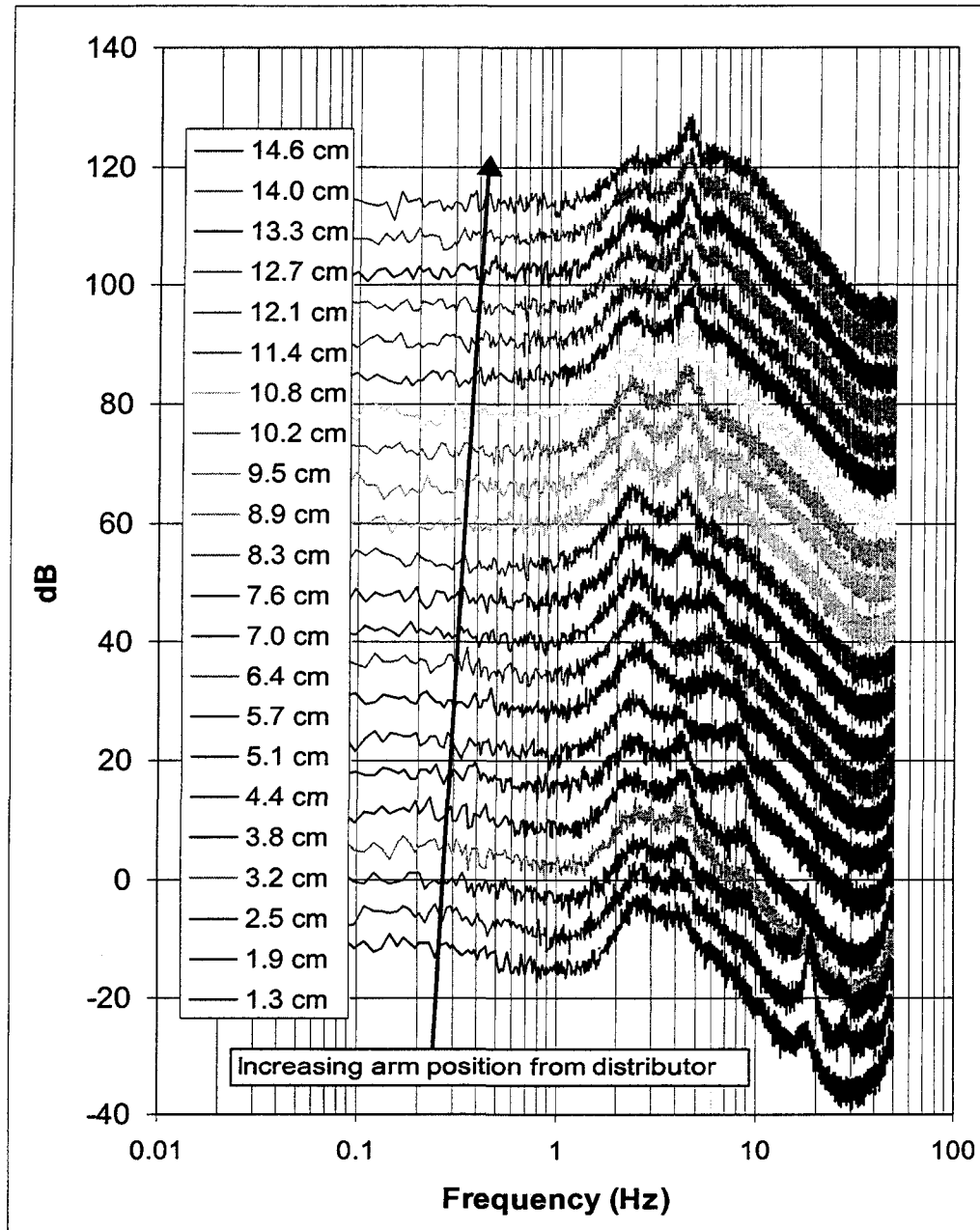


Figure C.3: Power spectra at different probe positions in a 16.7 cm bed

Experimental Operating Conditions for Figure C.4

Bed media	Badger 30x50 Sand	Bed height	21.6 ± 0.3 cm
Mean particle diameter	494 micron	Bed mass	6596.76 ± 0.01 gm
Particle density	2600 ± 100 kg/m ³	Pressure measurement	Dyn-abs
Volumetric flow	345 ± 7.5 LPM	Pressure probe position	Given in figure
Velocity ratio	1.4	File group	100702

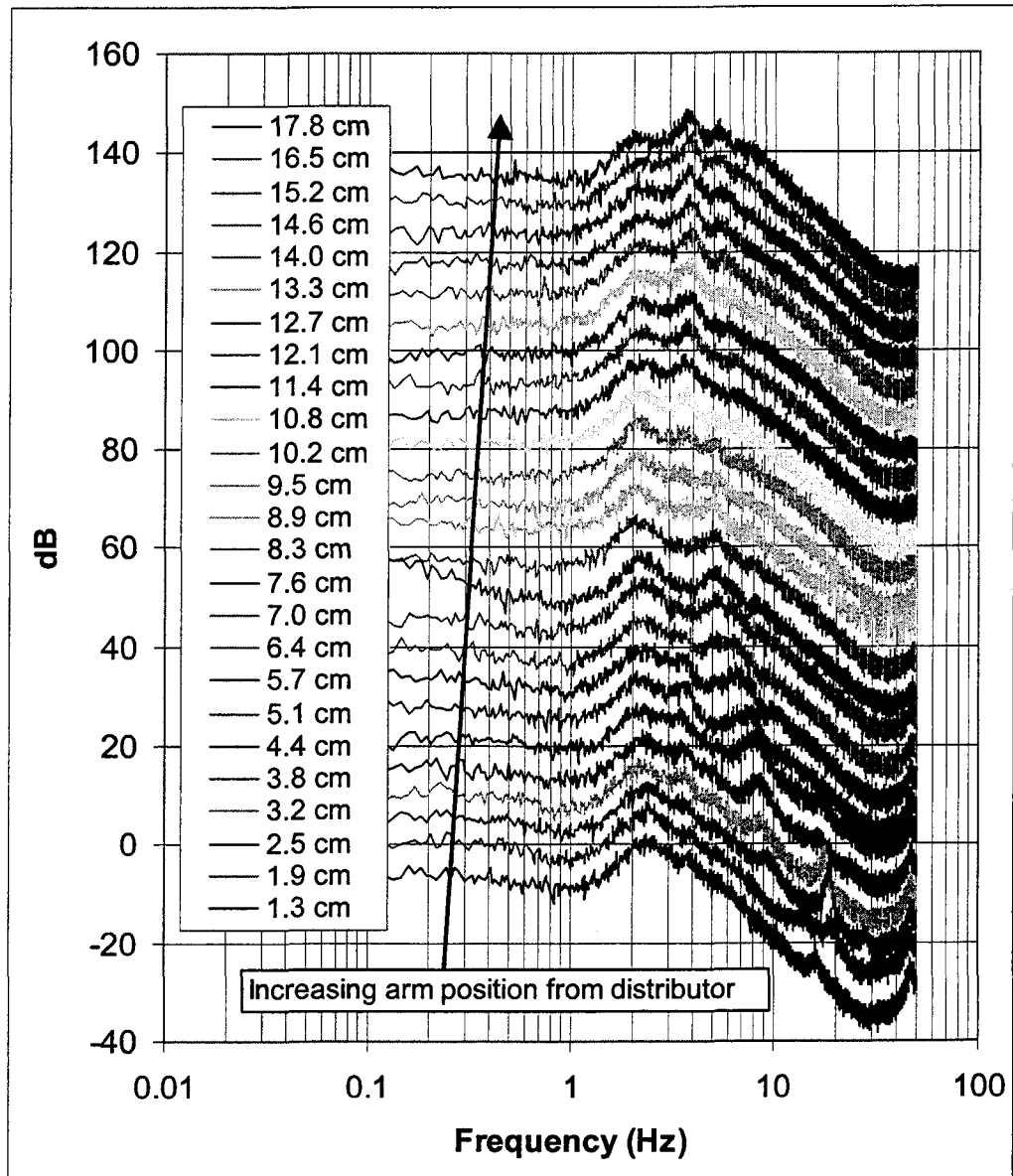


Figure C.4: Power spectra at different probe positions in a 21.6 cm bed

Experimental Operating Conditions for Figure C.5

Bed media	Badger 30x50 Sand	Bed height	24.8 ± 0.3 cm
Mean particle diameter	494 micron	Bed mass	7916.11 ± 0.01 gm
Particle density	2600 ± 100 kg/m ³	Pressure measurement	Dyn-abs
Volumetric flow	345 ± 7.5 LPM	Pressure probe position	Given in figure
Velocity ratio	1.4	File group	092702

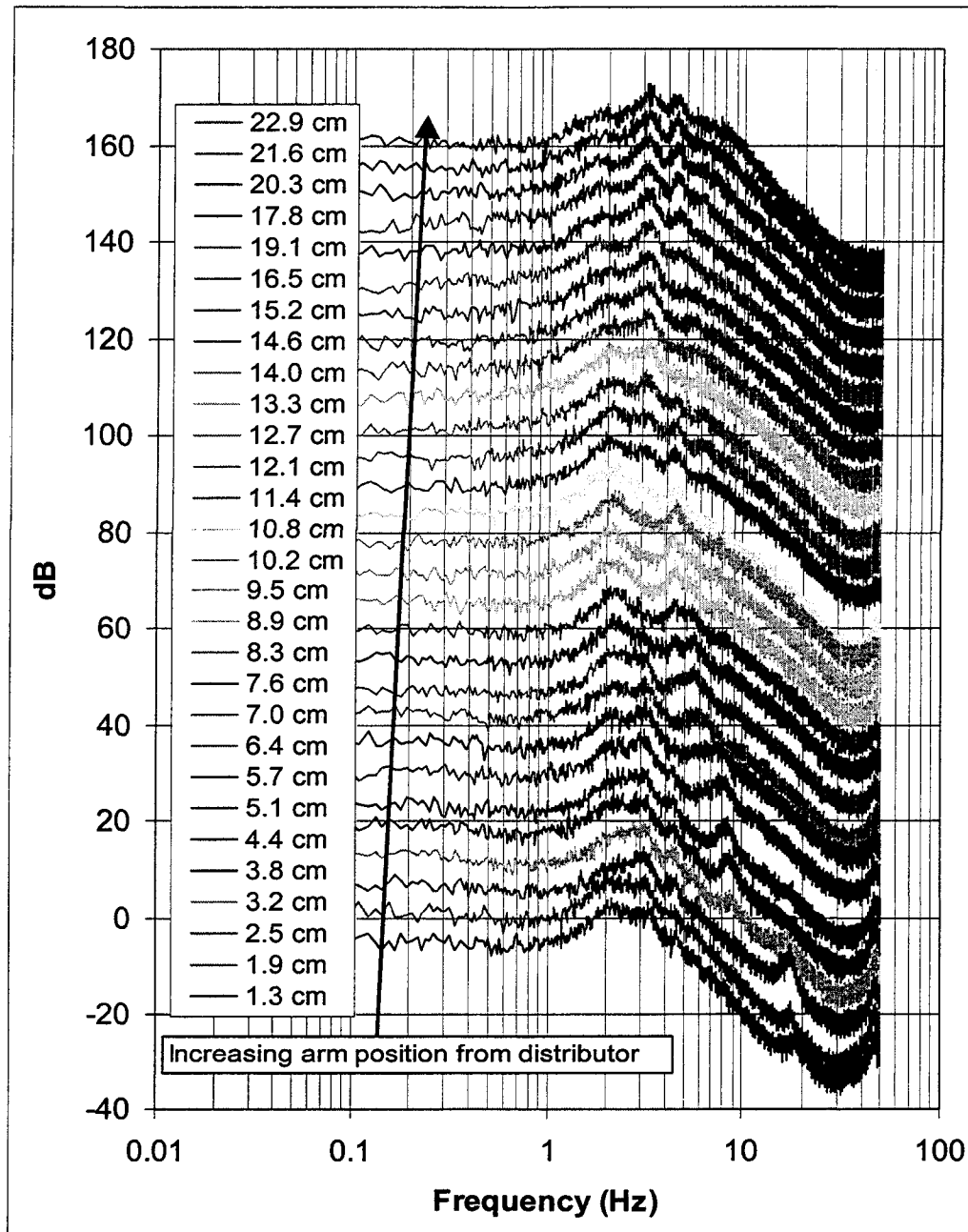


Figure C.5: Power spectrums at different probe positions in a 24.8 cm bed

Experimental Operating Conditions for Figure C.6

Bed media	Badger 30x50 Sand	Bed height	34.0 ± 0.3 cm
Mean particle diameter	494 micron	Bed mass	10554.82 ± 0.01 gm
Particle density	2600 ± 100 kg/m ³	Pressure measurement	Dyn-abs
Volumetric flow	345 ± 7.5 LPM	Pressure probe position	Given in figure
Velocity ratio	1.4	File group	092702

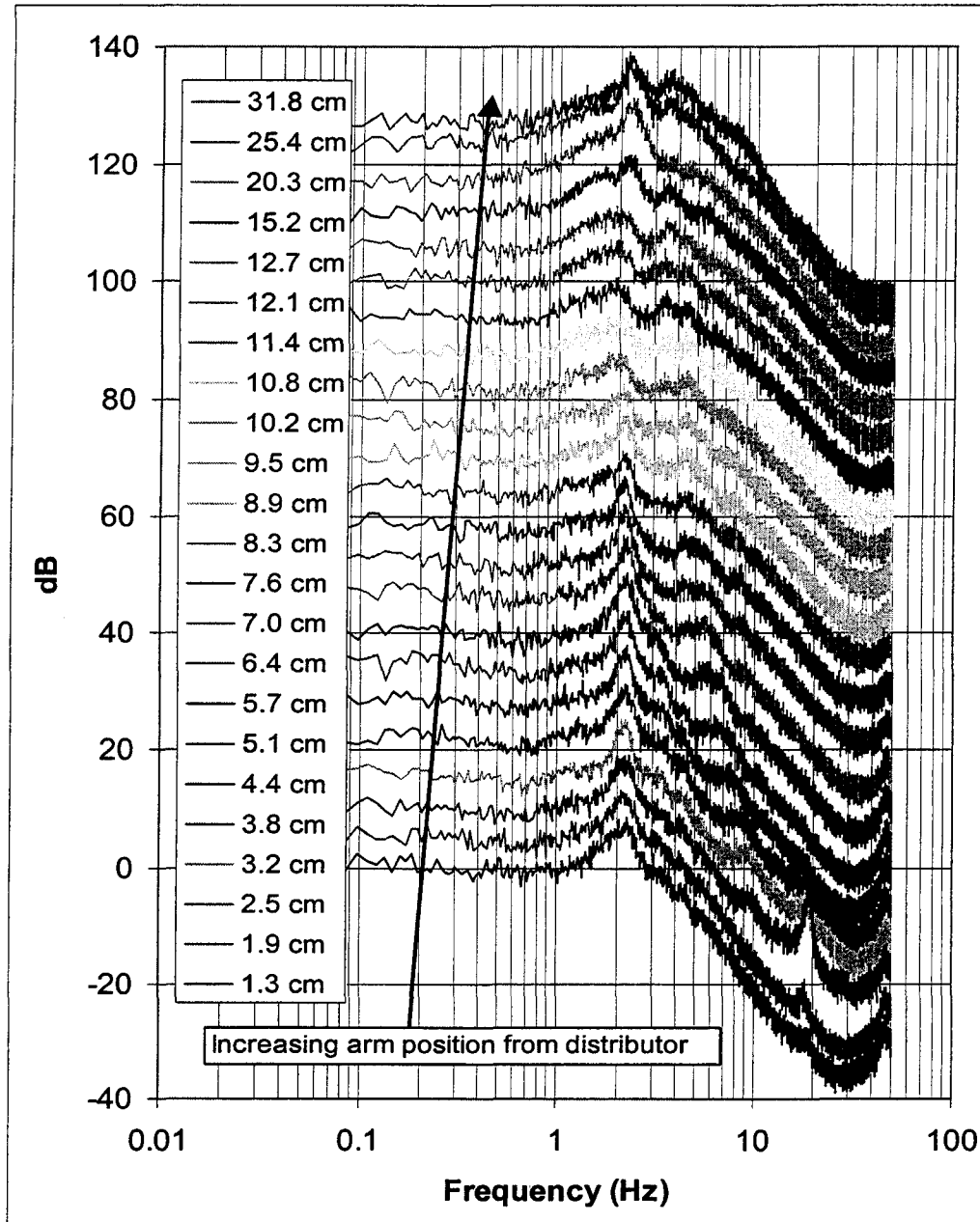


Figure C.6: Power spectra at different probe positions in a 34.0 cm bed

**APPENDIX D. EXPERIMENTAL AND MODELED POWER SPECTRUMS
AT DIFFERENT BED HEIGHTS**

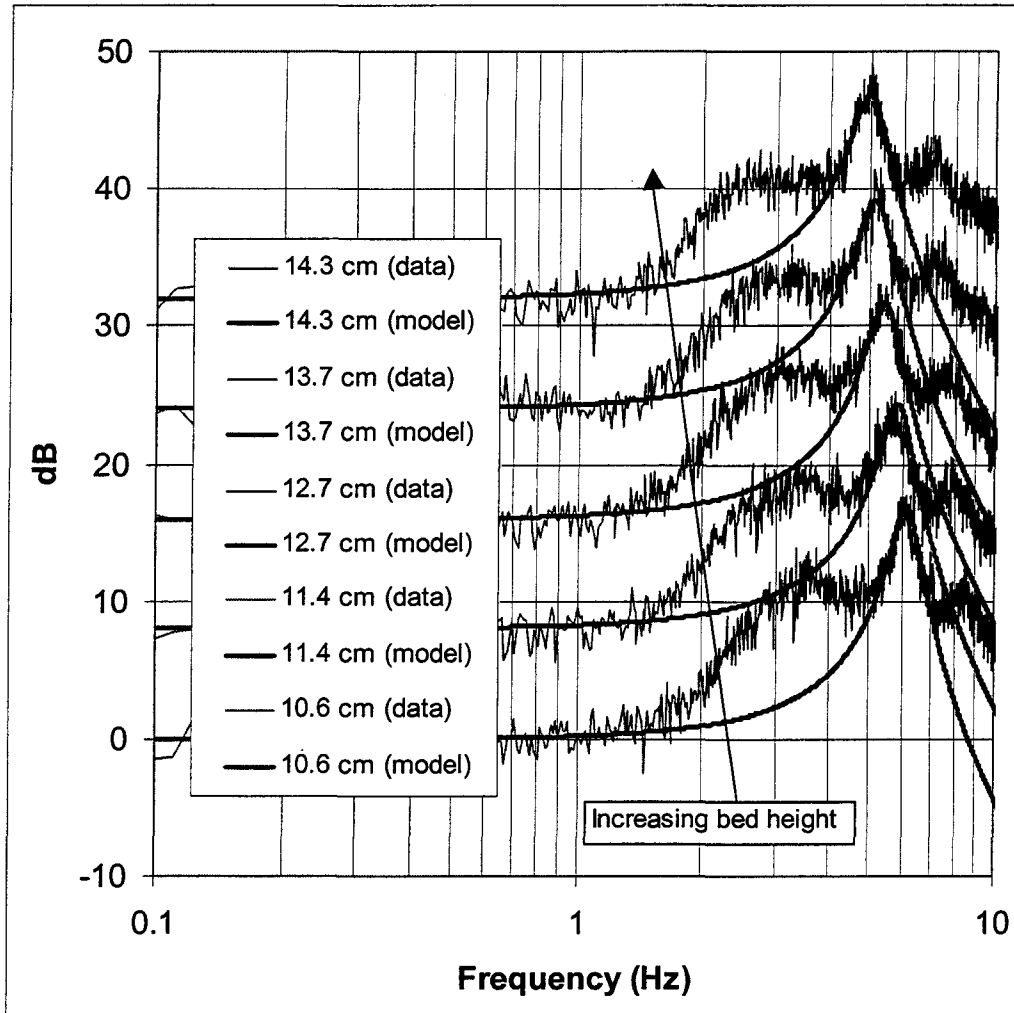


Figure D.1: Experimental and modeled power spectrums at five different bed heights

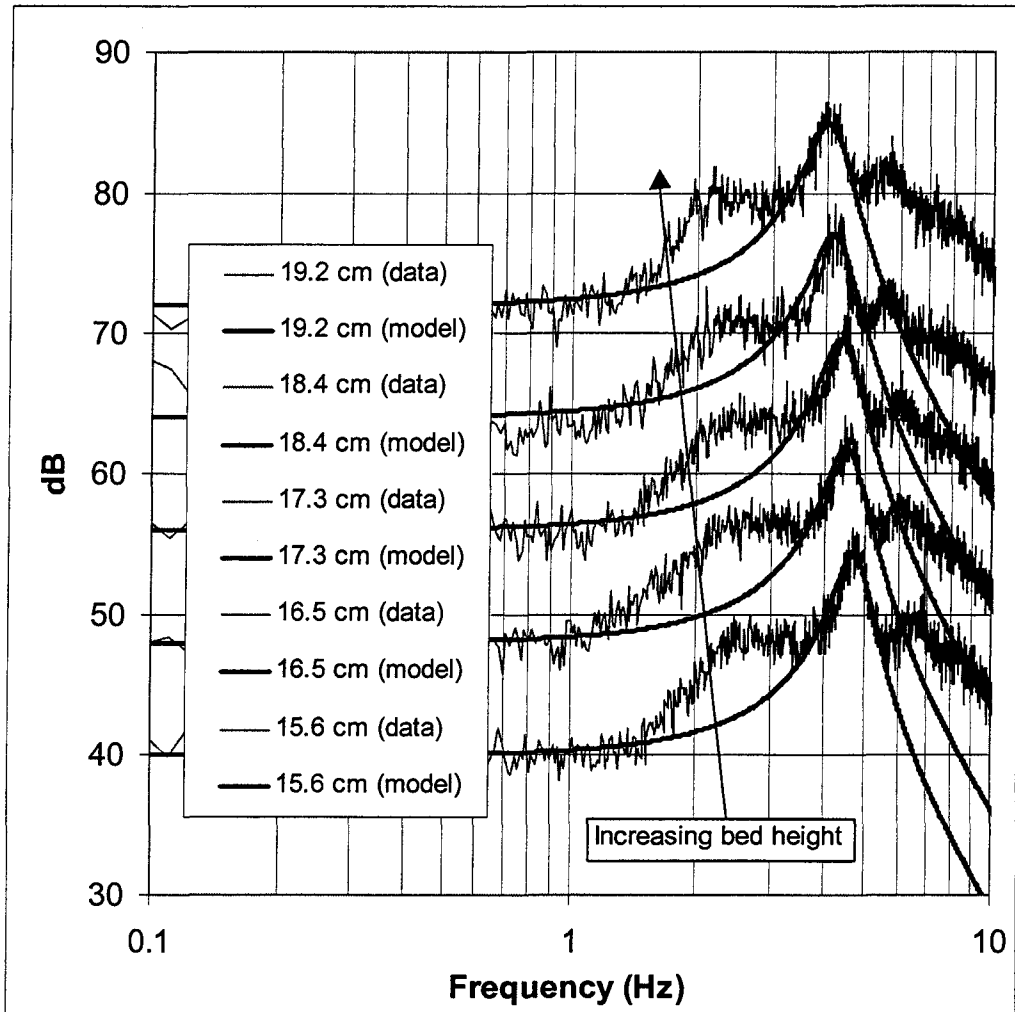


Figure D.2: Experimental and modeled power spectrums at five different bed heights

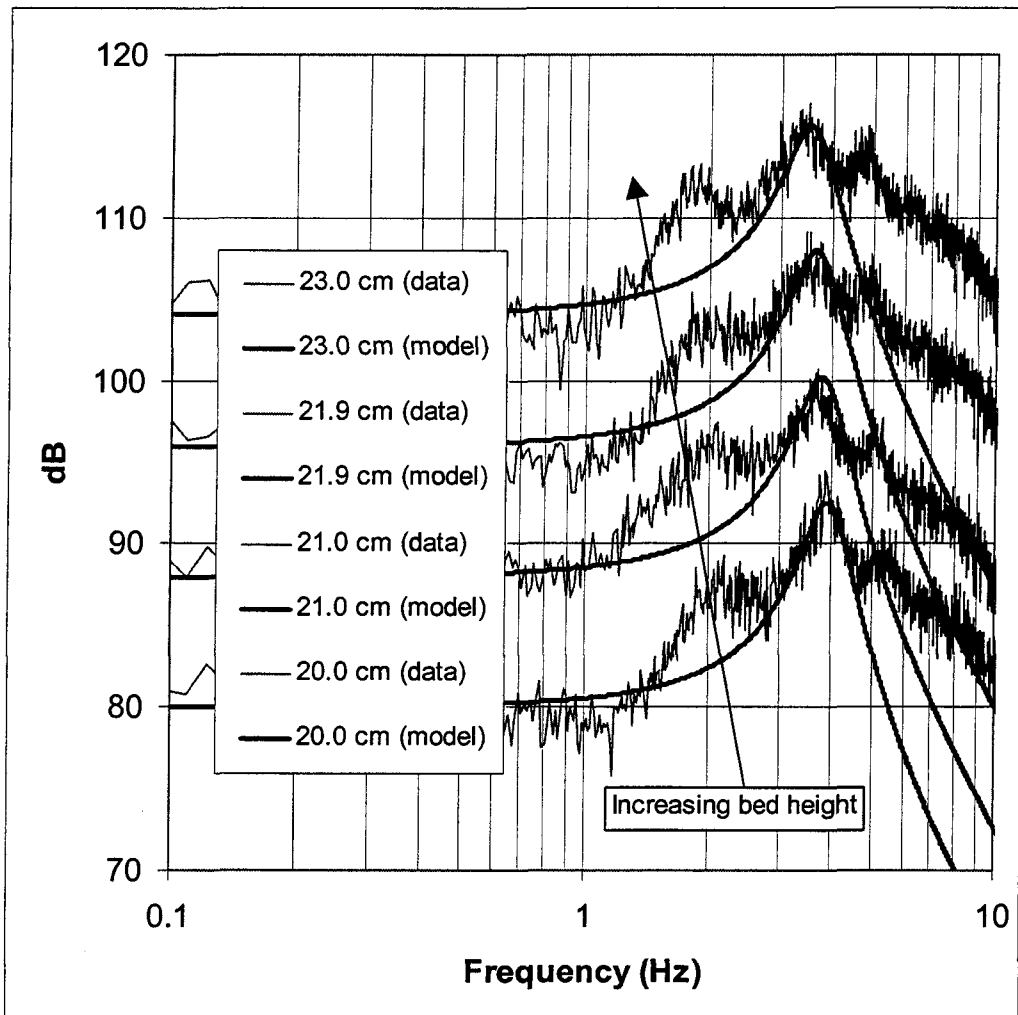


Figure D.3: Experimental and modeled power spectrums at five different bed heights